Oxidation Studies of Nickel, Copper and Cobalt Complexes of Classic Ligands Made Redox-Active

David de Bellefeuille

A Thesis in the Department of Chemistry and Biochemistry

Presented in Partial Fulfillment of the Requirements
for the degree of Master's of Science (Chemistry) at
Concordia University
Montréal, Québec, Canada

March 2014

CONCORDIA UNIVERSITY

School of Graduate Studies

This is to certify that the thesis prepared

By: David de Bellefeuille

Entitled: Oxidation Studies of Nickel, Copper and Cobalt Complexes of Classic Ligands Made Redox-Active

and submitted in partial fulfillment of the requirements for the degree of

Master of Science (Chemistry)

complies with the regulations of the University and meets the accepted standards with respect to originality and quality.

Signed by the final examining committee:

Research Supervisor

Xavier Ottenwaelder _____ _____
Signature Date

Committee Members

Christopher J. Wilds _____ _____
Signature Date

Louis Cuccia _____ _____
Signature Date

Session Chair

Peter Bird _____ _____
Signature Date

Approved by

Graduate Program Director

_____ _____
Signature Date

Faculty Dean

_____ _____
Signature Date

Abstract

Oxidation Studies of Nickel, Copper and Cobalt Complexes of Classic Ligands Made Redox-Active

David de Bellefeuille

In several oxidoreductase metalloenzymes, organic cofactors are transiently converted to radicals in order to achieve efficient catalytic turnover. This is, for example, the case of a tyrosine residue in galactose oxidase. Similarly, small-molecule catalysis can be improved when a transient radical ligand is involved. The present work aims at tailoring the structure of three classic ligands to make them redox-active, i.e. active participants in the electronic structure and reactivity of their complexes upon oxidation. The approach is to render an aromatic moiety on the ligand electron-rich by addition of NMe_2 substituents.

The first chapter describes a neutral Ni(II) complex with **1**. This complex undergoes two reversible oxidations that were characterized by electrochemistry, electron paramagnetic resonance spectroscopy, optical spectroscopy and density functional theory. These oxidations are ligand-based, producing a radical ligand and a diiminoquinone successively.

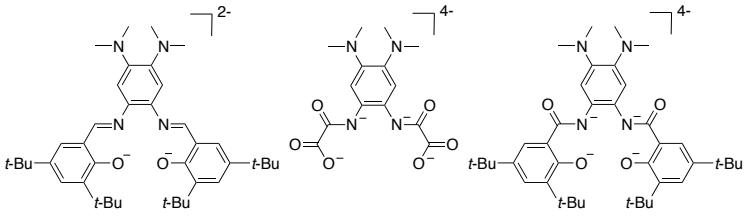

The second chapter investigates Cu(II) complexes of **1** and **2**, for the bio-relevance of Cu in several oxidoreductases. Both ligands oxidize to a radical that is ferromagnetically coupled to the unpaired electron of Cu(II). Spectroscopic characterization and theoretical calculations provide a description of the electronic structure of the oxidized complexes.

The third chapter looks at a Co(III) complex of **3**, which is electron-rich and undergoes redox processes at low potentials. The optical absorption behaviour of the oxidized products is similar to that of the free ligand, suggesting ligand-based oxidation.

As a whole, this thesis describes the effect of strongly electron-donating ligand substituents on the redox and electronic properties of a metal complex. The design leads to an easy strategy by which to tune the electronic structure of a complex by controlling the redox properties of its ligand.

Acknowledgements

First and foremost I would like to thank my research supervisor, Xavier Ottenwaelder, for all the support, help and funding to complete my master's degree. And also for his saintly patience in dealing with an "organic" chemist in his inorganic laboratory. I would also like to specially thank the members of the XoRG: Mohammad Askari, Laura Chaloner, Andrew Proppe and Nooshin Sheibany.

A special thanks to my committee members, Christopher J. Wilds and Louis Cuccia for their insight and expertise during our committee meetings.

Most of this work would not have been possible without the help from our collaborators abroad: Fabrice Thomas and Maylis Orio.

The Department of Chemistry and Biochemistry at Concordia is very cooperative and I must mention a few individuals who helped me throughout my degree. Thanks to Heidi M. Muchall, our GDP, for her support and advice. Thanks to Pat Forgione for our synthetic discussions and the many chemicals and exchanges of glassware and instruments over the years. Thanks to Joanne Turnbull for the Sephadex, without which I would never have purified my complexes. Thanks to Alexey Denisov and Sébastien Robidoux for the NMR training and advice. And thanks to Alain Tessier for mass spectrometry training and assistance with especially difficult compounds.

Some honourable mentions I wish to make are to thank Janet McMillan for her help with the TMBAP project, and Mohammad Askari and Dylan McLaughlin for the X-ray diffraction studies.

It would be impossible to maintain one's sanity if it wasn't for your friends, be it scientific discussions or appropriate distractions; I would like to make a shout out to my friends Derek O'Flaherty, Dylan McLaughlin, Jack Cheong, Harrison Saulnier, Andrew Barber, Francis McManus, Leticia Mori and Michael Cyr.

Lastly I would like to thank NSERC for funding this project.

Dedication

A Master's degree is a major undertaking and requires a monumental amount of work. The purpose to complete this degree is to better yourself in your field of interest and to gain higher education. However, nobody can complete this degree alone. There are people who inspire us to push further, who compel us to perform better and who remind us why we are doing it in the first place. Only my name is written on this thesis but there are many people in my life that I would like to dedicate it to.

Firstly, to my beautiful girlfriend Sarah, I dedicate this thesis. It takes a special kind of bond between two people to put up with the stress and hectic schedules that often come hand in hand with such an endeavour. Know that you were always in my mind while completing this work.

To my wonderful parents, Mom and Dad, I dedicate this thesis. You have always supported my search for higher education, both emotionally and financially. I worked hard everyday for the last 3 years to complete this degree and I would not have been able to persevere if it wasn't for all your support and love.

To my late grandparents, Poppa and Grandma, I dedicate this thesis. You were always great role models to me and you always supported my desire for higher education. You have always been proud of me and I hope that you are smiling down on me now.

To my sister, Suzie, and my extended family, Mrs. Findlay, Paul, Joan, Meaghan and Kevin, I dedicate this thesis. For providing the appropriate distractions I needed and for showing me what is most important in life.

To my children yet to come, I dedicate this thesis. Hard work defines a person's character. Know that you can do whatever you put your mind to and it is with thought of providing you with a great life that I have worked so hard to complete this degree.

Lastly, to Jackson, I dedicate this thesis for helping me find the right sentences to use.

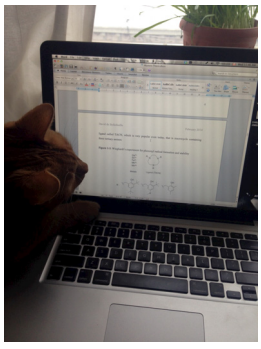

Contributions of Authors

This manuscript presented as part of a Master's thesis was compiled and developed by several collaborators. Authors and their corresponding contributions are listed here.

Reversible Double Oxidation and Protonation of the Non-Innocent Bridge in a Nickel(II) Salophen Complex

David de Bellefeuille*	Syntheses, writing of experimental section, bibliography, editing, proofing
Mohammad S. Askari	X-Ray diffraction, preliminary DFT calculations
Benedikt Lassalle-Kaiser	Preliminary protonation studies
Yves Journaux	Ligand design
Ally Aukauloo	Ligand design
Maylis Orio	DFT calculations, writing of DFT section
Fabrice Thomas	Electrochemistry and EPR, writing, editing and proofing
Xavier Ottenwaelder	Research supervisor, writing, editing and proofing

Redox Non-Innocence of the Bridge in Copper(II) Salophen and bis-Oxamato Complexes

David de Bellefeuille*	Syntheses, UV-Vis experiments, experimental section, bibliography, writing, editing and proofing
Maylis Orio	TD-DFT calculations, writing of DFT section
Ally Aukauloo	Ligand design
Yves Journaux	Ligand design
Christian Philouze	X-ray diffraction
Xavier Ottenwaelder	Research supervisor, X-ray diffraction, writing, editing, proofing
Fabrice Thomas	Electrochemistry, EPR, writing and editing

Implications of Strong Electron-Donating Groups in a Square-Planar Cobalt(III) Complex

David de Bellefeuille*	All experiments, writing, bibliography, editing and proofing
Janet McMillan	Synthesis of precursors
Xavier Ottenwaelder	Research supervisor, X-ray diffraction, editing and proofing

Table of Contents

List of Figures xi
List of Schemes xiv
List of Tables xv
List of Abbreviations xvi
1. Introduction 1
1.1 PURPOSE 1
1.2 BACKGROUND 3
1.2.1 Galactose Oxidase 3
1.2.2 Radicals in other enzymes 5
1.2.3 Redox-active ligands 8
1.2.4 Salen and Salophen models 11
1.3 GOALS OF THIS THESIS 14
1.3.1 Approach 15
1.3.2 Ligand design 16
1.4 METHODS 17
1.4.1 Electrochemistry 17
1.4.2 Electron paramagnetic resonance (EPR) spectroscopy 18
1.4.4 UV-vis-NIR spectroscopy / TD-DFT modeling 19
1.5 ORGANIZATION OF THE THESIS 20
1.5.1 Chapter 2: Reversible Double Oxidation and Protonation of the Non-Innocent Bridge in a Nickel(II) Salophen Complex 20
1.5.2 Chapter 3: Redox Non-Innocence of the Bridge in Copper(II)-Salophen and bis-Oxamato Complexes 21
1.5.3 Chapter 4: Implications of Strong Electron-Donating Groups in a Square-planar Cobalt(III) Complex 21
2. Reversible Double Oxidation and Protonation of the Non-Innocent Bridge in a Nickel(II) Salophen Complex 23
2.0 Notes on the Chapter 23

2.1 INTRODUCTION **24**
2.2 RESULTS AND DISCUSSION **25**
2.2.1 Synthesis and structure of ligand and neutral nickel(II) complex 25
2.2.2 Electrochemistry 27
2.2.3 EPR spectroscopy 30
2.2.4 DFT calculations 31
2.2.5 Electronic spectra and TD-DFT calculations 36
2.2.6 Protonation studies 40
2.3 CONCLUSION **44**
2.4 EXPERIMENTAL **44**
2.4.1 Materials 44
2.4.2 Characterization 45
2.4.3 X-ray crystallography 46
2.4.4 Computational details 46
2.4.5 Syntheses 48
2.5 SUPPORTING INFORMATION **51**
3. Redox Non-Innocence of the Bridge in Copper(II) Salophen and bis-Oxamato Complexes **53**
3.0 Notes on the Chapter **53**
3.1 INTRODUCTION **53**
3.2 RESULTS AND DISCUSSION **56**
3.2.1 Synthesis 56
3.2.2 Oxidation of $H_2\mathbf{L^1}$ and $Et_2H_2\mathbf{L^2}$ 58
3.2.3 Spectroscopic properties of **1**, $\mathbf{1H^+}$ and $\mathbf{2^{2-}}$ 65
3.2.4 Electrochemistry of **1** and $\mathbf{2^{2-}}$ 67
3.2.5 Electronic spectra of the oxidized species 69
3.2.6 EPR spectra of the oxidized species 71
3.2.7 Computational investigation of the complexes 75
3.3 CONCLUSION **84**
3.4 EXPERIMENTAL **84**
3.4.1 Materials 84
3.4.2 Characterization 85
3.4.3 X-ray Crystallography 86

3.4.4 Computational Details 86
3.4.5 Syntheses 88
3.5 SUPPORTING INFORMATION 89
4. Implications of Strong Electron-Donating Groups in a Square-Planar Cobalt(III) Complex 91
4.0 Notes on the Chapter 91
4.1 INTRODUCTION 93
4.2 RESULTS AND DISCUSSION 94
4.2.1 Synthesis and structure of ligand and complexes 94
4.2.2 Electrochemistry 97
4.2.3 Oxidation of ligand and complex 98
4.3 CONCLUSION 101
4.4 EXPERIMENTAL 101
4.4.1 Materials 101
4.4.2 Characterization 102
4.4.3 X-ray crystallography 102
4.4.4 Syntheses 103
5. Conclusion 107
6. References 111
Appendix A 121
Electrochemistry 121
Electron Paramagnetic Resonance Spectroscopy 124
UV-vis NIR Spectroscopy / TD-DFT modelling 128
Appendix B 131
Electrochemistry 131
EPR 133
UV-vis-NIR 134
DFT calculations 135
Appendix C 139

List of Figures

1-1 SOMO of substituted Ni(salen) derivatives.

2-1 ORTEP representation at 50% ellipsoid probability of **1** (^{i}: $x, y, 0.5-z$).

2-2 CV traces of 1 mM CH_2Cl_2 solutions (+0.1 M nBu$_4$NClO$_4$) of **1** and electrogenerated $\mathbf{1}^{+}$ at a carbon working electrode.

2-3 X-band EPR spectrum of the electrochemically generated $\mathbf{1}^{+}$ in CH_2Cl_2.

2-4 Localized molecular orbitals: SOMO of $\mathbf{1}^{+}$, LUMO of singlet $^{1}\mathbf{1}^{2+}$ and SOMOs for triplet diradical $^{3}\mathbf{1}^{2+}$.

2-5 UV-vis-NIR spectra of: **1**, $\mathbf{1}^{+}$, and $\mathbf{1}^{2+}$ generated by spectroelectrolysis at -30°C (1 mM in CH_2Cl_2, 0.1 M nBu$_4$NPF$_6$).

2-6 TD-DFT assignment of the main electronic excitations of $\mathbf{1}^{+}$.

2-7 TD-DFT assignment of the main electronic excitations of singlet $\mathbf{1}^{2+}$.

2-8 TD-DFT assignment of the main electronic excitations of triplet $\mathbf{1}^{2+}$.

2-9 UV-vis titration of a CH_2Cl_2 solution of **1** by HBF_4.

2-10 ORTEP representation at 50% ellipsoid probability of the cationic part of [**1H**](SbF$_6$).

2-11 CV traces of 1 mM CH_2Cl_2 solutions (+0.1 M nBu$_4$NClO$_4$) of $\mathbf{1H}^{+}$ before and after electrolysis at 0.6 V at a platinum working electrode.

3-1 ORTEP representation at 50% ellipsoid probability of the proligands and complexes, with selected bond lengths (Å).

3-2 Cyclovoltammogram of 1 mM CH_2Cl_2 solutions (+ 0.1 M nBu$_4$NClO$_4$) of proligands $H_2\mathbf{L}^{1}$ and $Et_2H_2\mathbf{L}^{2}$.

3-3 UV-vis spectra of proligands and their oxidation products.

3-4 Isotropic solution X-Band EPR spectrum of $(H_2\mathbf{L}^{1})^{+}$ and $(Et_2H_2\mathbf{L}^{2})^{+}$ generated by electrolysis at -30°C (1 mM in CH_2Cl_2, 0.1 M nBu$_4$NPF$_6$).

3-5 Spin density plots, including the values of the most important individual spin populations, and localized SOMOs for $(H_2\mathbf{L}^{1})^{+}$ and $(Et_2H_2\mathbf{L}^{2})^{+}$.

3-6 X-band EPR spectra of **1**, $\mathbf{1H}^{+}$, $\mathbf{1}^{2+}$ in1 mM CH_2Cl_2 frozen solution (+0.1 M nBu$_4$NPF$_6$).

3-7 Cyclovoltammograms of 1.0 mM CH_2Cl_2 solutions (+0.1 M nBu$_4$NClO$_4$) of **1**, **1H**$^+$ and **2**$^{2-}$.

3-8 UV-vis spectra of **1**$^+$ and **1**$^{2+}$ generated by electrolysis at 233 K (CH_2Cl_2, 0.1 M nBu$_4$NPF$_6$).

3-9 UV-vis spectra of **2**$^{2-}$ and **2**$^-$ generated by electrolysis at 233 K (CH_2Cl_2, 0.1 M nBu$_4$NClO$_4$).

3-10 X-band EPR spectrum of **1**$^+$ generated by electrolysis at -30°C (1 mM in CH_2Cl_2, 0.1 M nBu$_4$NPF$_6$).

3-11 X-band EPR spectra of: **2**$^{2-}$ and **2**$^-$ generated by electrolysis at -30°C (1 mM in CH_2Cl_2, 0.1 M nBu$_4$NClO$_4$).

3-12 Spin density plots, including the values of the most important individual spin populations, for **1**, triplet **1**$^+$, doublet **1**$^{2+}$, **2**$^{2-}$ and triplet **2**$^-$.

3-13 Localized SOMOs for **1**, triplet **1**$^+$, doublet **1**$^{2+}$, **2**$^{2-}$ and triplet **2**$^-$.

3-14 TD-DFT assignment of the UV-vis bands for **1**, triplet **1**$^+$ and doublet **1**$^{2+}$.

3-15 TD-DFT assignment of the UV-vis bands for **2**$^{2-}$, triplet **2**$^-$.

4-1 ORTEP representation at 50% ellipsoid probability of the cationic part of (nBu$_4$)**1**.

4-2 CV trace of (nBu$_4$)**1** in CH_2Cl_2 (+0.1 M nBu$_4$PF$_6$) at a glassy carbon working electrode.

4-3 UV-vis titration of **6** with 0.6 mM acetylferrocenium triflate in CH_2Cl_2.

4-4 UV-vis titration of (nBu$_4$)**1** with 0.6 mM acetylferrocenium triflate in CH_2Cl_2.

4-5 UV-vis spectra of **1**$^-$, **1** and **1**$^+$ extracted upon titration of (nBu$_4$)**1** with 0-2 equivalents of acetylferrocenium triflate in CH_2Cl_2.

A-1 Schematic view of an electrochemical cell.

A-2 Typical shape of a reversible redox process in a CV curve.

A-3 The Zeeman effect.

A-4 EPR spectrum.

A-5 EPR absorption and first derivative of a sample exhibiting axial anisotropy.

B-1 Cyclovoltamograms of a 1 mM CH_2Cl_2 solution (containing 0.1 M nBu$_4$NClO$_4$) of **5** at a carbon working electrode.

B-2 Cyclovoltamograms of 0.5 mM CH_2Cl_2 solutions (containing 0.1 M nBu$_4$NClO$_4$) of **1** and *in situ* generated **1H$^+$**.

B-3 Rotating Disc Electrode Voltammetry of 0.5 mM CH_2Cl_2 solutions (containing 0.1 M nBu$_4$NClO$_4$) of **1** and *in situ* generated [**1H**]$^+$; [**1H**]$^+$ after exhaustive electrolysis at +0.6 V.

B-4 X-band EPR spectrum of a 1 mM CH_2Cl_2 (+ 0.1 M nBu$_4$NClO$_4$) solution of the electrochemically generated **1$^+$**.

B-5 X-band EPR spectrum of a 0.25 mM CH_2Cl_2:CH_3OH (3:1) (+ 0.025 M nBu$_4$NClO$_4$) solution of the electrochemically generated **1$^+$**.

B-6 X-band EPR spectrum after electrolysis (one-electron removed) of [**1H**]$^+$ in CH_2Cl_2.

B-7 UV-vis spectra of **1** and the electrogenerated **1$^+$** and **1^{2+}** in CH_2Cl_2 containing 0.01 M nBu$_4$NClO$_4$.

B-8 UV-vis spectra of [**1H**]$^+$ before and after electrolysis at 0.80 V in CH_2Cl_2 containing 0.1 M nBu$_4$NClO$_4$ at -30°.

B-9 Computed metrical parameters in **1** and **1$^+$**.

B-10 Computed metrical parameters in ^{1}**1^{2+}** and ^{3}**1^{2+}**.

B-11 Computed metrical parameters in [**1H**]$^+$ and putative radical species [**1H**]$^{2+}$.

B-12 Spin density plots of **1$^+$** and triplet **1^{2+}**.

B-13 Localized SOMO and spin density plot for the putative radical species [**1H**]$^{2+}$.

B-14 g-tensor orientation for **1$^+$** and the putative radical species [**1H**]$^{2+}$.

C-1 DFT-optimized structure of H_2**L^1** and selected bond lengths.

C-2 DFT-optimized structure of (H_2**L^1**)$^+$ and selected bond lengths.

C-3 DFT-optimized structure of Et_2H_2**L^2** and selected bond lengths.

C-4 DFT-optimized structure of (Et_2H_2**L^2**)$^+$ and selected bond lengths.

C-5 DFT-optimized structure of **1** and selected bond lengths.

C-6 DFT-optimized structure of triplet **1$^+$** and selected bond lengths.

C-7 DFT-optimized structure of doublet **1^{2+}** and selected bond lengths.

C-8 DFT-optimized structure of **2^{2-}** and selected bond lengths.

C-9 DFT-optimized structure of triplet **2$^-$** and selected bond lengths.

List of Schemes

1-1 GO reaction equation.

1-2 Tyrosyl radical in the active site of GO.

1-3 Wieghardt's experiment for phenoxyl radical formation and stability.

1-4 Cytochrome P450's Compound I.

1-5 Molecular orbital diagrams for a square-planar complex (illustrated with a d^8 configuration) with varying electron-density ligands.

1-6 Active site of GO and salen/salophen structures.

1-7 Nickel salcn skeleton used by Thomas and Storr.

1-8 Reedijk's alkyl-substituted salophen nickel(II) complex.

1-9 Target ligands in their deprotonated forms.

1-10 Canonical forms of the phenoxyl radical.

2-1 Tuning the redox properties of an aromatic ligand by appropriate substitution.

2-2 Synthetic route towards **1**.

2-3 Protonation/Oxidation processes from **1**.

3-1 Electronic structure of one-electron oxidized Cu(II) salen complexes.

3-2 Proligands ($H_2\mathbf{L^1}$, $Et_2H_2\mathbf{L^2}$) and Cu(II) complexes investigated in this work.

3-3 Selected calculated bond lengths in $(H_2\mathbf{L^1})^+$ and $(Et_2H_2\mathbf{L^2})^+$, together with the variations upon oxidation from the neutral to the monocationic states.

3-4 Schematic representation of the twist occurring upon double oxidation of 1,2,4,5-tetraamino derivatives between the two 1,3-diaminoallyl moieties.

3-5 Selected calculated bond lengths in $^3\mathbf{1}^+$, $^2\mathbf{1}^{2+}$ and $^3\mathbf{2}^-$, together with the variations upon each 1e oxidation.

4-1 Synthetic route towards $\mathbf{1}^-$.

4-2 Two sequential one-electron ligand-based oxidations located on the central aromatic ring resulting in a Würster's Blue-type radical cation, followed by a diiminoquinone.

5-1 Summary of the ligands and corresponding complexes.

List of Tables

2-1 Crystallographic data for **1** and [**1H**](SbF_6).

2-2 Selected experimental and calculated bond lengths (Å) for **1**, $\mathbf{1}^{+}$ and $\mathbf{1}^{2+}$.

2-3 Individual contributions of the atoms to the spin density in $\mathbf{1}^{+}$ and triplet $^{3}\mathbf{1}^{2+}$.

2-4 Electronic transitions of $\mathbf{1}^{+}$ and $\mathbf{1}^{2+}$ (singlet: $^{1}\mathbf{1}^{2+}$, triplet: $^{3}\mathbf{1}^{2+}$).

3-1 Crystallographic Data for $H_2\mathbf{L}^{1}$, $Et_2H_2\mathbf{L}^{2}$, **1** and $(PPh_4)\mathbf{2}$.

3-2 Redox Potentials.

3-3 Experimental and Calculated Spin Hamiltonian Parameters of the Cu(II) Complexes.

3-4 Electronic Transitions of $\mathbf{1}^{0/+/2+}$ and $\mathbf{2}^{2-/-}$.

4-1 Crystallographic data for $(NBu_4)\mathbf{1}$.

A-1 The impact of SOC on the "g" factor.

B-1 Selected experimental and calculated bond lengths (Å) for $\mathbf{1H}^{+}$ and $\mathbf{1H}^{2+}$.

C-1 Selected calculated bond lengths for $\mathbf{H_2L}^{1}$, $(\mathbf{H_2L}^{1})^{+}$, **1**, triplet $\mathbf{1}^{+}$, doublet and $\mathbf{1}^{2+}$.

C-2 Selected calculated bond lengths for $Et_2H_2\mathbf{L}^{2}$, $(Et_2H_2\mathbf{L}^{2})^{+}$, $\mathbf{2}^{2-}$ and triplet $\mathbf{2}^{-}$.

C-3 Spin Hamiltonian parameters for the oxidized proligands.

List of Abbreviations

CASSCF	Complete Active Space Self-Consistent Field
calcd	Calculated
CIF	Crystallographic Information File
CT	Charge Transfer
CV	Cyclic Voltammetry
ΔEp	Peak-to-peak Separation
DFT	Density Function Theory
DIPEA	Diisopropylethylamine
DMF	Dimethylformamide
$E_{1/2}$	Nernstian Potential
ECE	Electron-transfer followed by Chemical reaction followed by Electron-transfer
EDG	Electron-donating Group
E_p	Peak Potential
EPR	Electron Paramagnetic Resonance
exp	Experimental
Fc	Ferrocene
Fc^+	Ferrocenium
GHz	Gigahertz
GO	Galactose Oxidase
HFC	Hyperfine Coupling
IL	Intraligand
ILCT	Intraligand Charge Transfer
I_p	Current Potential
IVCT	Intervalence Charge Transfer
J_{12}	J^3 Coupling Constant
kHz	Kilohertz
$L^{\bullet}$	Ligand Radical

LLCT	Ligand-to-ligand Charge Transfer
LUMO	Lowest Unoccupied Molecular Orbital
$M^{(n+1)}$	Oxidized Metal Cation
MeOH	Methanol
MHz	Megahertz
ML	Metal-to-Ligand
MLCT	Metal-to-Ligand Charge Transfer
M^{n+}	Metal Cation
MO	Molecular Orbital
MS	Mass Spectrometry
mT	Millitesla
mW	Milliwatt
*n*Bu	*n*-Butyl
NEt_3	Triethylamine
NME_2	Dimethylamino
NMR	Nuclear Magnetic Resonance
OMe	Methoxy
ORCA	*Ab Initio* Quantum Chemistry Program Package
ORTEP	Oak Ridge Thermal Ellipsoid Plot program for crystal structure illustration
Pd/C	Palladium Adsorbed on Carbon
PPh_4	Tetraphenylphosphonium
psi	Pounds per Square Inch
Q-Band	35 GHz EPR Frequency
Salen	N,N'-ethylenebis(salicylimine)
Salophen	N,N'-phenylenebis(salicylimine)
SOC	Spin-Orbit Coupling
SOMO	Singly Occupied Molecular Orbital
t-BuOH	*tert*-Butanol
TACN	1,4,7-Triazacyclonanonane
TD-DFT	Time-Dependent Density Function Theory
UV-vis-NIR	Ultra-Violet, Visble, Near-Infrared

X-Band	8-10 GHz EPR Frequency
ZFS	Zero-Field Splitting

1. Introduction

1.1 PURPOSE

This thesis is a contribution towards the field of bio-inspired catalysis; more specifically, a biomimetic study of oxidative enzymes with the long-term goal of fostering the key mechanistic elements of these enzymes for catalytic purposes. Our group's interest is in studying redox processes of complexes with first-row transition metals. When we think about metal catalysis, one common example is of C–C coupling reactions (Suzuki, Heck, Sonogashira, etc.),[1–3] most of which utilize palladium as the metal catalyst. Such coupling reactions form a single bond between two substrates. Any bond forming or breaking is a 2-electron process, and palladium is outstanding in catalyzing these events because it has the capacity to shuttle between the 0 and +2 oxidation states without the intermediacy of a one-electron process. This ability to gain and lose 2-electrons at a time is a trait of noble metals such as palladium, platinum, silver or gold. For the purposes of this thesis, a "noble" metal can be defined as a transition metal that often undergoes two-electron redox events. Less common noble metals are ruthenium, rhodium, rhenium, mercury, iridium and osmium. One issue is of the abundance of these metals in the earth's crust; metals like palladium, platinum, rhodium and iridium are very rare and are therefore expensive. Also, many of them cannot be disposed of in an environmentally conscious manner and may even have adverse effects to the ecosystem and human health. This is one driving force for interest in bio-inspired catalysis. Nature does not often use rare metals and uses these noble metals even less.

Biological systems tend to use earth-abundant metals[4] like iron, copper and zinc, which are first-row transition metals. This raises the question: how can enzymes selectively perform 2-electron redox processes by using metals that easily shuttle between oxidation states that are one electron apart (e.g. Fe^{2+} and Fe^{3+})? In order to understand this, scientists have prepared model compounds of the active sites of enzymes. The approach is to employ environmentally benign first-row transition metals instead of traditional metals that may be extremely rare or toxic[4,5] and impart noble metal characteristics to their coordination complexes.

First-row transition metals like iron, cobalt, nickel and copper tend to undergo only one-electron redox events (e.g. $Fe^{2+} \rightarrow Fe^{3+}$ or $Ni^{2+} \rightarrow Ni^{3+}$) and the task of imparting this two-electron "noble" metal character is not as simple as choosing the right metal. Coordination complexes involve the metal and the ligand. If the energy levels of both metal and ligand are similar, electrons in high energy levels from either source can be removed during an oxidation. By taking advantage of this, it is theoretically possible for a coordination complex to undergo two one-electron redox events in close succession with the ultimate result being a pseudo two-electron oxidation (i.e. noble metal character). In order to guarantee that two redox events occur, the ligand must have a low oxidation potential, close to that of the metal. Thus, the more electron-rich the ligand the more easily the complex can be oxidized.

Enzymes have evolved abilities to perform many different reactions; occasionally they even contain highly reactive intermediates. Many metallo-enzymes like Cytochrome P450 and Galactose Oxidase exhibit radical intermediates, consistent with an organic cofactor being oxidized by one electron. Combining first-row transition metals with

electron-rich ligands is an excellent methodology to model the active sites of these classes of metallo-enzymes.

1.2 BACKGROUND

1.2.1 Galactose Oxidase

As with many scientific discoveries, interest in bio-inspired redox chemistry stems from the desire to understand and model natural systems. In the early 1980s, biochemists were interested in understanding the structure and the state of the active sites of enzymes. One of particular interest to this field was galactose oxidase.

Galactose oxidase (herein referred to as GO) is a protein with a single copper ion in its active site. It was originally isolated and purified from the fungus *Dactylium Dendroides*. This fungus grows and feeds on hardwood trees and in order to do this it must soften the plant material. This organism uses the enzyme to convert galactose into galactohexodialdose producing hydrogen peroxide as a by-product (Scheme 1-1). The organism discards the dialdose product and secretes the peroxide in order to soften the plant material, rendering it digestible. From the oxidation reaction of galactose it is clear that the enzyme is performing two-electron chemistry but copper exists only in two oxidation states under normal physiological conditions, copper(I) and copper(II). This raised the question of how this reaction was performed at a single copper site. For a while biochemists were pleased to have discovered the first ever biologically stable copper(III)-based enzyme.[6] Shortly thereafter, however, James Whittaker at Carnegie Mellon University questioned this finding and made a very important discovery. By using EPR, he was able to identify the presence of a tyrosyl radical bound to a copper(II) center in GO (Scheme 1-2).[7]

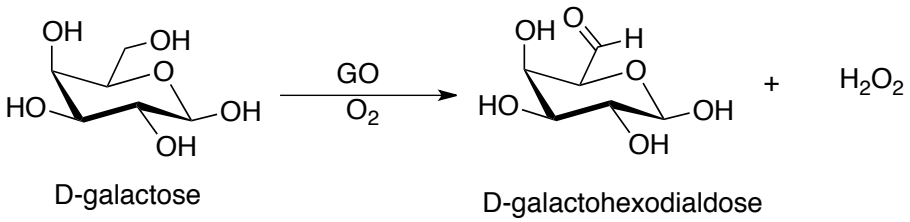

Scheme 1-1. GO reaction equation.

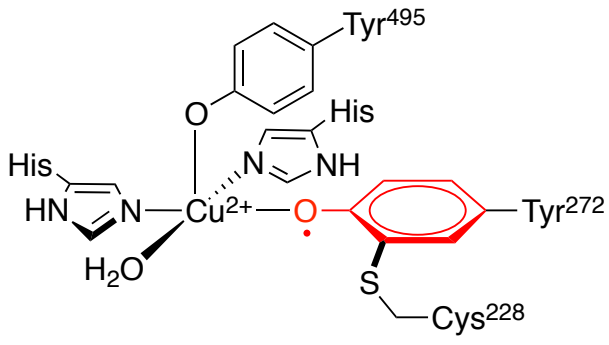

Scheme 1-2. Tyrosyl radical in the active site of GO.

At the time of this discovery, the premise of a stable tyrosyl radical drew the attention of chemists such as Karl Wieghardt from the Max Planck Institute for Bioinorganic Chemistry. His interest lied in the tyrosyl radical's lifetime in physiological conditions. Phenoxyl radicals had been studied before but quickly decomposed or reacted, whereas this tyrosyl radical in GO seemed to be much more stable. He began to make model compounds of phenoxyl radicals coordinated to metal ions using aromatic phenols tethered to a TACN coordinating moiety (TACN = 1,4,7-triazacyclononane) (Scheme 1-3). On the amines he placed differently substituted phenols and complexed the ligands (as trisphenolates) with different metal ions. In every case, the complex undergoes three one-electron oxidations and the oxidized species are persistent. Such numbers of redox processes may not be surprising for metals like iron and manganese that can adopt many different oxidation states, but gallium can only be present in the +3 oxidation state. This

means that the complexes of Ga^{3+} must have been oxidized on the ligand, thus supporting Whittaker's findings that substituted phenols (or tyrosine residues) are redox-active ligands and that ligated radicals have a longer lifetime than typical free radicals. In fact, it was determined that the redox-activity of the tyrosine residue in GO was a result of its substitution with a neighbouring cysteine; the sulphur is a strong electron-donating group that provides more electron density to the aromatic ring, making it easier to oxidize.

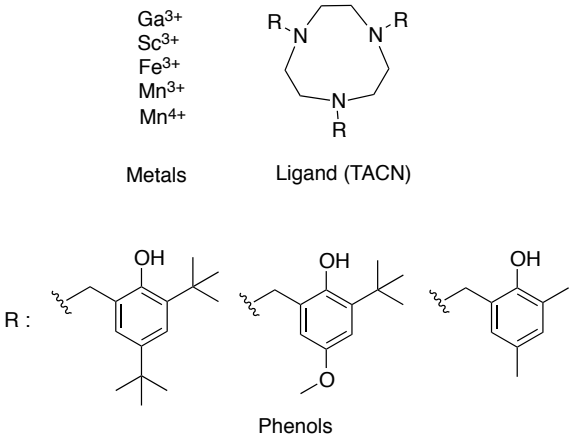

Scheme 1-3. Wieghardt's experiment for phenoxyl radical formation and stability.

1.2.2 Radicals in other enzymes

The behaviour of metal-to-radical coordination is not limited to galactose oxidase, and is present in many other enzymes such as cytochrome P450, ribonucleotide reductase, prostaglandin-H synthase and cytochrome C peroxidase.

The classic example of radicals in enzymes is that of cytochrome P450. This protein contains a high-valent iron(IV)-oxo porphyrin cation-radical complex famously referred to as Compound I (Scheme 1-4). In this species, the radical is stabilized by delocalization over the porphyrin system. Of the many redox reactions that this class of enzymes can perform, one notable reaction is that of C–H bond hydroxylation[8] via the reduction of the

Fe(IV)-oxo-radical to a Fe(III). Compound I abstracts a hydrogen from the C–H bond to form an Fe(IV)-hydroxo intermediate and a C• radical which then combine by oxygen rebound to form the hydroxylated product and an Fe(III) hemic moiety.[8]

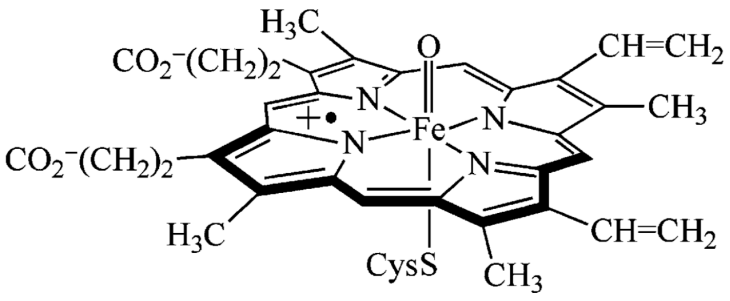

Scheme 1-4. Cytochrome P450's Compound I.[9]

In the case of ribonucleotide reductase, the presence of a stabilized tyrosyl radical coupled to a μ-oxodiferric centre is essential for the proper function of the enzyme. This enzyme catalyzes the formation of deoxyribonucleotides from ribonucleotides and therefore is directly involved in DNA synthesis and the rates of cellular division (mitosis). If this enzyme were too reactive, the DNA to cellular material ratio would be too high; conversely if the enzyme were not reactive enough, cellular division would become slowed. In order for the reaction to proceed, two steps must occur before the substrate binds to the active site: a tyrosine residue must be oxidized, and two subunits of the enzyme must come together. The initial oxidation of tyrosine is of particular relevance to this thesis as the oxidation potential of tyrosine (~0.94 V)[10] is far too high for this residue to be oxidized under normal physiological conditions. Therefore, the tyrosine residue must have been enriched with electron density by some means, in order to lower its redox potential. Initially, a Fe(II) dimer inserts O_2 between the Fe(II) centers by

oxidative addition and rearranges to form Fe(III)–O–O–Fe(III) which is reduced to H_2O–Fe(III)–O–Fe(IV), then reacts with tyrosine to form a tyrosyl radical coupled to a Fe(III)–O–Fe(III).[10]

Another example of nature using a tyrosyl radical is in the enzyme prostaglandin-H synthase, a bifunctional enzyme containing cyclooxygenase and peroxidase active sites (hemic). This enzyme is important in the biosynthesis of prostaglandins, which are messenger molecules that can induce local and systemic effects in the body (ex. pain, swelling, etc). The cyclooxygenase converts arachadonic acid into prostaglandin endoperoxide G_2, which then gets reduced by peroxidase to make prostaglandin endoperoxide H_2,[10] which is an important biological molecule. The mechanism is disputed but recent evidence suggests that a tyrosyl radical is generated by the reduction of a heme [Fe(IV) to Fe(III)] to allow the arachadonic acid to bind in the active site. Furthermore, this radical is formed during the catalytic cycle of peroxidase.[10]

Cytochrome *c* peroxidase catalyzes the oxidation of two molecules of ferrocytochrome *c* to ferricytochrome *c* while reducing hydrogen peroxide to water. Being in a hemic protein, the iron centre shuttles between Fe(II), Fe(III) and Fe(IV), providing two redox equivalents from the metal alone. In most peroxidases, the second oxidizing equivalent is stored in the porphyrin, however, in the case of cytochrome *c* peroxidase, the oxidizing equivalent is stored as an oxidized amino acid residue, a tryptophan radical cation.[10] This tryptophan radical is very stable and persists longer than a free tryptophan radical, which was reasoned to be caused by an electron-rich iron centre due to deprotonation of a nearby histidine residue.[10]

Although the manner in which a radical is formed in metallo-enzymes may differ, these situations have one aspect in common; electron-rich aromatic ligands can be oxidized and remain stable for the duration of the catalytic cycle.

1.2.3 Redox-active ligands

Over the past 30 years, researchers have been identifying an increasing number of situations where oxidation of the organic ligand occurs as well as or in the place of the metal, which was traditionally thought to be the only oxidizable centre. The frontier orbitals of a complex normally exhibit a high metal character, meaning that a d orbital from the metal is little delocalized with the primary coordination sphere of the ligand. This delocalization is small provided the energy gap between "ligand" orbitals and "metal" orbitals is large. For these kinds of complexes, the redox behaviour, rather the orbital considerations therein, is governed by the metal. However, if the orbitals of the ligand are higher in energy (i.e. strong π/σ donors), their participation in the frontier orbitals of the complex is greater (Scheme 1-5).

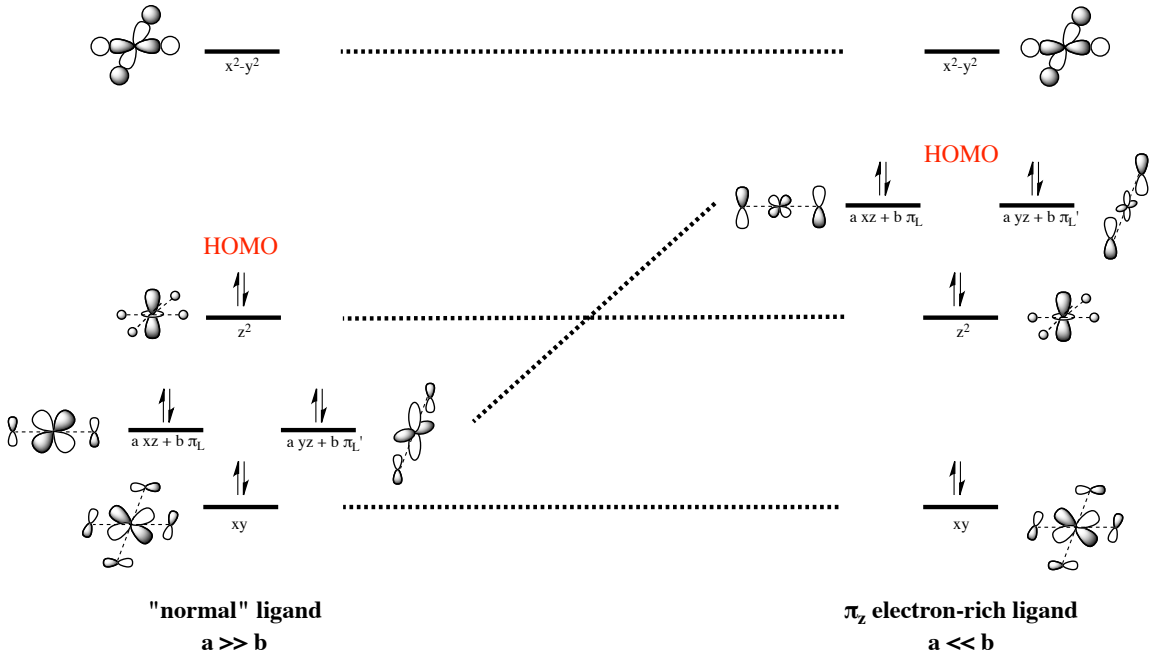

Scheme 1-5. Molecular orbital diagrams for a square-planar complex (illustrated with a d^8 configuration) with varying electron-density ligands. On the left, the typical case with small participation of the ligand fragment. On the right, the case of a ligand with an electron-rich out-of-plane π system (π_z). In this case the HOMO of the complex is essentially distributed on the π orbitals of the ligand with minimal involvement of the metal fragment.

Scheme 1-5 displays the MO diagram of a transition metal complex with a “normal”, "innocent" ligand and of a complex with an electron-rich ligand. The coefficient *a* represents the d orbital contribution and *b* represents the π_z orbital contribution of the ligand in the out-of-plane π-type interactions. In the “normal” ligand case, *b* is small because the ligand fragment orbitals are low in energy. The d(xz) and d(yz) orbitals remain metal-based; $d(z^2)$ is the HOMO. An oxidation from this system would occur logically from the HOMO, i.e. to form a a $d(z^2)^1$ configuration. In the electron-rich ligand case, *b* is large because the ligand fragment π_z orbitals are higher in energy and interact strongly with the d(xz) and d(yz). The antibonding orbital resulting from this interaction has a high energy and incorporates an increasing contribution of the ligand. In the

extreme case, this orbital becomes of ligand character with a small participation of d(xz) and d(yz) ($a << b$). Hence, the HOMO is on the ligand and an oxidation would generate an unpaired electron on a ligand-based orbital, i.e. a radical.

Organic ligands that behave in this manner are referred to as "non-innocent", meaning they are not innocent in the redox process (i.e. they are involved in the redox chemistry) or redox-active. The two terms are synonymous and refer to the same process. In essence, a redox-active ligand is an organic ligand where the locus of oxidation is on the ligand itself. These are generally conjugated ligands with an electron-rich aromatic system. In the presence of an aromatic ligand, one can thus encounter either of the two oxidation situations delineated in (Eqn 1-1).

$$M^n / L - e^- \rightarrow M^{n+1} / L \; or \; M^n / L^{+\bullet} \qquad \text{(Equation 1-1)}$$

Characterization of complexes with redox-active ligands can be difficult because it is not always a simple case of one product or the other. In fact, the products in Eqn. 1-1 are isomers called electromers or valence isomers. These are isomers that vary only in their electronic configuration that is the population of their respective orbitals. Generally, one isomer is favoured above the other, but in some cases the energies of the two forms can be close and interconversion is possible. This balance is referred to as valence tautomerism (Eqn 1-2). When the metal-oxidized and the ligand-oxidized species are in equilibrium, it becomes very difficult to characterize the types of complexes, notably because the equilibrium can shift easily one way or the other when phase changes are involved (e.g. precipitation for X-ray crystallography or freezing a solution for low-temperature spectroscopy).

$$M^{n+1} / L \Leftrightarrow M^{n} / L^{+\bullet}$$ (Equation 1-2)

The equilibrium can be pushed in either direction by manipulating the properties of the metal and the ligand and especially the individual redox potential of the complex. For example, by substituting the ligand with electron-donating groups (EDG), thus rendering it more electron-rich, the ligand-oxidized product is favoured.

1.2.4 Salen and Salophen models

Inspired by the active sites of metallo-enzymes like GO, researchers have made synthetic mimics in order to understand the redox chemistry taking place. The models are designed to be as close as possible to the structure of the active site, especially the nature of the coordinated ligands. The active site of GO, for instance, contains an N_2O_2 coordination sphere and an extended π-network via the tyrosine and histidine residues. This coordination sphere can be modeled by a bis-(Schiff base)-bis(phenolate) ligand like a classic "salen". Salen is a classic ligand that is an abbreviation of salicylaldehyde and ethylenediamine. It is the aliphatic form of the ligand shown in Scheme 1-6.

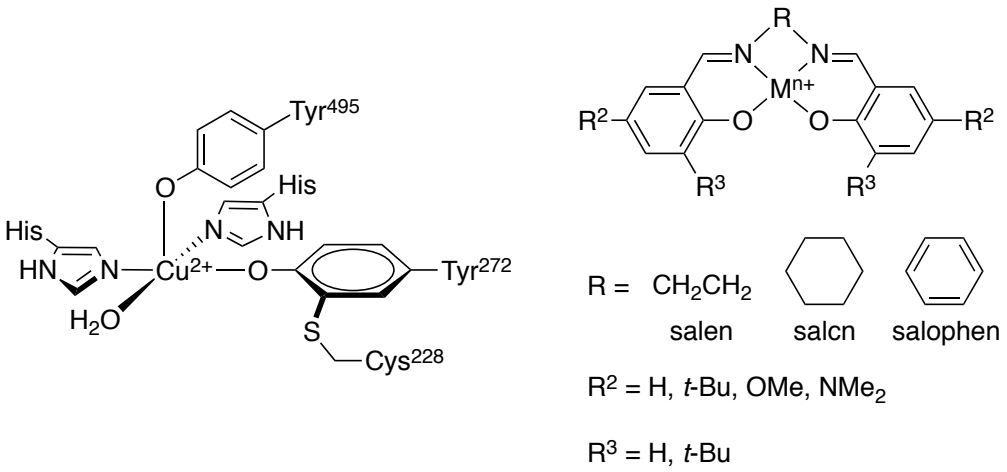

Scheme 1-6. Active site of GO and salen/salophen structures.

These mimics are electron-rich and contain extended π-systems. This high electron density in π-type orbitals (once the phenols are deprotonated) induces an oxidation primarily on the ligand (Scheme 1-5).[11] Fabrice Thomas' group in Grenoble prepared salcn models using copper(II) and nickel(II). They substituted the *para* position of the phenolates with a methoxy group and noticed that upon oxidation, a radical formed that was delocalized along the π-system.[12,13] Using UV-vis-NIR, EPR and TD-DFT they show that the radical is stabilized by sharing some spin density with the metal, consistent with GO's behaviour. Building on this model, Tim Storr's group at Simon Fraser University varied the electron donating strength of the substituent (i.e. *t*-butyl, methoxy, dimethylamino) and studied the impact of the substitution at the *para* position of the phenolate oxidizing the nickel(II) complex.[14] The stronger the electron-donating group the more the radical was localized on one of the phenolates.

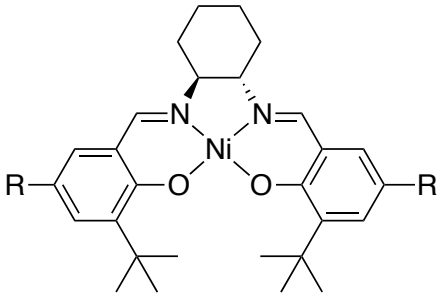

R = *t*-Bu (1)
R = OMe (2)
R = NMe_2 (3)

Scheme 1-7. Nickel salcn skeleton used by Thomas and Storr.

Figure 1-1 shows the singly occupied molecular orbitals (SOMO) corresponding to the oxidized complexes with the different substituting groups. The methoxy and dimethylamino substituted complexes show localization of the radical on one side of the molecule or on one of the phenolates. Clearly the radical does not seem to be delocalized through the metal when the complex contains strong electron-donating substituents. This led Thomas to prepare salophen complexes with the same substitution as their salen counterparts. A salophen ligand is the short hand for salicylaldehyde and phenylenediamine (Scheme 1-6). Thomas prepared copper(II) complexes with a *para*-methoxy substituted salophen ligand and observed, yet again, delocalization of the radical on one of the phenolates.[13]

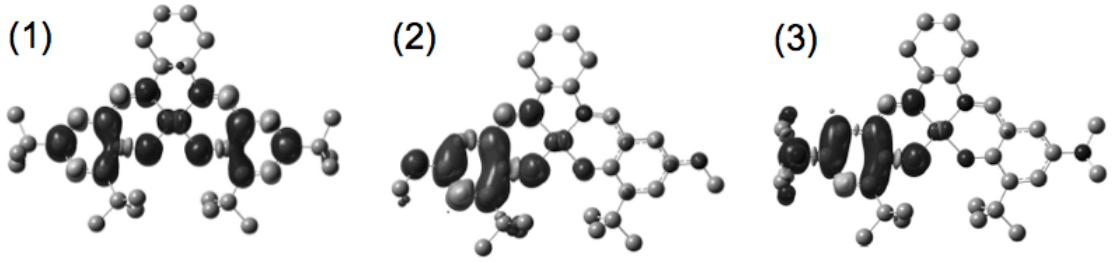

Figure 1-1. SOMO of substituted Ni(salen) derivatives.[14]

By comparison, Jan Reedijk from Leiden University prepared salophen complexes with less electron-rich phenolates and observed complete delocalization.[15] In conclusion, the stronger the electron donation of the substituent on the phenolates, the greater the localization of the radical.

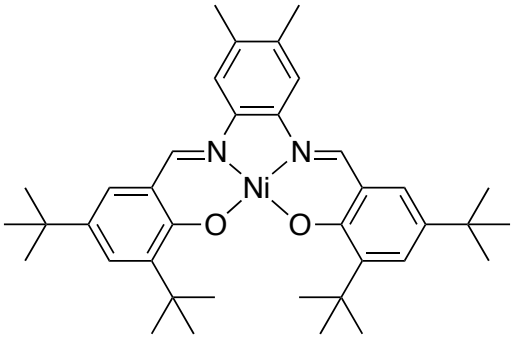

Scheme 1-8. Reedijk's alkyl-substituted salophen nickel(II) complex.[15]

1.3 GOALS OF THIS THESIS

An important observation from the previous work in this field is that by modifying the strength of the EDGs, one can control the localization of the radical formed upon oxidation. Our group became interested in the potential for such complexes in bio-inspired catalysis. A good redox catalyst must have low redox potentials and noble metal character (i.e. 2-electron redox processes). If we compare the salophen complexes used

by Thomas and Reedijk, there is one main difference. Reedijk substituted the main aromatic ring with, albeit mild, EDGs and he observed delocalization of the radical over the entire molecule. Furthermore, Thomas prepared a salophen complex where the central aromatic ring is substituted with OMe groups and he observed partial localization of the radical on the central aromatic bridge.[13] Our hypothesis is that enriching the central ring with more electron-donating groups, the oxidations would both take place on the central ring rather than having one oxidation per phenolate This situation is desirable for reasons of coupling between fragments. With an oxidation occurring on a phenolate, the molecule formally contains a phenoxyl and a phenolate moieties, and is thus in a mixed-valence state. The two moieties are likely coupled[16,17] and this would thus spread the redox potentials of the first and second oxidations, thereby deterring from noble character. We are striving to localize the oxidation on a single moiety to prevent this situation.

My research goals can then be summarized as this: to prepare new kinds of redox-active ligands that can undergo two redox events on a single moiety. By substituting the central aromatic ring with strong EDGs, the molecule become very electron-rich, making it easier to oxidize and thus lowering the redox potentials. If these potentials are low enough, two redox events could occur instead of one.

1.3.1 Approach

My approach was to design three ligands with dimethylamino substitution on the central aromatic rings. One is a modified salophen that when complexed with a 2+ metal makes a neutral complex. The next ligand is used for comparative purposes; it eliminates the possibility of any delocalization on the phenolates as they are replaced with oxamates.

The last contains amide functionalities rather than imines making the complex negatively charged and thus more electron rich while maintain all the aspects for the first. The latter being more electron-rich may lead to lower oxidation potentials.

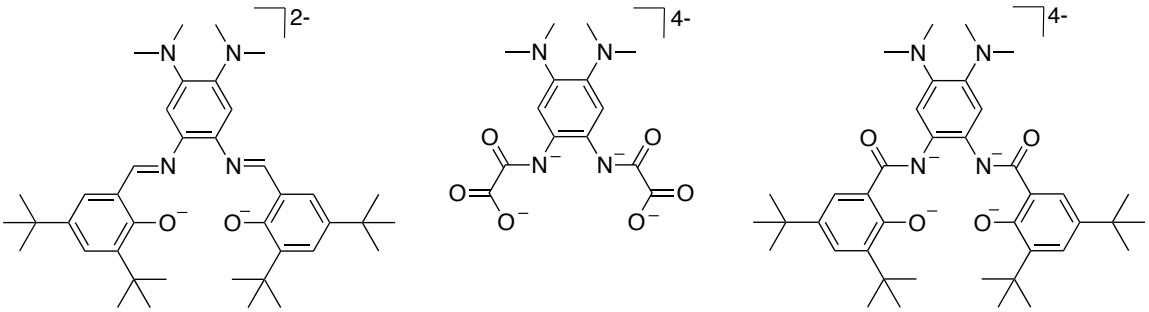

TMTS TMopba TMBAP

Scheme 1-9. Target ligands in their deprotonated forms.

1.3.2 Ligand design

There are several considerations involved in the design of the target ligands above. As mentioned before, the ligand must contain an N_2O_2 coordination sphere. In order to stabilize a radical, the ligand must also contain an extended π-system, hence the salophen backbone of TMTS and TMBAP. The absence of such a large extended π system in TMopba was intentionally done for comparative purposes. The *ortho* and *para* positions of the phenolates are substituted with *t*-butyl groups for two reasons: to increase the solubility in organic solvents and to protect vulnerable positions from radical reactions (Scheme 1-10). Lastly, the substitution of strong EDGs on the central aromatic ring; in this case, two dimethylamino groups are added in order to maximize the electron density of the central aromatic ring. For the third ligand, a single replacement of the imine to an amide is done to increase electron richness. The first ligand from Scheme 1-9 is named "TetraMethyl-*T*-butylSalophen" or TMTS for short, the second is named "TetraMethyl-

O-PhenyleneBisoxAmate" or TMopba and the third is named "TetraMethylBisAmidoPhenol" or TMBAP.

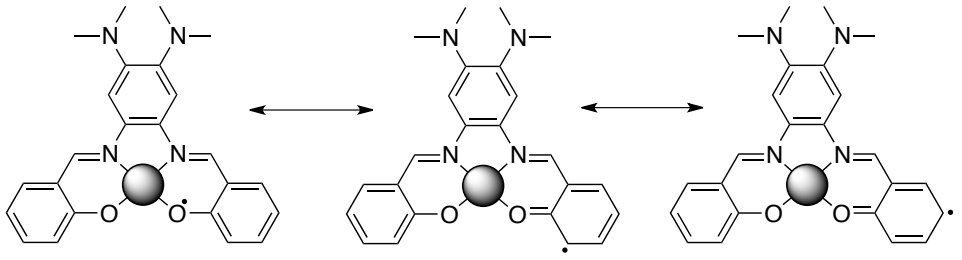

Scheme 1-10. Canonical forms of the phenoxyl radical.

1.4 METHODS

The manuscripts presented in this thesis involve several inorganic techniques that may not be explained in detail. A concise description of the major techniques is given in appendix A, with a short overview below.

1.4.1 Electrochemistry

Of several electrochemical techniques available, two have been used in this work: cyclic voltammetry (CV) and electrolysis. In CV the principle is quite simple; the analyte is redox-active, meaning that by supplying a low potential to the solution (NB: potentials are measured with respect to a reference electrode), electrons are present at the electrode surface and can induce a reduction of the complex, conversely by applying a high voltage (with respect to the redox potential of the complex), electrons will flow from the complex to the electrode (i.e. oxidation). The instrument records changes in current (electron flow) with respect to changes in potential. Therefore the shape of the curve provides information about which process is occurring. During an oxidation, electrons are being

"released" by the analyte, thus increasing the current in the cell. Hence, during a reduction, electrons are being "consumed" by the analyte, thus lowering the current in the cell. This technique is used to observe the presence of redox events and their reversibility and to measure the redox potentials of the events.

Although one can calculate the number of electrons per redox event by using Nernstian relationships, a more conclusive way of obtaining this information is by electrolysis. In addition, this technique can also provide more information about the stability of the oxidized/reduced species. An electrolysis experiment is done after the CV has determined the redox potentials. A voltage is maintained just slightly above that of an oxidation event and the solution is allowed to completely oxidize. Once there is no change in current, the total charge can be calculated and the moles of electrons per moles of analyte can be determined. Another experiment to determine stability is to perform a CV after the electrolysis. If both CV curves (before electrolysis and after electrolysis) match, there has been no decomposition of the analyte in the oxidized state.

1.4.2 Electron paramagnetic resonance (EPR) spectroscopy

Since these complexes have been tailored to exhibit redox-active ligand behaviour, the oxidized product either contains a radical or results from a change in oxidation state of the metal, both of which are characterized by EPR spectroscopy. In an EPR experiment, the electron spin is reversed when it absorbs microwave energy; the instrument records this absorption and displays the first derivative. The position and shape of this signal is informative on the position and delocalization of the unpaired electron on the molecule (electronic structure).

Similar to the chemical shift in an NMR experiment, the value of the g-factor depends on the immediate environment of the unpaired electron. A free electron has a g_e of 2.0023 and any deviation from this is indicative of the interaction between the electron spin and the magnetic field generated by the orbiting electron (spin-orbit coupling or SOC). Light atoms like carbon do not generate a large magnetic field and therefore exhibit very low SOC, whereas heavier atoms can affect the value of g significantly. In addition, the overall shape of the EPR spectrum provides information related to the orbitals containing the unpaired electron.

Atoms have electron spin and nuclear spin, therefore it stands to reason that the nuclear spin can interact with the electron spin. Like J-coupling in NMR, nearby nuclei can split the EPR signal resulting in multi-lined spectra. This is called hyperfine coupling (hfc). Hyperfine coupling can provide detailed insight into the position of an unpaired electron, like a radical for instance.

1.4.4 UV-vis-NIR spectroscopy / TD-DFT modeling

When an electron is removed from a substrate, a hole is formed either on the metal (higher oxidation state) or on the ligand (radical). Both situations will create large changes in the optical absorption spectrum, as new electronic transitions are possible notably because the "hole" can act as electron acceptor in these transitions. These transitions can be observed by UV-vis spectroscopy. Without any point of comparison, the position of these transitions cannot be assigned to specific processes. Using TD-DFT modeling, the value of UV-vis transitions are calculated and by comparing them to experimental values, one can understand the exact processes taking place. Furthermore,

when a radical is formed, promotion of an electron into the hole generates a signal in the near-infrared (NIR) region.

1.5 ORGANIZATION OF THE THESIS

This thesis is a manuscript-based report, i.e. each chapter is a formatted copy of a published or to-be-published manuscript. Even though each manuscript has an introduction to provide the reader with some background, a more detailed description of the approach and purpose is provided here while highlighting important aspects.

1.5.1 Chapter 2: Reversible Double Oxidation and Protonation of the Non-Innocent Bridge in a Nickel(II) Salophen Complex

Inspired by previous research by our collaborators and other groups, this manuscript details the first implementation and proof-of-concept of our methodology of substituting the central aromatic ring of a salophen complex with two dimethylamino groups. The hypothesis is that this modification will provide sufficient electron richness to the complex to not only direct the oxidation to the central aromatic ring (and away from the phenolates) but also lower the redox potential of the ligand such that two successive oxidation processes can occur under mild conditions.

For this work, the metal was chosen to be nickel(II). Nickel(II) is a diamagnetic metal in a square-planar geometry and thus provides sharp NMR signals. After oxidation, nickel(III) has a spin ½ which is ideal for EPR studies.

1.5.2 Chapter 3: Redox Non-Innocence of the Bridge in Copper(II)-Salophen and bis-Oxamato Complexes

The results from the Ni(II)TMTS manuscript were encouraging and paved the way for similar studies on more bio-available metals like copper(II). Two ligands were investigated: TMTS and TMopba (Scheme 1-9). Cu(II)TMTS complements the results previously found for Ni(II)TMTS while Cu(II)TMopba restricts the possibilities of radical formation as the ligand has only one aromatic moiety. In addition, since copper(II) is a paramagnetic metal, magnetic coupling is expected between the radical and the metal's unpaired electron.

1.5.3 Chapter 4: Implications of Strong Electron-Donating Groups in a Square-planar Cobalt(III) Complex

As the ligand is more electron-rich, the more easily the complex can be oxidized. This sparked the design of a new ligand. TMBAP contains amides instead of imines, which needed to be deprotonated in order to form a complex with a 2+ metal ion. The resulting complex had an overall 2– charge making it more electron-rich than the TMTS complexes and similar to the TMopba complexes. In addition, TMBAP should be more donor than TMopba because phenolates are more basic than carboxylates.

2. Reversible Double Oxidation and Protonation of the Non-Innocent Bridge in a Nickel(II) Salophen Complex

2.0 Notes on the Chapter

Drawing our inspiration from the work that has previously been done to mimic the active sites of redox metallo-enzymes, we developed a methodology to substitute a classic family of ligands, salophens, on the central aromatic ring with strong electron-donating dimethylamino groups. The hypothesis is that by making the ligand more electron-rich, the complex will be easier to oxidize. To date, researchers have studied the effects of electron-donating substituents on the phenolate moieties of these ligands or mildly electron donating groups on the central aromatic bridge. Their interest was centered around gaining an understanding of the role of the tyrosyl radical in the active sites of metallo-enzymes by modeling them with phenolates and probing the effects of substituents on these groups. The result of substitution with strong electron-donating groups was a localization of the "hole" formed by oxidation on one of the phenolates. If the substitution was done on the central aromatic moiety rather than the phenolates, would this direct the oxidation to the central ring? Of course, this moves away from biomimetics, as the goal is no longer to generate a phenoxyl radical but instead to attempt to relocate the locus of oxidation in a complex by tailoring the electronics of the ligand.

For characterization purposes, nickel(II) was used as the metal rather than the more bio-available copper(II) or the more catalytically active cobalt(II). In a square-planar geometry, nickel(II) is diamagnetic and thus provides sharp NMR signals. In addition,

oxidation of this diamagnetic complex leads to a species with only one unpaired electron (spin = ½), the electronic structure of which is easily analyzed by EPR.

2.1 INTRODUCTION

Combining the redox properties of a metal ion and an organic moiety constitutes an elegant methodology to access high formal oxidation states when the metal ion alone is insufficient to undergo all catalytic redox steps.[5,18] In metalloenzymes, organic cofactors such as the porphyrin of hemic systems[19] and tyrosine residues[20] can thus be transiently oxidized to radicals and promote efficient catalytic turnover. In chemical modeling, a number of ligand types are redox-active (non-innocent) when engaged within a complex[20,21] e.g., porphyrins,[22] phenolates,[23,24] catecholates,[25] aminophenolates,[26] phenylenediamines,[27] benzene-*N*-amidates,[28–31] and diimines.[32] In complexes with a non-innocent ligand, the locus of oxidation (or reduction) is dictated by the respective symmetry and energy of the frontier orbitals of the metal ion and those of the organic framework.[27] Thus, the oxidation site in a complex can be shifted from the metal to the ligand by tuning the electronics of the ligand. Our group previously investigated the oxidative chemistry of Ni(II) phenylenediaminebis(oxamato) complexes (Scheme 2-1), where the aromatic harbors substituents of various electron-donating properties. The strongly electron-donating dimethylamino substituents direct the oxidation site towards the aromatic part of the ligand, whereas a metal-centered oxidation process is observed for the parent, unsubstituted complex.[30] From a fundamental point of view, identifying new types of metallo-radical complexes will complement our knowledge on these intriguing species. In the present paper, we investigate the oxidative chemistry of the

Ni(II) complex **1** of the novel salophen ligand **5**, which incorporates a bis(NMe_2)-substituted aromatic bridge. We show that **1** undergoes two ligand-based, low-potential, reversible oxidations to yield a phenylenediamine radical $\mathbf{1}^{+}$ and an α-diiminoquinone species $\mathbf{1}^{2+}$, both being stable for hours.

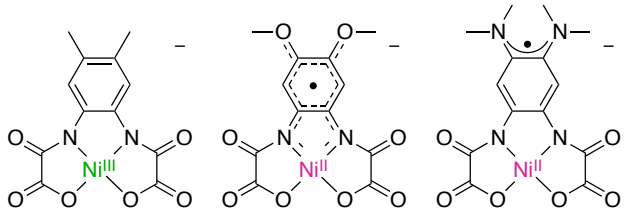

Scheme 2-1. Tuning the redox properties of an aromatic ligand by appropriate substitution, from a Ni(III) complex to a fully delocalized Ni(II)-radical species to a pure radical species.[30]

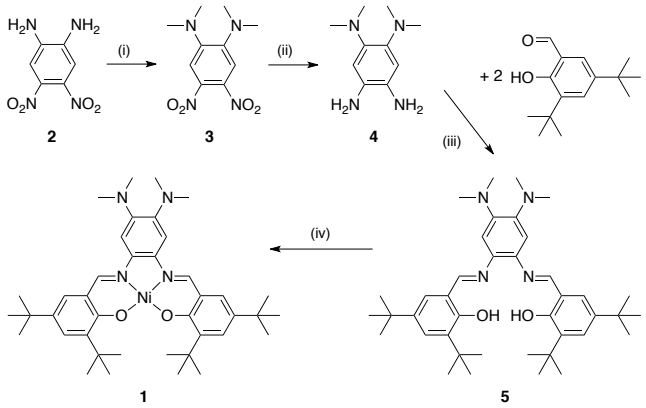

Scheme 2-2. Synthetic route towards **1**. (i) $(CH_2O)_n$, $NaBH_3CN$, AcOH, 89%; (ii) H_2, Pd/C, MeOH, quantitative; (iii) $HC(OMe)_3$, MeOH , 67%; (iv) $Ni(OAc)_2$, CH_2Cl_2/MeOH, 96%.

2.2 RESULTS AND DISCUSSION

2.2.1 Synthesis and structure of ligand and neutral nickel(II) complex

The synthesis of **5** is based on 4,5-diamino-1,2-dinitrobenzene, **2**,[33] a versatile precursor for benzene rings with distinct amino substitution at positions 1,2 and 4,5

(Scheme 2-2).[30,34,35] Metallation of **5** with Ni(II) acetate affords **1**, a diamagnetic complex as evidenced by sharp NMR signals both in $CDCl_3$ and in d^6-dmso. The aromatic protons H3 and H6 of **1** are more shielded (7.02 ppm) than in the MeO- (7.1 ppm)[36] or Me- (7.44 ppm)[15] substituted Ni(II)-salophen complexes, indicating that the central ring is electron-rich owing to the NMe_2 substituents. The crystal structure of **1** reveals the expected square-planar coordination environment that is typical of Ni(II) in a salophen cavity (Figure 2-1, Table 2-1).[15,36,37] A small puckering is induced by steric contact between the 6-*tert*-butyl substituents, as evidenced by a *ca*. 13° angle between the average planes defined by the central ring and each phenolate and a ca. 29° angle between the average phenolate planes. Due to steric contact between methyl groups of distinct NMe_2 substituents, the angle between the NMe_2 groups and the mean benzene plane is 55° in this solid-state structure, denoting limited resonance.

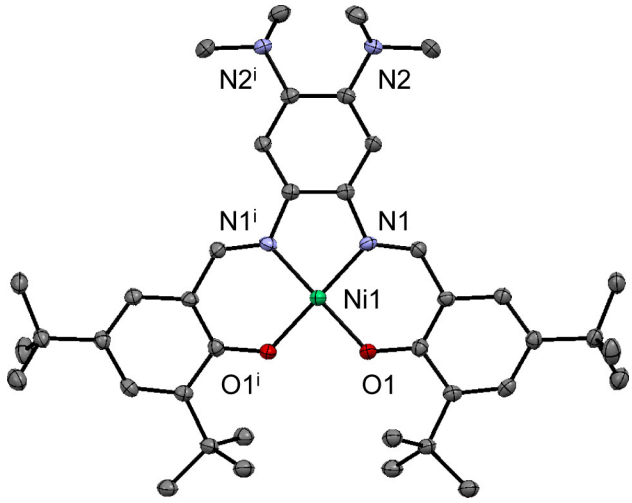

Figure 2-1. ORTEP representation at 50% ellipsoid probability of **1** (^{i}: *x*, *y*, 0.5-*z*). Hydrogen atoms were omitted for clarity. Selected bond lengths: Ni1-N1: 1.8504(17) Å; Ni1-O1: 1.8475(14) Å.

Table 2-1. Crystallographic data for **1** and [**1H**](SbF_6).

	1	[**1H**](SbF_6)
CCDC number	893505	893506
Empirical formula	$C_{40}H_{58}N_4NiO_2$	$C_{40}H_{57}F_6N_4NiO_2Sb$
Formula weight	683.60	920.36
Temperature	110(2) K	110(2) K
Wavelength	1.54178 Å	1.54178 Å
Crystal system	Monoclinic	Monoclinic
Space group	C2/c	$P2_1/c$
a	23.9521(7) Å	15.5147(3) Å
b	15.1711(4) Å	9.0739(2) Å
c	10.3912(3) Å	32.0739(6) Å
α	90°	90°
β	101.883(2)°	111.3800(10) °
γ	90°	90°
Volume	3695.03(18) $Å^3$	4204.59(15) $Å^3$
Z	4	4
Density (calculated)	1.229	1.454
Absorption coefficient	1.049	6.201
F(000)	1472	1896
Crystal size	0.03 × 0.05 × 0.56 mm	0.04 × 0.07 × 0.42 mm
Index ranges	$h = -28 \rightarrow 28$, $k = -18 \rightarrow 17$, $l = -12 \rightarrow 12$	$h = -18 \rightarrow 18$, $k = -10 \rightarrow 10$, $l = -38 \rightarrow 38$
Reflections collected	16344	56704
Independent reflections	3334	7678
Parameters	221	506
Goodness of fit	1.048	1.094
Final R indices [I > 2σ(I)]	$R_1 = 4.14\%$, $wR_2 = 9.76\%$	$R_1 = 3.826\%$, $wR_2 = 9.30\%$
R indices (all data)	$R_1 = 6.82\%$, $wR_2 = 11.11\%$	$R_1 = 4.68\%$, $wR_2 = 9.70\%$
Largest diff. peak and hole	0.535 and -0.457 e $Å^{-3}$	1.072 and -1.058 e $Å^{-3}$

2.2.2 Electrochemistry

The electrochemical behavior of the ligand and complexes has been studied in CH_2Cl_2 (+ 0.1 M nBu$_4$NClO$_4$ as supporting electrolyte) by cyclic voltammetry, differential pulse voltammetry and rotating disc electrode voltammetry. All potentials are referenced vs. the Fc^+/Fc couple.

The cyclovoltammogram (CV) of the free ligand **5** in CH_2Cl_2 displays two oxidation waves at $E_{1/2}^1$ = 0.07 V (ΔE_p = 0.06 V) and $E_{1/2}^2$ = 0.25 V (ΔE_p = 0.06 V), each corresponding to a one-electron process (Figure B-1). The first redox transfer is reversible, showing that the stability of the cation is noteworthy. In contrast, the low

I_p^a/I_p^c value for the second wave indicates that the dication is rather unstable, at least on the time scale of the experiment. Both oxidations of **5** occur at much lower potentials than for the phenoxyl/phenol couples in the parent salophen ligand (unsubstituted at the central ring, 0.74 V) and related salen ligands involving di-*tert*-butylphenol moieties (0.65-0.80 V).[38] $E_{1/2}^1$ and $E_{1/2}^2$ values for **5** are, however, within the range of those measured for the oxidation of a series of bis(NMe_2) aromatic derivatives. For example, oxidation of 1,4,5,8-tetrakis(dimethylamino)naphthalene occurs at $E_{1/2}^1$ = -0.01 and $E_{1/2}^2$ = 0.07 V, oxidation of 2,3,6,7-tetrakis(dimethylamino)naphthalene occurs at $E_{1/2}^1$ = 0.08 and $E_{1/2}^2$ = 0.16 V,[39,40] while *N*,*N*,*N*',*N*'-tetramethyl-*p*-phenylenediamine exhibits oxidation potentials of -0.21 and 0.38 V, the first one yielding the famous Würster's Blue salt.[41] The electron transfers observed for **5** are thus ascribed to sequential oxidations on the central tetraminobenzene ring into a radical cation and then a closed-shell α-diiminoquinone dication.

The CV of Ni(II) complex **1** in CH_2Cl_2 (Figures 2-2, B-2 and B-3) displays three quasi-reversible one-electron oxidation waves at $E_{1/2}^1$ = 0.12 (peak-to-peak separation $\Delta E_p = E_p^{a1} - E_p^{c1}$ = 0.11 V), $E_{1/2}^2$ = 0.24 V (ΔE_p = 0.11 V) and $E_{1/2}^3$ = 0.97 V (ΔE_p = 0.12 V). Typically, symmetrical Ni(II)-salen complexes with two di-*tert*-butylphenolate moieties exhibit two quasi-reversible one-electron oxidation waves above 0.4 V, which correspond to the successive oxidations of the phenolate moieties into phenoxyl radicals.[11,14,15,36,37,42–44] The low values of $E_{1/2}^1$ and $E_{1/2}^2$ values of **1** advocate for a different assignment, e.g. successive oxidations of the tetraaminobenzene central ring. This hypothesis is further supported by the close similarity between the oxidation potentials of **1** and free ligand **5**. The third redox wave of **1** is likely centered on the phenolate

moieties, but it has not been further investigated due to the low stability of the trication $\mathbf{1}^{3+}$.

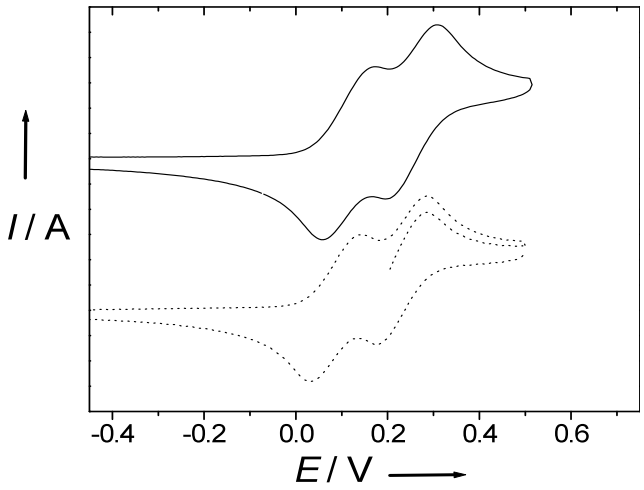

Figure 2-2. CV traces of 1 mM CH_2Cl_2 solutions (+0.1 M nBu$_4$NClO$_4$) of **1** (—) and electrogenerated $\mathbf{1}^{+}$ (···) at a carbon working electrode. Potentials are relative to the Fc^+/Fc redox couple. Scan rates: 0.1 V/s, T = 298 K.

For spectroscopic characterization, oxidized species $\mathbf{1}^{+}$ and $\mathbf{1}^{2+}$ were prepared either by bulk electrolysis at a fixed potential of 0.20 V or 0.42 V, respectively, or by chemical oxidation using one equivalent of acetylferrocenium (E = 0.27 V) or two equivalents of 1,1'-diacetylferrocenium (E = 0.49 V) in CH_2Cl_2, respectively.[45] Given the proximity of the first two oxidation processes of **1**, $\mathbf{1}^{+}$ disproportionates to **1** and $\mathbf{1}^{2+}$ with an equilibrium constant of *ca*. 1.0 x 10^{-3}. A solution sample of $\mathbf{1}^{+}$ would thus contain ~3% of each **1** and $\mathbf{1}^{2+}$. This phenomenon was taken into account when analyzing the spectroscopic data. Both preparation methods gave similar results, but the oxidized species were more stable time-wise under the chemical oxidation conditions. For example, a solution of dication $\mathbf{1}^{2+}$, obtained via chemical oxidation was left standing for 4 h under inert atmosphere. Further reduction of this solution with ferrocene and analysis

of the products after chromatography indicated >95% recovery of **1**, thus evidencing a noticeable stability of the dication.

2.2.3 EPR spectroscopy

The 25 K EPR spectrum of $\mathbf{1}^{+}$ in CH_2Cl_2 consists of an isotropic (S = ½) radical signal centered at g_{iso} = 2.004 (Figure B-4). This suggests a lack of metal character in the SOMO of $\mathbf{1}^{+}$ and argues against a Ni(II)-phenoxyl radical formulation, as such species are known to have higher g_{iso} values (typically 2.03 for salen precursors involving 2,4-di-*tert*-butylphenolate moieties).[11,14,15,36,37,42–44] More information about the oxidation site in $\mathbf{1}^{+}$ is provided by its isotropic EPR spectrum in CH_2Cl_2 at 293 K (Figure 2-3). Under these conditions the (S = 1/2) signal is still observed at g_{iso} = 2.004, but a hyperfine splitting corresponding to the interaction of the electron spin with hydrogen and nitrogen nuclei could be evidenced. From simulation of the spectrum the following isotropic hyperfine coupling (HFC) constants were obtained: 13.7 MHz for 6 equivalent ^{1}H nuclei, 17.7 MHz for 6 equivalent ^{1}H nuclei and 14.4 MHz for 2 equivalent ^{14}N nuclei. The high HFC values to nitrogen atoms rule out a phenoxyl character for the radical species. Instead, the HFC pattern indicates that the radical is delocalized over the two NMe_2 substituents without significant contribution of neither iminic nitrogens nor the Ni center.[41,46] We calculated the EPR parameters by DFT methods with the ORCA EPR-II package (see below for more DFT details). The calculated HFC are A_{6H} = 13.7 MHz, A_{6H} = 16.7 MHz, A_{2N} = 12.9 MHz, with a highly isotropic g-matrix (g_1 = 2.0018, g_2 = 2.0047, g_3 = 2.0065; g_{iso} ~ 2.004). The very good agreement between experimental and theoretical EPR data

confirms the assignment of $\mathbf{1}^{+}$ as a π-radical localized on the central bis(NMe_2)benzene ring.

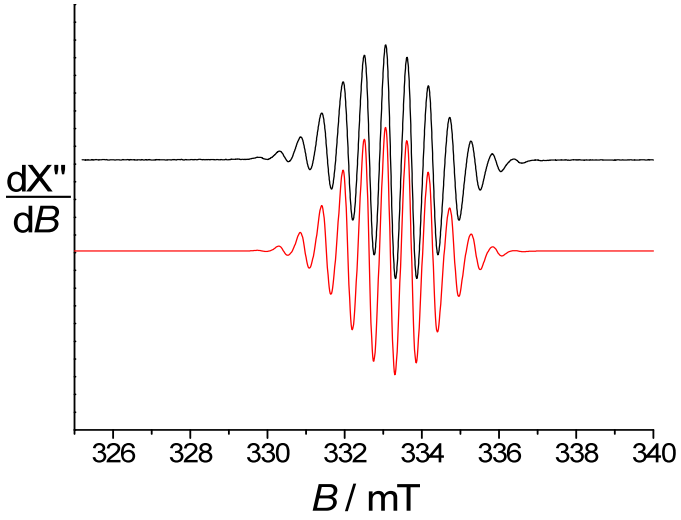

Figure 2-3. X-band EPR spectrum of the electrochemically generated $\mathbf{1}^{+}$ in CH_2Cl_2. Black lines: experimental spectrum; red lines: simulation using the parameters given in the text. T = 293 K, microwave power: 4 mW, microwave freq.: 9.33 GHz, mod. amp.: 0.05 mT, mod. freq.: 100 kHz.

The dication $\mathbf{1}^{2+}$ is EPR-silent in CH_2Cl_2 both at 20 K and 100 K, consistent with a diamagnetic character of the doubly oxidized ligand (see below).

2.2.4 DFT calculations

DFT calculations were undertaken at the B3LYP level of theory with the ORCA package in order to get insight into the geometric and electronic structures of the oxidized species. The structures of the oxidized species $\mathbf{1}^{+}$, $\mathbf{1}^{2+}$ and protonated radical $(\mathbf{1H})^{2+}$, as well as the initial complexes **1** and $\mathbf{1H}^{+}$ for comparison, were investigated by geometry optimization. Except for the putative radical species $(\mathbf{1H})^{2+}$ (chemically irrelevant, see below for protonation studies), the optimized structures are found to be symmetrical. A

reasonable agreement was found between the calculated and experimental bond lengths for complexes **1** (Table 2-2, Figure B-9) and **1H$^+$** (Table B-1, Figure B-11). In the case of **1^{2+}**, the electronic description is complicated by the need to consider two spin states, singlet and triplet, hereafter noted ^{1}**1**$^{2+}$ and ^{3}**1**$^{2+}$, respectively (Figure B-10). We calculated the energy gap between the optimized singlet and triplet forms and found that the singlet was stabilized by 13.0 kJ/mol (including solvation terms). The singlet spin state is therefore likely the ground spin state of **1^{2+}**.

Table 2-2. Selected experimental and calculated bond lengths (Å) for **1**, **1$^+$** and **1^{2+}**.[a]

Bond	**1** (exp)	**1** (calcd)	**1**$^+$(calcd)	^{1}**1**$^{2+}$ (calcd)	^{3}**1**$^{2+}$ (calcd)
nature	closed shell	closed shell	radical	Singlet closed shell	Triplet open shell
Ni-O	1.848	1.883	1.881	1.890	1.869
Ni-N1	1.850	1.885	1.884	1.895	1.875
C1-O1	1.310	1.299	1.291	1.280	1.287
C1-C2	1.438	1.444	1.446	1.448	1.449
C2-C3	1.379	1.382	1.378	1.373	1.378
C3-C4	1.412	1.418	1.425	1.435	1.421
C4-C5	1.369	1.371	1.366	1.360	1.380
C5-C6	1.419	1.420	1.426	1.432	1.407
C1-C6	1.419	1.430	1.440	1.457	1.444
C6-C7	1.420	1.417	1.403	1.386	1.412
C7-N1	1.310	1.305	1.317	1.364	1.309
N1-C8	1.419	1.414	1.395	1.364	1.407
C8-C9	1.394	1.398	1.383	1.379	1.377
C9-C10	1.387	1.395	1.407	1.411	1.413
C10-C10'	1.428	1.440	1.462	1.500	1.460
C8-C8'	1.382	1.393	1.427	1.472	1.420
C10-N3	1.420	1.408	1.365	1.325	1.358

[a]: Atom numbering used:

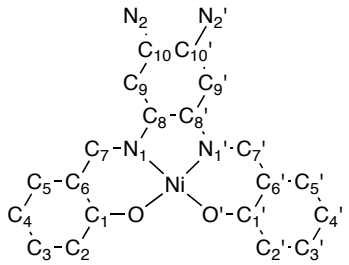

Metrical analysis of the calculated **1** and $\mathbf{1}^{+}$ structures supports the locus of oxidation being on the central ring (Table 2-2, Figure B-9). Examination of the C-C and C-O bond lengths within the phenolic rings of **1** and $\mathbf{1}^{+}$ reveals that no significant change occurs upon oxidation, the bond lengths being similar within ±0.01 Å while the N-Ni and O-Ni bond lengths do not vary by more than 0.002 Å. The C-C and C-O bond lengths in the phenolic rings of $\mathbf{1}^{+}$ are all in the range expected for a bis(phenolate) character. In contrast, clear metrical changes are observed within the bis(NMe_2)benzene fragment on going from **1** to $\mathbf{1}^{+}$ (Table 2-2). The shortening of C10-N3 and C8-C9 bonds, concomitant with the lengthening of C10-C10' and C8-C8', highlights a quinoidal distribution of bond lengths within the tetraminobenzene ring in $\mathbf{1}^{+}$.[12] This is strong evidence that oxidation of **1** occurs on the bridge, affording a phenylene π-radical $\mathbf{1}^{+}$. Interestingly, the magnitude of the C10-N3 shortening (0.043 Å) is much larger than for the C8-N1 bonds (0.019 Å), suggesting that the radical character in $\mathbf{1}^{+}$ prevails on the 4,5-diaminobenzene rather than the 1,2,4,5-tetraminobenzene fragment.

The energetically favored singlet spin state of $\mathbf{1}^{2+}$, $^{1}\mathbf{1}^{2+}$, displays phenolic C-C and C-O bond lengths that are very close to those calculated for **1** and $\mathbf{1}^{+}$, and thus has a bis(phenolate) character (Table 2-2, Figure B-10). The bonds in the central ring of $^{1}\mathbf{1}^{2+}$ display the same trend as was observed on going from **1** to $\mathbf{1}^{+}$, i.e. an α-diiminoquinone character showing that double oxidation occurs on the electron-rich bridge of **1**. Interestingly, the angles between the NMe_2 substituents and the central ring in both $\mathbf{1}^{+}$ and $^{1}\mathbf{1}^{2+}$ are small (18 and 14°, respectively) compared with that in **1** (55°), evidencing a strong participation of the NMe_2 groups in the resonance stabilization of the oxidized species.[47]

The geometric structure of the triplet $\mathbf{1}^{2+}$, $^{3}\mathbf{1}^{2+}$, is consistent with a diradical character (Table 2-2, Figure B-10). Comparison of the metrical parameters of $^{3}\mathbf{1}^{2+}$ with those of $\mathbf{1}^{+}$ shows that some bonds within the phenolic rings are altered by oxidation: in particular, C5-C6 is shortened by 0.019 Å and C4-C5 is lengthened by 0.015 Å. These features are indicative of a phenoxyl character for $^{3}\mathbf{1}^{2+}$,[12] the radical being equally shared between the two peripheral rings of the molecule. In agreement with this assumption, comparison of the bond lengths within the central radical ring of $\mathbf{1}^{+}$ and $^{3}\mathbf{1}^{2+}$ does not reveal any significant difference. Therefore, the $^{3}\mathbf{1}^{2+}$ is better described as a diradical involving both delocalized phenoxyl moieties and a bis(NMe_2)benzene π-radical unit.

Consistent with the above bond length analysis, the calculated SOMO of $\mathbf{1}^{+}$ is essentially located on the bis(NMe_2)benzene fragment (75%) with a small contribution from the salicylimines (25%, Figure 2-4a). Not surprisingly, the LUMO of the singlet dication $^{1}\mathbf{1}^{2+}$ corresponds to the SOMO of $\mathbf{1}^{+}$ (Figure 2-4b; 75% bis(NMe_2)benzene fragment and 25% salicylimines). The two SOMOs of the triplet diradical $^{3}\mathbf{1}^{2+}$ are shown in Figure 2-4c. One has a main bis(NMe_2)benzene character (95%), with a small contribution of the salicylimines (5%). The other has a main salicylimine character (85%), with small contributions of the bis(NMe_2)benzene central ring (5%) and a nickel d_{xz} orbital (10%).

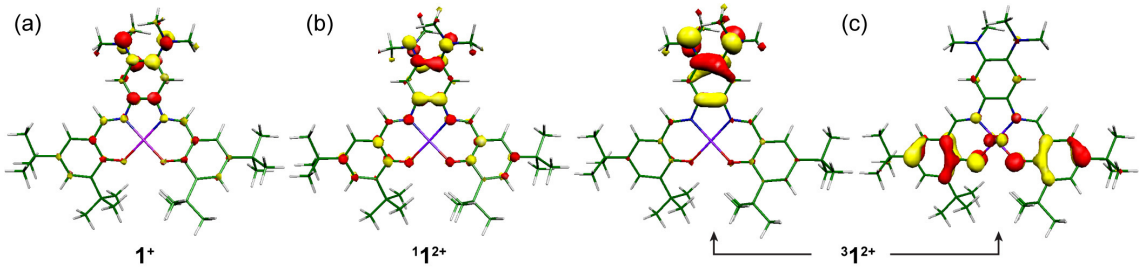

Figure 2-4. Localized molecular orbitals: (a) SOMO of $\mathbf{1}^{+}$, (b) LUMO of singlet $^{1}\mathbf{1}^{2+}$, (c) SOMOs for triplet diradical $^{3}\mathbf{1}^{2+}$. See text for fragment composition analysis.

The individual contributions of the atoms to the spin density confirm the assignments made above (Table 2-3, Figure B-12). In the case of $\mathbf{1}^{+}$, the spin density is found exclusively on the central ring and the nitrogens of the NMe_2 substituents, with negligible contribution from the phenolates or imine moieties. In the case of $^{3}\mathbf{1}^{2+}$, the coefficients are essentially the same on the central ring and NMe_2 substituents as in $\mathbf{1}^{+}$, with the addition of a radical character on the phenolic moieties, thereby confirming this species as a multi-site diradical.

Table 2-3. Individual contributions of the atoms to the spin density in $\mathbf{1}^{+}$ and triplet $^{3}\mathbf{1}^{2+}$.[a]

Atoms	$\mathbf{1}^{+}$	$^{3}\mathbf{1}^{2+}$	Atoms	$\mathbf{1}^{+}$	$^{3}\mathbf{1}^{2+}$
Ni	0	0.10	C5	0	0
O	0	0.15	C6	0.02	0.10
N1	0.02	0	C7	0.02	0
C1	0	0	C8	0.11	0.07
C2	0	0.06	C9	0	0
C3	0	0	C10	0.10	0.09
C4	0	0.13	N2	0.22	0.26

[a]: See Table 2-2 for atom numbering.

2.2.5 Electronic spectra and TD-DFT calculations

Oxidation of **1** to $\mathbf{1}^{+}$ and $\mathbf{1}^{2+}$ leads to drastic changes in their electronic absorption spectra. In contrast to **1**, both the orange-brown $\mathbf{1}^{+}$ and the brown $\mathbf{1}^{2+}$ exhibit intense absorptions in the vis-NIR range (Figure 2-5, Table 2-4). The extinction coefficients of these absorptions are reminiscent of charge-transfer bands. Noteworthy, $\mathbf{1}^{+}$ displays no significant absorption at wavenumbers lower than 8,000 cm^{-1} (Figure 2-5b), in sharp contrast with the Ni(II) phenoxyl-radical salen complexes that typically exhibit an intense intervalence charge-transfer (IVCT) band at 4300-4700 cm^{-1} (17-25 $mM^{-1}cm^{-1}$).[11,14,43,44] The red-shift of the vis-NIR features of $\mathbf{1}^{2+}$ (Figure 2-5c) compared with $\mathbf{1}^{+}$ likely reflects an increase in the ligand oxidation state.

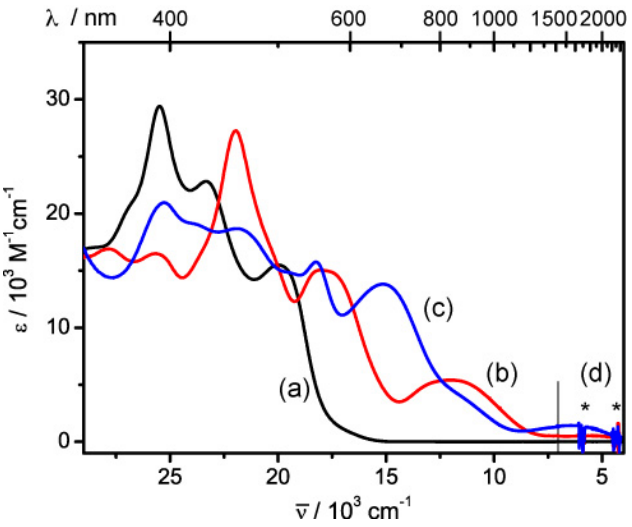

Figure 2-5. (a-c) UV-vis-NIR spectra of: **1** (a, black), $\mathbf{1}^{+}$ (b, red), $\mathbf{1}^{2+}$ (c, blue) generated by spectroelectrolysis at -30°C (1 mM in CH_2Cl_2, 0.1 M $n$$Bu_4NPF_6$). (d) Extension of the (a-c) spectra in the 1400-2800 nm range as per chemical oxidation of **1** with Ac_2Fc^{+} in CH_2Cl_2. The asterisks denote solvent absorptions.

The UV-vis-NIR spectrum of the radical-cation $\mathbf{1}^{+}$ is well matched by the electronic excitations predicted by TD-DFT calculations (Table 2-4). In particular, the calculations

confirm the absence of an intense IVCT transition in the NIR that would have indicated a mixed-valance phenolate-phenoxyl radical system.[11,14,43,44] The three lowest-energy absorptions are rising from interligand charge-transfer (ILCT) transitions (Figure 2-6). In the βHOMO → βLUMO transition at 12 000 cm^{-1}, the donor orbital is a π system mainly located on the phenolate rings, while the acceptor orbital (βLUMO) is principally located on the central bis(NMe_2)benzene fragment with a small contribution from the phenolate moieties. The next two absorptions stem from βHOMO-1 → βLUMO and βHOMO-3 → βLUMO transitions, respectively. The donor orbitals are again ligand-centered, with the βHOMO-1 being a π system mainly located on the phenolate rings and the βHOMO-3 being a π system delocalized over the whole salophen backbone with dominant contributions of the phenolates and central ring.

Table 2-4. Electronic transitions of $\mathbf{1}^{+}$ and $\mathbf{1}^{2+}$ (singlet: $^{1}\mathbf{1}^{2+}$, triplet: $^{3}\mathbf{1}^{2+}$).

	Experimental ν, cm^{-1} (ε, M^{-1} cm^{-1})	TD-DFT ν, cm^{-1} (f)	Assignment[a]
$\mathbf{1}^{+}$	12 000 (5 410)	11 592 (0.019)	βHOMO→βLUMO, IL
	18 000 (15 000)	18 112 (0.120)	βHOMO-1→βLUMO, IL
	22 000 (27 300)	24 409 (0.307)	βHOMO-3→βLUMO, IL
$^{1}\mathbf{1}^{2+}$	6 250 (1 430)	5 777 (0.102)	αHOMO→αLUMO, IL
	12 000 (shoulder)	12 991 (0.011)	αHOMO-2→αLUMO, IL
	15 100 (13 800)	16 674 (0.145)	αHOMO-3→αLUMO, IL
	18 250 (15 750)	18 988 (0.171)	αHOMO-7→αLUMO, ML
$^{3}\mathbf{1}^{2+}$		6 920 (0.26)	βHOMO→βLUMO, IL
		10 315 (0.15)	βHOMO-1→βLUMO, ML

[a] IL: intraligand charge-transfer, ML: metal-to-ligand charge-transfer.

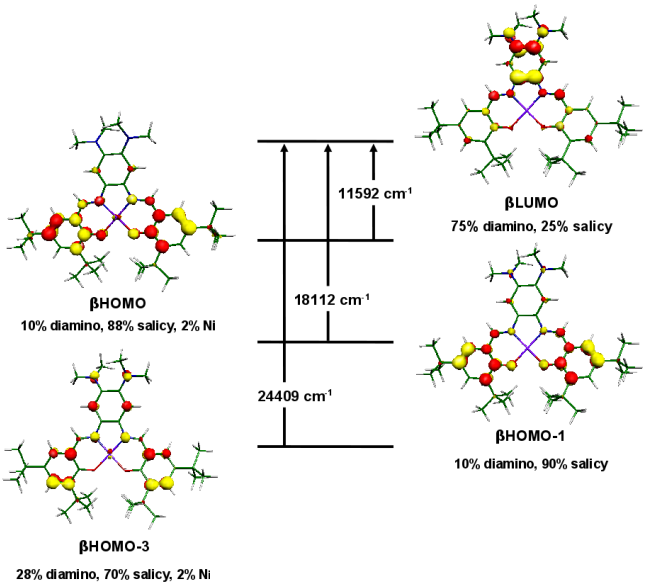

Figure 2-6. TD-DFT assignment of the main electronic excitations of $\mathbf{1}^{+}$. The fragment population of the relevant MOs is indicated in parentheses. Fragments: Ni = nickel atom, salicy = salicylimine moieties (phenolate rings + imines), diamino = central ring + NMe_2 substituents.

TD-DFT calculations on $\mathbf{1}^{2+}$ were conducted by considering both the singlet and triplet spin states (Table 2-4). Only the set of excitations for the singlet species reproduces the experimental bands and thus supports a singlet nature of $\mathbf{1}^{2+}$, further confirming the energetic analysis. A detailed analysis of the composition of the MOs involved in the transitions reveals that the absorptions at 6 250, 12 000 and 15 100 cm^{-1} stem from ILCT transitions, while the band at 18 250 cm^{-1} corresponds to a MLCT transition (Figure 2-7). In particular, the βLUMO and βHOMO of $^{1}\mathbf{1}^{2+}$ have essentially the same character as in $\mathbf{1}^{+}$, but the relative energy of these orbitals in $^{1}\mathbf{1}^{2+}$ differ greatly from the situation in $\mathbf{1}^{+}$. The highest oxidation state and non-radical nature of the central ring in $\mathbf{1}^{2+}$ contributes to a stabilization of the βLUMO and leads to an overall red shift of the spectrum for $\mathbf{1}^{2+}$ compared with $\mathbf{1}^{+}$.

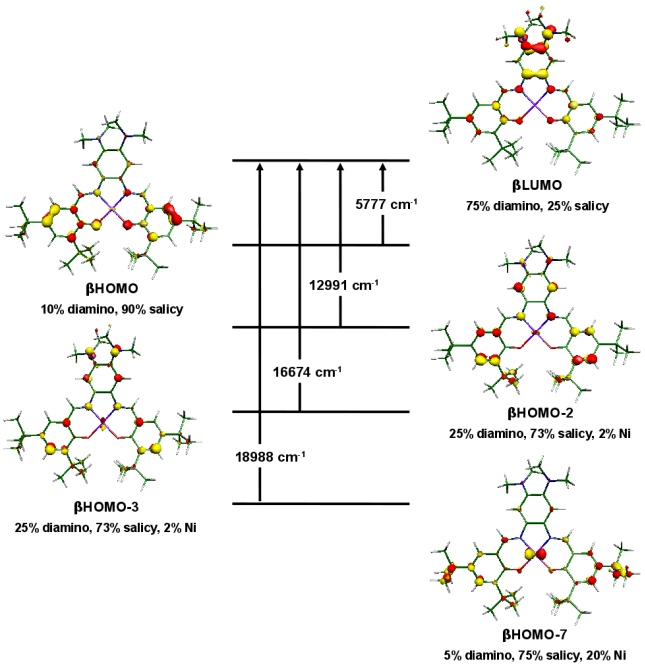

Figure 2-7. TD-DFT assignment of the main electronic excitations of singlet $\mathbf{1}^{2+}$. The fragment population of the relevant MOs is indicated in parentheses. Fragments: Ni = nickel atom, salicy = salicylimine moieties (phenolate rings + imines), diamino = central ring + NMe_2 substituents.

In the hypothetical triplet diradical $^3\mathbf{1}^{2+}$, the main electronic excitations arise from βHOMO → βLUMO and βHOMO-1 → βLUMO transitions (Figure 2-8). Similarly to Ni(II) phenoxyl radical salen complexes, the βHOMO → βLUMO excitation corresponds to an IVCT, where both the donor and acceptor orbitals have a strong phenolate/phenoxyl character. According to previous studies,[11,14,43,44] and consistent with the calculated oscillator strength of the 6 920 cm^{-1} band, this transition should give rise to a very intense band in the NIR, in contrast to what is observed experimentally. This is again in favor of a singlet description for $\mathbf{1}^{2+}$.

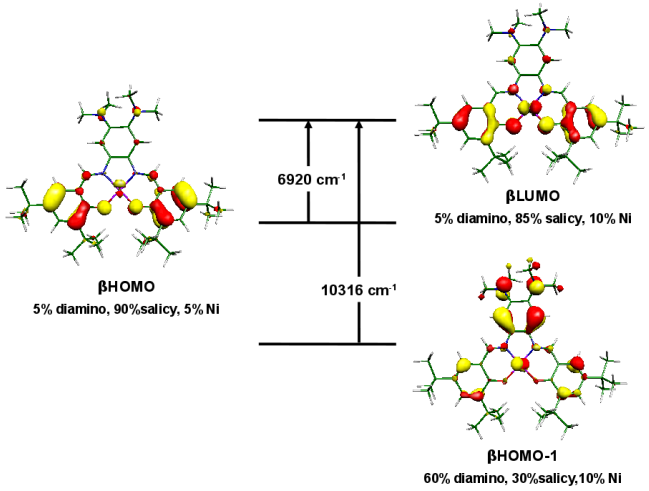

Figure 2-8. TD-DFT assignment of the main electronic excitations of triplet $\mathbf{1}^{2+}$. The fragment population of the relevant MOs is indicated in parentheses. Fragments: Ni = nickel atom, salicy = salicylimine moieties (phenolate rings + imines), diamino = central ring + NMe_2 substituents.

2.2.6 Protonation studies

By virtue of its NMe_2 substituents, complex **1** can be protonated with a strong acid (HBF_4 or $HSbF_6$). The process was monitored by UV-vis spectroscopy (Figure 2-9) and yielded a complex with similar optical features as **1**, though less intense. Addition of a base to the acidic solution led to full recovery of the UV-vis features of **1**, demonstrating the reversibility of the process. On a preparative scale, using $HSbF_6$ in methanol led to the isolation of crystals of [**1H**](SbF_6) that were suitable for X-ray diffraction analysis. The crystal structure of [**1H**](SbF_6) confirmed that protonation occurred on a NMe_2 group, with hydrogen-bonding to the other (Figure 2-10). Consequently, the NMe_2 groups are facing each other and are no longer related by a C_2 axis as was the case in **1**. The $\mathbf{1H}^+$ molecule is more planar than **1** in their respective solid-state structure, with only an 8.3° angle between the carbon rings of each phenolate.

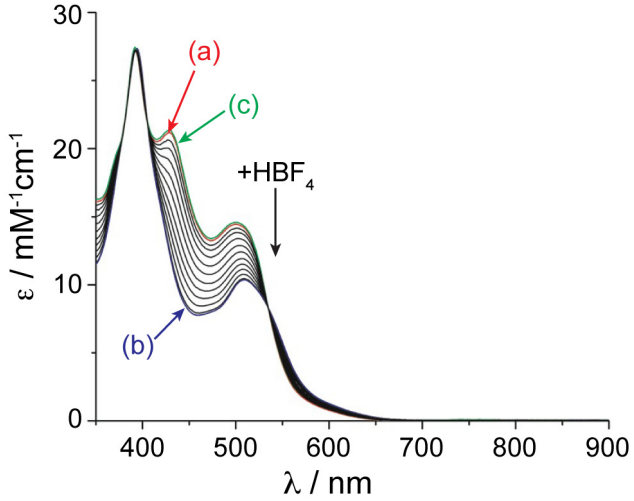

Figure 2-9. UV-vis titration of a CH_2Cl_2 solution of **1** by HBF_4. (a, red) before addition of acid; (b, blue) after 1 eq. of acid; (c, green) after 1 eq. of acid and 8 eq. of NEt_3. l = 1.000 cm, T = 298 K.

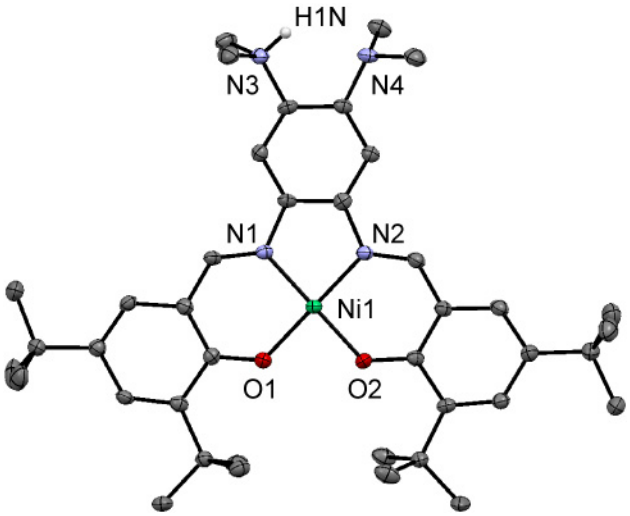

Figure 2-10. ORTEP representation at 50% ellipsoid probability of the cationic part of [**1H**](SbF_6). Hydrogen atoms, except the one located between the NMe_2 substituents, were omitted for clarity. Selected bond lengths: Ni1-N1: 1.851(3) Å; Ni1-N2: 1.864(3) Å; Ni1-O1: 1.862(2) Å, Ni1-O2: 1.852(2) Å.

Protonation studies confirmed the involvement of the NMe_2 substituents in the redox behavior of **1**. The CV of **1H**$^+$ revealed a two-electron process (based on coulometry) with E_p^{a1} = 0.57 V and E_p^{c1} = 0.21 V (Figure 2-11). The protonation-induced increase by

more than 300 mV of E_p^{a1} compared with **1** is consistent with the NMe_2 substituents being significant contributors to the orbital from which the electron is abstracted in **1**. The large peak-to-peak separation, ΔE_p = 0.36 V, indicates that a chemical reaction is coupled to the electron transfer. The similarity between E_p^{c1} of $\mathbf{1H^+}$ and $E_{1/2}{}^2$ of **1** suggests that a significant amount of dication $\mathbf{1^{2+}}$ (and likely monocation $\mathbf{1^+}$) is formed during oxidation of $\mathbf{1H^+}$. In addition, the CV recorded after complete electrolysis at 0.6 V is not superimposable to that of $\mathbf{1H^+}$ and displays an additional feature at 0–0.3 V which is reminiscent of the CV of **1** (Figure 2-11). These results suggest that oxidation of $\mathbf{1H^+}$ affords a transient acidic radical species that deprotonates readily to produce $\mathbf{1^+}$. The E_p^{a1} value of $\mathbf{1H^+}$ being higher than $E_{1/2}{}^2$ of $\mathbf{1^+}$, the net result is a two-electron oxidation of $\mathbf{1H^+}$ into $\mathbf{1^{2+}}$ and proton release in solution (Scheme 2-3).

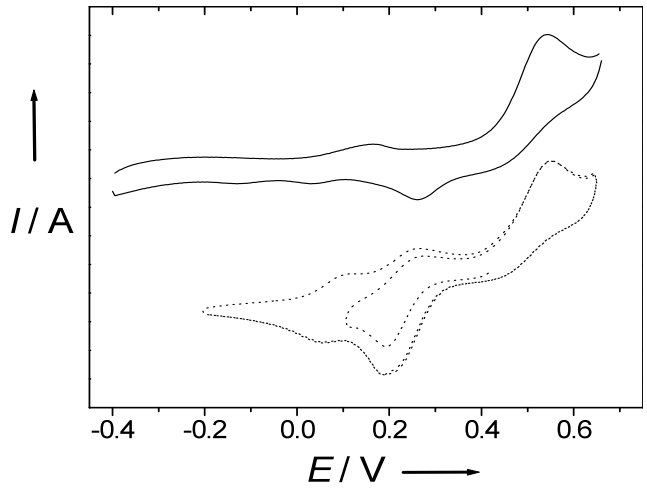

Figure 2-11. CV traces of 1 mM CH_2Cl_2 solutions (+0.1 M nBu$_4$NClO$_4$) of $\mathbf{1H^+}$ before (—) and after (···) electrolysis at 0.6 V at a platinum working electrode. Potentials are relative to the Fc^+/Fc redox couple. Scan rates: 0.1 V/s, T = 298 K.

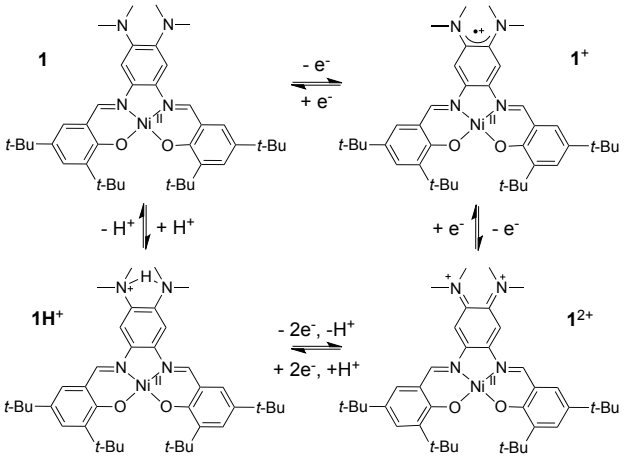

Scheme 2-3. Protonation/Oxidation processes from **1**.

The electrochemical oxidation of **1H**$^{+}$ at 0.62 V (i.e. at a potential slightly higher than E_p^{a1}) was monitored by EPR spectroscopy at 298 K. The EPR spectrum recorded at half electrolysis (one electron removed) consisted of a signal very similar to the one of **1**$^{+}$, albeit much less intense (Figure B-6), while two-electron oxidation (complete electrolysis) resulted in a total quenching of the EPR signal. This behavior is consistent with **1**$^{2+}$ being the final oxidation product, with a small amount of **1**$^{+}$ being transiently formed during electrolysis. In order to confirm this oxidation scheme, we calculated the EPR parameters for a putative protonated (S = ½) radical species **(1H)**$^{2+}$ by DFT methods (Figure B-14). The computed EPR parameters are g_1 = 1.990, g_2 = 2.018, g_3 = 2.049 (g_{iso} ~ 2.019) without any HFC higher than 3 MHz, consistent with the location of the radical on the salicylimine moieties (Figure B-13). The poor agreement between these calculated values and the experimental data confirm that a protonated radical species **(1H)**$^{2+}$ is not realistic under the experimental conditions.

UV-vis-NIR monitoring of the electrochemical oxidation of $\mathbf{1H^+}$ (0.62 V, two electrons removed) showed the appearance of absorption bands at 15 100 and 18 320 cm^{-1} indicating >95% formation of $\mathbf{1^{2+}}$ (Figure B-8). All data thus suggest that the radical dication $\mathbf{1H^{2+}}$ is very acidic. It is easily deprotonated, making oxidation of $\mathbf{1H^+}$ a proton-coupled two-electron transfer to afford $\mathbf{1^{2+}}$ (Scheme 2-3).

2.3 CONCLUSION

In summary, the two NMe_2 substituents in salophen-type Ni(II) complex **1** direct the first two oxidation processes onto the central ring. Complex **1**, together with radical $\mathbf{1^+}$ and α-diiminoquinone $\mathbf{1^{2+}}$, constitute a rare example in the salophen family where the neutral part of the molecule, not the phenolates, gets oxidized by one[13] and two electrons reversibly. In these nickel(II) complexes, ligand **5** is thus found in three different oxidation states (2-, - and neutral) that are reversibly accessible at low redox potentials. Implication of the redox non-innocence of **5** onto complexes with other metal ions is underway.

2.4 EXPERIMENTAL

2.4.1 Materials

Organics, solvents and metal salts were obtained from commercial sources and used as received unless indicated otherwise. For oxidation studies, dichloromethane was degassed and dried over an MBraun solvent purification system, then stored over activated 4Å molecular sieves in amber bottles inside an inert-atmosphere glovebox (MBraun Labmaster) filled with dry N_2 atmosphere (less than 1 ppm in dioxygen and

water). Compound **2**[33] and 3,5-di-*t*-butylsalicylaldehyde[48] were synthesized following literature procedures.

2.4.2 Characterization

Elemental CHN microanalyses were performed by the Microanalytical Service of the Institut de Chimie des Substances Naturelles (CNRS, France). Solution ^{1}H and ^{13}C NMR spectra were recorded on a Varian Inova 500 MHz instrument using tetramethylsilane as internal reference. FT-IR spectra were recorded on a Perkin-Elmer 882 spectrophotometer as KBr pellets. UV-vis-NIR solution spectra were recorded on Varian CARY 5E (250-1400 nm) and 5000 (1400-3300 nm) spectrophotometers. X-Band EPR spectra were recorded on a Bruker EMX Plus spectrometer controlled with the Xenon software and equipped with a Bruker teslameter. A Bruker nitrogen flow cryostat connected to a high sensitivity resonant cavity was used for 100 K measurements. An Oxford Instrument helium flow cryostat connected to a dual mode resonant cavity was used to run experiments at 25 K. The spectra were simulated using the SIMFONIA software (Bruker). Cyclic voltammetry (CV) curves were recorded on a CHI 620 potentiostat in a standard three-electrode cell under Argon atmosphere. Electrochemical measurements were performed either at 298 K for the non-oxidized complexes or 243 K for the oxidized species to ensure as little decomposition as possible. An $AgNO_3$/Ag (0.01 M) reference electrode was used. All the potentials given in the text are referred to the regular Fc^+/Fc redox couple used as external reference. A vitreous carbon disc electrode (3 mm diameter) or a platinum disc (2 mm diameter) polished with 1 mm diamond paste was used as working electrode. Both the carbon and platinum working

electrodes gave the same response for **1**. In the case of $\mathbf{1H^+}$ we observed significant deposition at the carbon working electrode, which was avoided by using a platinum one. Electrolysis was performed on a PAR 273 potentiostat, under Argon atmosphere at -40°C. The set-up for bulk electrolyses consisted of carbon felt electrode (for **1**) or a large platinum grid (for $\mathbf{1H^+}$), while the counter-electrode was also isolated by a salt bridge. RDE voltammetry was performed with a Radiometer TCV101 speed control unit and an EDI 101 electrode.

2.4.3 X-ray crystallography

X-ray crystallographic analysis was performed using the microfocus Cu-Kα source of a Bruker APEX-DUO diffractometer. The frames were integrated with the Bruker SAINT software package using a narrow-frame algorithm. Data were corrected for absorption effects using the multi-scan method (SADABS). The structures were solved by direct methods and refined using the Bruker APEX2 software Package (SHELXL instructions).[49] All non-hydrogen atoms were refined with anisotropic thermal parameters. Hydrogen atoms were generated in idealized positions, riding on the carrier atoms, with isotropic thermal parameters, except for H1N in [**1H**](SbF_6) which was located on the electronic density difference map and allowed to refine with only a distance restraint from N3.

2.4.4 Computational details

All theoretical calculations were performed with the ORCA program package.[50] Full geometry optimizations were carried out for all complexes using the GGA functional

BP86[51–53] in combination with the TZV/P[54] basis set for all atoms and by taking advantage of the resolution of the identity (RI) approximation in the Split-RI-J variant[55] with the appropriate Coulomb fitting sets.[56] Increased integration grids (Grid4 in ORCA convention) and tight SCF convergence criteria were used. Solvent effects were accounted for according to the experimental conditions. For that purpose, we used the CH_2Cl_2 ($\varepsilon = 9.08$) solvent within the framework of the conductor-like screening (COSMO) dielectric continuum approach.[57] The relative energies were obtained from single-point calculations using the B3LYP[58,59] functional together with the TZV/P[54] basis set. They were computed from the gas-phase optimized structures as a sum of electronic energy, thermal corrections to free energy, and free energy of solvation. Optical properties were also obtained from single-point calculations using the hybrid functional B3LYP[58,59] and the TZV/P[54] basis set. Electronic transition energies and dipole moments for all models were calculated using time-dependent DFT (TD-DFT)[60–62] within the Tamm-Dancoff approximation.[63,64] To increase computational efficiency, the RI approximation[65] was used in calculating the Coulomb term and at least 30 excited states were calculated in each case. g-tensors and hyperfine coupling constants were obtained from single-point calculations employing the hybrid functional B3LYP.[58,59] The triply polarized core property basis set CP(PPP)[66] was applied for the metal while the EPR-II[67] basis set was used for all remaining atoms. Special care was also taken to ensure accurate results by increasing the size of the integration grid to 7 (ORCA convention) for the metal center.[66]

2.4.5 Syntheses

3 (4,5-bis(dimethylamino)-1,2-dinitrobenzene): To a degassed suspension of **2**[33] (5.5 g, 27.7 mmol) and paraformaldehyde (8.3 g, 276 mmol) in glacial acetic acid (50 mL) was added sodium cyanoborohydride (8.75 g, 139 mmol) in small portions. The suspension was then stirred overnight at room temperature under inert atmosphere. The solid was filtered off and rinsed with acetone. The filtrate was evaporated to dryness and dichloromethane and water were added. The product was extracted two times and the combined organic phases washed once with water, dried over sodium sulfate and evaporated to dryness. The resulting oil was dissolved in 50 mL of diethyl ether, filtered over cotton, and evaporated to a minimum. 500 mL of cold hexanes was added and the suspension was kept in a –20°C freezer overnight to yield a dark red crystalline material that was filtered off and dried under vacuum. Yield: 6.25 g, 89%. Anal. Calcd for $C_{10}H_{14}N_4O_4$ (254.2 g/mol): C 47.24, H 5.55, N 22.04. Found: C 46.88, H 5.53, N 21.92. ^{1}H NMR ($CDCl_3$, 500 MHz): δ 2.87 (s, 12H), 7.21 (s, 2H). ^{13}C NMR ($CDCl_3$, 125 MHz): δ 40.41, 113.62, 136.43, 146.73. FT-IR (KBr): ν 1505, 1520, 1544, 1572, 1582 (NO_2) cm^{-1}.

4 (N^1,N^1,N^2,N^2-tetramethylbenzene-1,2,4,5-tetramine): A suspension of **3** (1.02 g, 4 mmol) and 10% Pd/C (0.1 g) in methanol (80 mL) was stirred under a dihydrogen atmosphere at room temperature either overnight under 40 bar of pressure in a stainless-steel autoclave or for 3 days under 40 psi of pressure in a Parr shaker. The suspension was then filtered under inert atmosphere over a pad of Celite that was well rinsed with degassed methanol. Removing the solvent yielded a light-brown, air-sensitive solid. ^{1}H NMR (DMSO-d^6, 500 MHz): δ 3.34 (s, 12H), 4.07 (s, 4H), 6.20 (s, 2H).

5 (4,5-bis(dimethylamino)benzene-1,2-bis(3,5-di-*t*-butylsalicylidenimine)): After rinsing the Celite in the preceding synthesis (without isolating the product), the methanolic solution of **4** was directly added to a degassed solution of 3,5-di-*t*-butylsalicylaldehyde[48] (2.0 g, 8.5 mmol) and trimethylorthoformate (6.5 mL) in methanol (50 mL). After refluxing for 24 h under inert atmosphere, the suspension was cooled with an ice bath. The air-stable solid was filtered off and the excess trimethylorthoformate was removed by twice-repeated redissolution in a small amount of dichloromethane followed by evaporation to dryness in a rotary evaporator. The orange solid was then collected with cold methanol, filtered off, rinsed twice with cold methanol and dried under vacuum. Yield: 1.7 g, 67% over two steps. Anal. Calcd for $C_{40}H_{58}N_4O_2$ (626.9 g/mol): C 76.63, H 9.33, N 8.94. Found: C 76.59, H 9.43, N 8.79. ^{1}H NMR ($CDCl_3$, 500 MHz): δ 1.30 (s, 18H, *t*-Bu), 1.42 (s, 18H, *t*-Bu), 2.85 (s, 12H, NCH_3), 6.73 (s, 2H, central aromatic), 7.18 (d, 2H, 2.4 Hz, phenol), 7.38 (d, 2H, H_c, 2.4 Hz, phenol), 8.62 (s, 2H, imine), 13.80 (s, 2H, OH). ^{13}C NMR ($CDCl_3$, 125 MHz): δ 29.47, 31.51, 34.16, 35.10, 41.47, 109.34, 118.63, 126.39, 127.45, 135.84, 136.99, 140.04, 144.61, 158.36, 162.34. FT-IR (KBr): ν 1584, 1614 (C=N) cm^{-1}.

1: To a solution of **5** (313 mg, 0.5 mmol) in dichloromethane (5 mL), a methanolic solution (20 mL) of nickel(II) acetate tetrahydrate (88.4 mg, 0.5 mmol) was added dropwise. After 1h reflux, the suspension was cooled down. The precipitate was filtered off and rinsed copiously with methanol. Pure material was obtained as the red fraction upon short filtration over silica eluted by dichloromethane. The fraction was then concentrated to ca. 5 mL and layered with methanol to afford a red crystalline product. Yield 328 mg, 96%. Anal. Calcd for $C_{40}H_{56}N_4NiO_2$ (683.6 g/mol): C 70.28, H 8.26, N

8.20. Found: C 70.24, H 8.29, N 8.15. ^{1}H NMR ($CDCl_3$, 500 MHz): δ 1.29 (s, 18H, *t*-Bu), 1.45 (s, 18H, *t*-Bu), 2.86 (s, 12H, CH_3), 7.02 (s, 2H, central aromatic), 7.07 (d, 2H, 2 Hz, phenol), 7.35 (d, 2H, 2 Hz, phenol), 7.96 (s, 2H, imine). ^{13}C NMR ($CDCl_3$, 125 MHz): δ 29.73, 31.30, 33.92, 35.91, 41.49, 102.67, 119.66, 126.35, 129.75, 136.43, 136.80, 140.39, 144.79, 152.12, 163.79. FT-IR (KBr): ν 1501, 1526, 1605 (C=N) cm^{-1}. Needle-shaped single-crystals amenable for X-ray crystallography were grown by slow diffusion of a methanol layer atop a dichloromethane solution of **1**.

[**1H**](SbF_6): Atop a solution of **1** (50 mg, 0.073 mmol) in dichloromethane (5 mL) was carefully layered a solution of $HSbF_6 \cdot 6\ H_2O$ (48 mg, 0.146 mmol) in 15 mL methanol. The mixture was allowed to diffuse and evaporate slowly, yielding a deep-red crystalline solid that was washed with dichloromethane. Single-crystals were selected from this solid for X-ray diffraction studies.

Ac_2FcSbF_6 (diacetylferrocenium hexafluoroantimonate) was prepared in the glove box by stirring equimolar amounts of recrystallized diacetylferrocene (Ac_2Fc, 270.1 mg, 1.0 mmol) and $AgSbF_6$ (343.62 mg, 1.0 mmol) in diethyl ether (10 mL) for 20 minutes. The dark blue precipitate was filtered off over a small plug of Celite and was well rinsed with ether. The titled compound was then extracted off the plug by dichloromethane, yielding solutions of ca. 7 mM concentration. The titled compound can be isolated by rotary evaporation, but for purity reasons, we preferred the use of freshly prepared solutions. The exact concentration of these solutions was assessed by UV-vis titration experiments of **1**.

2.5 SUPPORTING INFORMATION

Supporting Information: Additional electrochemical, EPR, UV-vis-NIR and DFT data, together with crystallographic CIF files (CCDC-893505 and 893506). See Appendix B.

3. Redox Non-Innocence of the Bridge in Copper(II) Salophen and bis-Oxamato Complexes

3.0 Notes on the Chapter

In chapter 2, we showed that substituting the central aromatic ring of a salophen-nickel complex with dimethylamino groups directs the first two oxidation processes onto this aromatic bridge. A π-radical cation followed by an α-diiminoquinone were formed by two successive, easily accessible and reversible one-electron redox events. The redox activity of this modified salophen ligand can now be applied to complexes with other metals. One of particular interest for both bio-relevant and catalytic applications is copper(II). One foreseeable issue was that copper(II) is paramagnetic, i.e. it contains an unpaired electron. Paramagnetic species generate their own EPR signals and can couple magnetically to the radical formed during oxidation.

In this chapter, two ligands are compared: the modified salophen (TMTS) and a substituted phenylene(bis)oxamate (TMopba). The latter ligand is more electron-rich than TMTS and possesses only one aromatic moiety, thereby eliminating the possibility of oxidation at the phenolates and to limit the delocalization of the radical.

3.1 INTRODUCTION

The coordination chemistry of d-transition metal complexes with redox non-innocent ligands currently attracts considerable interest. A radical ligand not only imparts unique electronic properties to the complex, but also profoundly tunes its catalytic activity.[4,5,20,68–

[96] Many examples of cooperativity between a metal ion and an organic radical moiety during turnover exist in biology (galactose oxidase,[97–103] cytochrome P450,[19,104–106] ribonucleotide reductase[10]) and coordination chemistry.[20,23,24,107,108] The most prevalent biological radical cofactors are tyrosyl[97–103] and one-electron oxidized hemes. [19,104–106] Numbers of redox non-innocent ligands that can undergo one-electron transfers when engaged within a complex have been described by chemists. The most representative ones are porphyrins,[22] phenolates,[11,15,16,36,37,42–44,109–114] catecholates,[115–117] aminophenolates,[26,95,118–128] phenylene diamines,[27,129,130] α-dimine[69,88,131–135] and dithiolenes.[125,136] Generally, one-electron oxidation of a M^{n+}–L complex affords the high-valent $M^{(n+1)+}$–L species or the radical M^{n+}–$L^{\bullet}$ electromer, or an equilibrium of both (valence tautomerism). The electronics of the ligand, the size of the chelate ring as well as the nature of the metal ion are crucial factors that govern the oxidation site (scheme 3-1). This intricacy is illustrated by recent investigations on copper (Cu) salen complexes. Oxidation of the [Cu^{II}($Salcn^{tBu}$)] complex indeed affords a Cu(II) radical complex in thermal equilibrium with the Cu(III) phenolate species.[42,137] In contrast, single-electron oxidation of [Cu^{II}($Salcn^{OMe}$)][12] and [Cu^{II}(Sal-1,3-cn^{tBu})][138] affords the Cu(II) radical isomer, irrespective of the temperature.

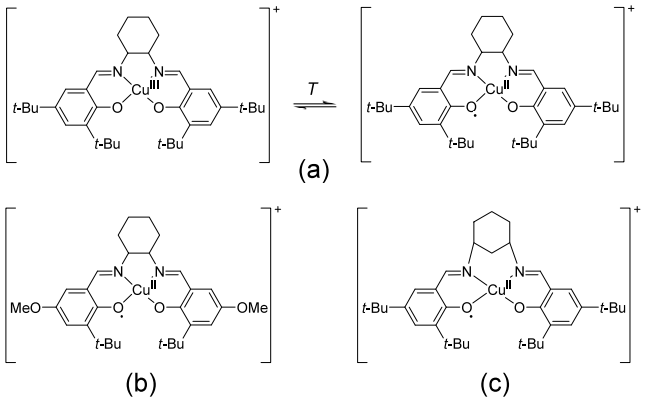

Scheme 3-1. Electronic structure of one-electron oxidized Cu(II) salen complexes: (a) $[Cu^{II}(Salcn^{tBu})]$; (b) $[Cu^{II}(Salcn^{OMe})]$; (c) $[Cu^{II}(Sal\text{-}1,3\text{-}cn^{tBu})]$.

In a previous paper we reported on the redox properties of the Ni(II)-salophen complex $[Ni(L^1)]$ (see scheme 3-2 for the ligand structure), whose bridging ring contains strongly electron-donating dimethylamino substituents.[139] We established by EPR spectroscopy that $[Ni(L^1)]$ undergoes two reversible one-electron transfers centered on the central diaminobenzene ring. Similarly, the Ni(II)-bis(oxamato) complex $[Ni^{II}(L^2)]^{2-}$ exhibits a ligand-centered oxidative redox activity, affording a Ni(II)-π radical complex.[30] This result was striking since both the Ni(II)[139] and Cu(II)[29] complexes of the related unsubstituted ligand undergo metal-centered redox activity. We herein describe the Cu(II) complexes $[Cu^{II}(\mathbf{L^1})]$ (**1**) and $[Cu^{II}(\mathbf{L^2})]^{2-}$ ($\mathbf{2^{2-}}$). By spectroelectrochemistry, EPR and DFT calculations we establish that one-electron oxidations of **1** and $\mathbf{2^{2-}}$ afford Cu(II) π-cation radical complexes. In addition, two-electron oxidation of **1** produces the Cu(II) complex $\mathbf{1^{2+}}$ in which the ligand adopts an iminoquinoid closed-shell form.

3.2 RESULTS AND DISCUSSION

3.2.1 Synthesis

The proligands $H_2\mathbf{L^1}$ and $Et_2H_2\mathbf{L^2}$ were synthesized according to published procedures.[30,139] Complex **1** was formed by reaction of $H_2\mathbf{L^1}$ with Cu(II) acetate, whereby coordination occurs upon deprotonation of the phenolate by the acetate ions. In the case of $Et_2H_2\mathbf{L^2}$, saponification with a strong base in water is required prior to slow addition of the Cu(II) salt. The doubly negatively charged complex is then isolated by ion metathesis as its PPh_4^+ salt, which confers $\mathbf{2}^{2-}$ great solubility in organic solvents such as CH_2Cl_2 or CH_3CN.

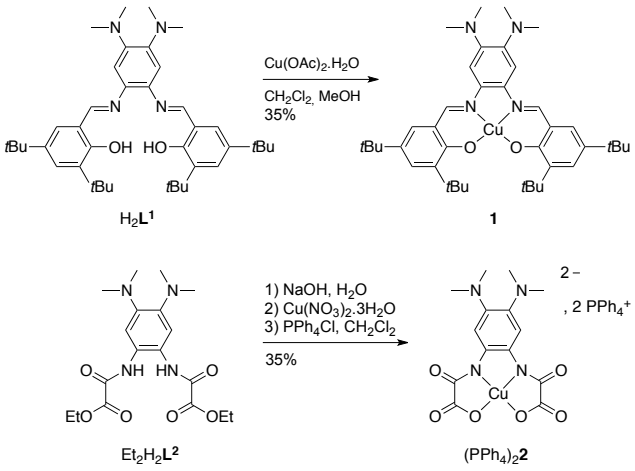

Scheme 3-2. Proligands ($H_2\mathbf{L^1}$, $Et_2H_2\mathbf{L^2}$) and Cu(II) complexes investigated in this work: $[Cu^{II}(\mathbf{L^1})]$ (**1**), $[Cu^{II}(\mathbf{L^2})]^{2-}$ ($\mathbf{2^{2-}}$ as a PPh_4^+ salt).

The proligands and complexes were characterized by X-ray crystallography (Figure 3-1, Table 3-1). **1** is isostructural to its Ni(II) analogue previously reported.[139] Both **1** and $\mathbf{2}^{2-}$ complexes exhibit a square-planar Cu(II) coordination geometry that is typical for salophen and bis(oxamate) environments.[29,137,140] Although the entire molecule of **1** is puckered, with a 30° angle between the mean phenolate planes, the angle between the

two N-Cu-O planes is only 5°. In $\mathbf{2}^{2-}$, this angle is less than 1°, but Cu-O bonds are longer due to the 5-5-5- chelate arrangement. The 6-5-6 chelate sequence in **1** provides a closer geometry to a strict square planar. In the two complexes, one methyl of each NMe_2 group is significantly out of planarity with the central aromatic ring ($C_{arom}C_{arom}NC_{Me}$ torsion angles between 61 and 70°). The steric clash between methyl groups thus enforces the nitrogen lone pair of the NMe_2 substituents to tilt out of the plane of the aromatic ring. The sum of the CNC angles about the NMe_2 substituents ranges from 337.8° to 343.2°, indicating intermediate hybridizations between sp^2 and sp^3. Resonance with the NMe_2 groups is thus limited.

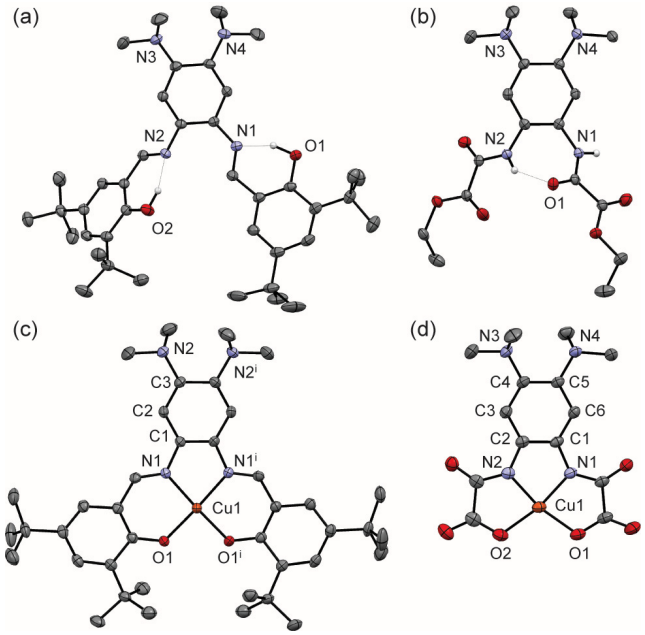

Figure 3-1. ORTEP representation at 50% ellipsoid probability of the proligands and complexes, with selected bond lengths (Å). H atoms are omitted for clarity, except those engaged in hydrogen bonding. (a) $H_2\mathbf{L^1}$; (b) one molecule in $Et_2H_2\mathbf{L^2}$; (c) **1** (^{i}: *x*, *y*, 0.5-*z*): Cu1-O1: 1.8922(16), Cu1-N1: 1.9349(19); (d) the anion in $(PPh_4)_2\mathbf{2}$: Cu1-O1: 1.9490(14), Cu1-O2: 1.9609(14), Cu1-N1: 1.9122(16), Cu1-N2: 1.8958(16).

Table 3-1. Crystallographic Data for $H_2\mathbf{L^1}$, $Et_2H_2\mathbf{L^2}$, **1** and $(PPh_4)\mathbf{2}$.

	$H_2\mathbf{L^1}$	$Et_2H_2\mathbf{L^2}$	1	$(PPh_4)_2\mathbf{2}$
CCDC number	986938	986939	986940	986941
Empirical formula	$C_{40}H_{58}N_4O_2$	$C_{36}H_{52}N_8O_{12}$	$C_{40}H_{56}CuN_4O_2$	$C_{62}H_{54}CuN_4O_6P_2$
Formula weight	626.90	788.85	688.43	1076.57
Temperature	150(2) K	150(2) K	200 K	149(2) K
Wavelength	0.71073 Å	0.71073 Å	0.71073 Å	0.71073 Å
Crystal system	Monoclinic	Triclinic	Monoclinic	Monoclinic
Space group	$P2_1/n$	P-1	C2/c	$P2_1/n$
a	12.0460(8) Å	11.0946(8) Å	24.250(5) Å	14.0795(11) Å
b	17.8754(12) Å	12.5522(9) Å	15.236(3) Å	25.948(2) Å
c	17.7441(12) Å	16.3727(12) Å	10.361(2) Å	14.5253(11) Å
α	90°	78.1050(10)°	90°	90°
β	102.6350(10)°	70.6440(10)°	101.68(3)°	101.1600(10)°
γ	90°	66.7530(10)°	90°	90°
Volume	3728.3(4) $Å^3$	1969.1(2) $Å^3$	3749.0(13) $Å^3$	5206.2(7) $Å^3$
Z	4	2	4	4
Density (calculated)	1.117 g cm^{-3}	1.330 g cm^{-3}	1.220 g cm^{-3}	1.373 g cm^{-3}
Absorption coefficient	1.069	0.101	0.621	0.539
F(000)	1368	840	1476	2244
Crystal size	0.288 × 0.229 × 0.210 mm	0.726 × 0.354 × 0.268 mm	0.04 × 0.04 × 0.26 mm	0.449 × 0.362 × 0.248 mm
Index ranges	$h = -15 \rightarrow 15$, $k = -22 \rightarrow 2$, $l = -22 \rightarrow 22$	$h = -14 \rightarrow 14$, $k = -16 \rightarrow 16$, $l = -21 \rightarrow 21$	$h = -28 \rightarrow 28$, $k = -18 \rightarrow 18$, $l = -12 \rightarrow 12$	$h = -19 \rightarrow 18$, $k = -34 \rightarrow 35$, $l = -18 \rightarrow 19$
Reflections collected	43087	23453	19006	62464
Independent reflections	8292	9031	3299	12834
Parameters	437	533	221	680
Goodness of fit	1.005	1.031	1.113	1.018
Final R indices [$I > 2\sigma(I)$]	$R_1 = 4.98\%$, $wR_2 = 10.65\%$	$R_1 = 3.87\%$, $wR_2 = 9.47\%$	$R_1 = 3.96\%$, $wR_2 = 8.34\%$	$R_1 = 3.87\%$, $wR_2 = 8.63\%$
R indices (all data)	$R_1 = 9.51\%$, $wR_2 = 12.72\%$	$R_1 = 4.82\%$, $wR_2 = 10.08\%$	$R_1 = 6.48\%$, $wR_2 = 9.01\%$	$R_1 = 6.34\%$, $wR_2 = 9.66\%$
Largest diff. peak and hole	0.181 and -0.218 e $Å^{-3}$	0.322 and -0.293 e $Å^{-3}$	0.308 and -0.250 e $Å^{-3}$	0.363 and -0.489 e $Å^{-3}$

3.2.2 Oxidation of $H_2\mathbf{L^1}$ and $Et_2H_2\mathbf{L^2}$

The electrochemical behavior of the proligands $H_2\mathbf{L^1}$ and $Et_2H_2\mathbf{L^2}$ was studied in CH_2Cl_2 (+ 0.1 M nBu$_4$NClO$_4$ as supporting electrolyte). The cyclovoltammogram (CV) of $H_2\mathbf{L^1}$ displays two oxidation waves at $E_{1/2}^1 = 0.07$ V ($\Delta E_p = 0.06$ V) and $E_{1/2}^2 = 0.25$ V vs. the Fc^+/Fc couple (Figure 3-2a). While the first redox transfer is reversible, the low I_p^a/I_p^c value for the second wave indicates that the dication is poorly stable. The $E_{1/2}^1$ and $E_{1/2}^2$ values are within the range of those measured for the oxidation of a series of

poly(dimethylamino) aromatic derivatives,[39–41] suggesting sequential oxidations of the central tetraaminobenzene ring into a radical cation and then a closed-shell α-diiminoquinone dication. Coulometric measurements at a fixed potential of 0.1 V establish that the first redox wave corresponds to a one-electron transfer and that the cation $(H_2\mathbf{L^1})^+$ is stable at the time scale of the electrolysis (30 min at 233 K). This was not the case for the dication, which decomposes significantly during electrolysis. The CV of $Et_2H_2\mathbf{L^2}$ exhibits an anodic peak at 0.24 V, which is associated to a cathodic one at -0.07 V (Figure 3-2b). The large ΔE_p value (0.31 V) is clear-cut evidence that a chemical reaction is coupled to the electron transfer (ECE mechanism). The anodic potential is 0.15 V higher than $E_{1/2}^1$ of $H_2\mathbf{L^1}$, showing that the H-bonded amide groups exert a stronger electron-withdrawing effect than the H-bonded imines.[141] As for $H_2\mathbf{L^1}$ coulometric titration reveals that the oxidation wave corresponds to a one-electron transfer and that the stability of the oxidized species is noteworthy.

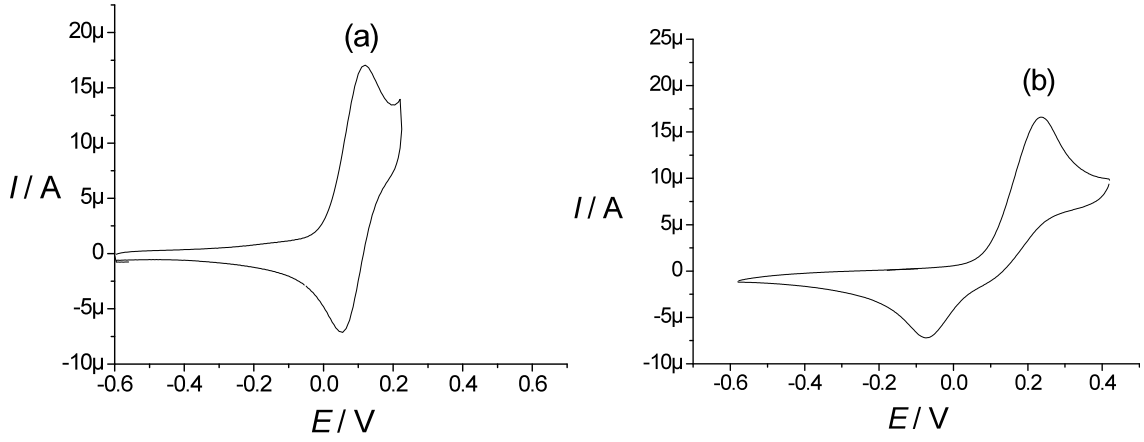

Figure 3-2. Cyclovoltammogram of 1 mM CH_2Cl_2 solutions (+ 0.1 M nBu$_4$NClO$_4$) of proligands $H_2\mathbf{L^1}$ (a) and $Et_2H_2\mathbf{L^2}$ (b). Potentials are relative to the Fc^+/Fc redox couple. Scan rates: 0.1 V / s, T = 298 K.

Table 3-2. Redox Potentials [a]

	$E_{1/2}^1$	$E_{1/2}^2$	$E_{1/2}^3$	$E_{1/2}^4$
$H_2\mathbf{L^1}$	0.07 (60)	0.25 [b]		
$Et_2H_2\mathbf{L^2}$	0.24, -0.07 [c]			
1 [d]	0.09 (60)	0.22 (60)	0.82 (80)	0.96 [b]
$Ni\mathbf{L^1}$ [16]	0.12	0.24	0.97	
$\mathbf{1}H^+$	0.62, 0.28 [c]			
$\mathbf{2}^{2-}$	-0.47 (80)	-0.17 [e]		
$(Ni\mathbf{L^2})^{2-}$ [17]	-0.51			

[a] In V vs. the Fc^+/Fc couple. Conditions: 1.0 mM sample in CH_2Cl_2 + 0.1 M n-Bu_4NClO_4, T = 293 K. The peak-to-peak separations ΔE_p given in mV in parentheses. [b] Irreversible process: E_p^a is given. [c] ECE process: E_p^a and E_p^c are given. [d] In n-Bu_4NPF_6 the oxidation potentials are 0.14 V (90), 0.31 V (110), 0.94 V (100), 1.13 V (100). [e] The profile and intensity of the cathodic wave suggests adsorption of **2** on the electrode; E_p^a is given.

The ligand cations $(H_2\mathbf{L^1})^+$ and $(Et_2H_2\mathbf{L^2})^+$ were prepared by exhaustive electrolysis and characterized by UV-vis and EPR spectroscopies. The UV-vis spectrum of $(H_2\mathbf{L^1})^+$ in CH_2Cl_2 (+ 0.1 M n-Bu_4NClO_4) contrasts sharply with that of its neutral counterpart (Figure 3-3a). While $H_2\mathbf{L^1}$ does not display absorption bands above 500 nm, several transitions could be detected in the visible region in the case of $(H_2\mathbf{L^1})^+$, mainly as shoulders at ca. 440 nm, 520 nm and 680 nm. Similarly, the UV-vis spectrum of $(Et_2H_2\mathbf{L^2})^+$ displays a low energy band at 580 nm that is absent in the spectrum of the neutral precursor, in addition to the 380 nm absorption (Figure 3-3b). Similar transitions were reported for free radicals of the Würster's type by Granick et al.[142] Thus, the oxidation site in $(H_2\mathbf{L^1})^+$ and $(Et_2H_2\mathbf{L^2})^+$ is the bridging *bis*(dimethylamino)benzene ring. The shift in absorption band on going from $(H_2\mathbf{L^1})^+$ to $(Et_2H_2\mathbf{L^2})^+$ is ascribed to changes in the electron-donating ability of imine versus amide groups and the extend of π system in $(H_2\mathbf{L^1})^+$.

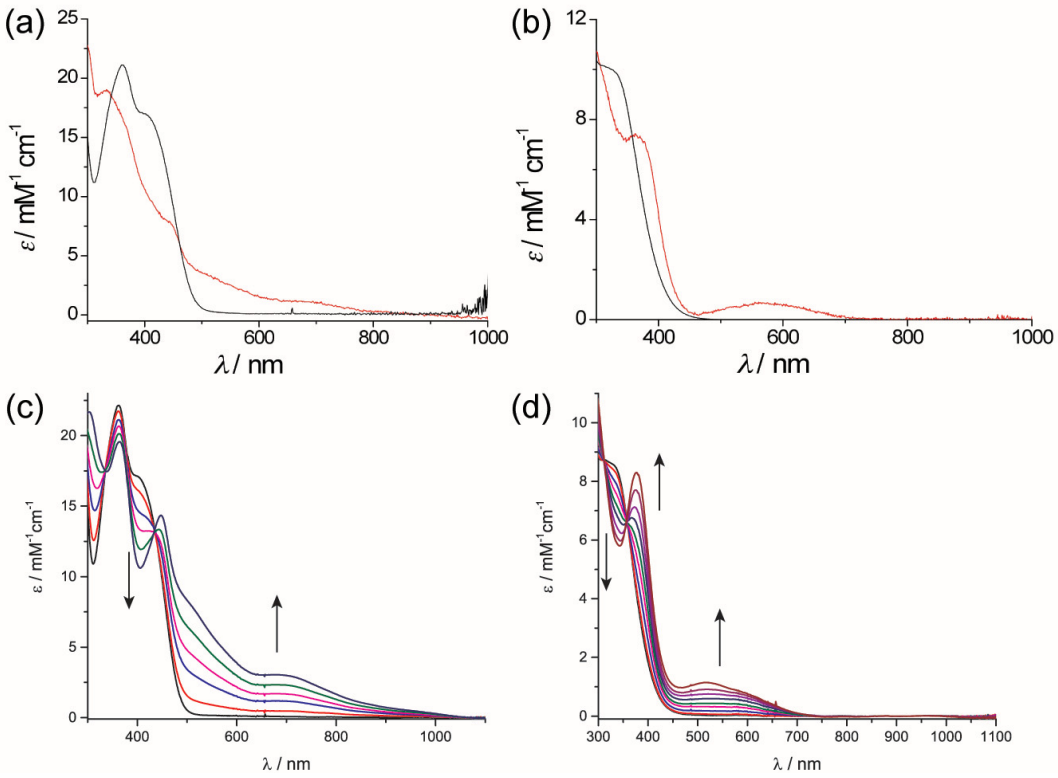

Figure 3-3. UV-vis spectra of proligands and their oxidation products generated by electrolysis at -30°C (0.1 mM in CH_2Cl_2, 0.1 M nBu$_4$PF$_6$, T = 233 K, l = 1.000 cm): (a) $H_2\mathbf{L^1}$ (black) and $(H_2\mathbf{L^1})^+$ (red), (b) $Et_2H_2\mathbf{L^2}$ (black) and $(Et_2H_2\mathbf{L^2})^+$ (red). Titration of: (c) $H_2\mathbf{L^1}$ and (d) $Et_2H_2\mathbf{L^2}$ with 0-1.0 equivalents of acetylferrocenium triflate in CH_2Cl_2. T = 243 K, l = 1.000 cm.

The radical nature of the cations was confirmed by EPR spectroscopy. The isotropic X-band EPR spectra of $(H_2\mathbf{L^1})^+$and $(Et_2H_2\mathbf{L^2})^+$ in CH_2Cl_2 both display a signal centered at g = 2.003 with a well-resolved hyperfine splitting (Figure 3-4). The hyperfine splitting arises from the interaction of the electron spin with H and N atoms. The spectra are not superimposable, showing that the salicyl/amide substituents affect the spin distribution. The experimental spectrum of $(H_2\mathbf{L^1})^+$ could be simulated by using the spin Hamiltonian parameters A_N = 12.8 MHz (2 equivalent ^{14}N) and A_H = 17.8 MHz (for 12 equivalent ^{1}H). Simulation of the spectrum of $(Et_2H_2\mathbf{L^2})^+$ gives the following values: A_N = 15.4 MHz (2 equivalent ^{14}N) and A_H = 19.6 MHz (for 12 equivalent ^{1}H). These hyperfine coupling

(hfc) constants are consistent with an unpaired electron essentially shared between the two dimethylamino substituents. Interestingly, the hfc constants of $(H_2\mathbf{L^1})^+$ are slightly different than those reported for $[Ni(\mathbf{L^1})]^+$,[139] highlighting the influence of coordination on the spin density in the π-radical. Further, the hfc constants obtained for $(Et_2H_2\mathbf{L^2})^+$ are larger than those measured for $(H_2\mathbf{L^1})^+$. Thus a higher amount of spin density resides on the dimethylamino substituents in $(Et_2H_2\mathbf{L^2})^+$. Taft et al. established empirical relationships between the hfc constants of the nitrogen and hydrogen atoms and the σ+ Hammet of the substituent in para-substituted N,N-dimethylaniline cation radicals.[143] An increase in the σ+ (i.e. more electron-withdrawing group that makes the compound harder to oxidize) results in higher hfc constants. Such correlation applies here, with the harder to oxidize $(Et_2H_2\mathbf{L^2})^+$ exhibiting larger hfc constants than $(H_2\mathbf{L^1})^+$.

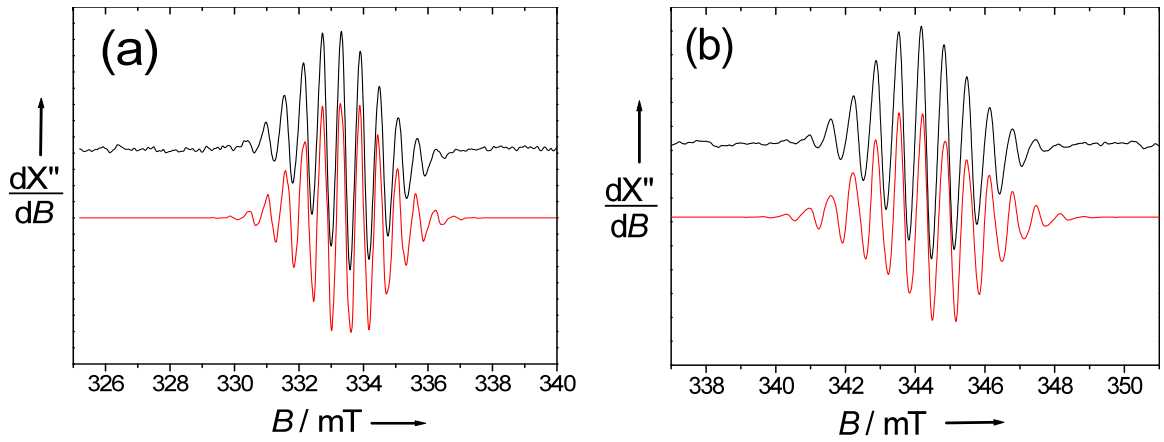

Figure 3-4. Isotropic solution X-Band EPR spectrum of: (a) $(H_2\mathbf{L^1})^+$ and (b) $(Et_2H_2\mathbf{L^2})^+$ generated by electrolysis at -30°C (1 mM in CH_2Cl_2, 0.1 M nBu$_4$PF$_6$), T = 298 K. Conditions: (a) Microwave Freq. 9.33 GHz, power: 8 mW, Mod Freq. 100 kHz, Amp. 0.1 mT; (b) Microwave Freq. 9.62 GHz, power: 8 mW, Mod Freq. 100 kHz, Amp. 0.3 mT.

DFT calculations were undertaken using the ORCA program package in order to get insight onto the geometric and electronic structures of proligands $\mathbf{H_2L^1}$ and $Et_2H_2\mathbf{L^2}$ (and the complexes, see section 3.2.7).

The structural rearrangements induced by oxidation of $H_2\mathbf{L^1}$ into $(H_2\mathbf{L^1})^+$ and $Et_2H_2\mathbf{L^2}$ into $(Et_2H_2\mathbf{L^2})^+$ were investigated by DFT calculations (Scheme 3-3, Figures C-1 to C-4, Table C-1 and C-2). For $H_2\mathbf{L^1}$, the phenolate C–O bonds remain essentially unaffected and no quinoidal pattern typical of phenoxyl radicals is observed in the peripheral rings. For both species, the bond lengths that change most significantly upon oxidation occur within the bridging ring, notably with a 0.019-0.034 Å elongation of the (N)C–C(N) bonds while the other C–C bonds vary within -0.017 to +0.015 Å. In addition, the shortening of the $C–N_{dimethylamino}$ bonds is much more important than that of the $C–N_{imine}$ or $C–N_{amide}$ bonds. These DFT-optimized structures are consistent with the unpaired electron residing mainly on the bis(dimethylamino) side of the bridge, in agreement with EPR data.

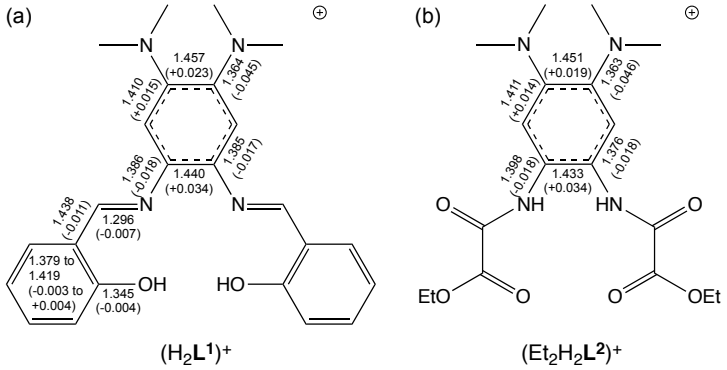

$(H_2\mathbf{L^1})^+$ $(Et_2H_2\mathbf{L^2})^+$

Scheme 3-3. Selected calculated bond lengths in $(H_2\mathbf{L^1})^+$ (a) and $(Et_2H_2\mathbf{L^2})^+$ (b), together with the variations upon oxidation from the neutral to the monocationic states (in parentheses). *tert*-Butyl substituents in (a) were omitted for clarity. All species were left-right symmetric (± 0.001 Å). See Tables C-1 and C-2 for details.

Electronic structure calculations on oxidized proligands $(H_2\mathbf{L}^1)^+$ and $(Et_2H_2\mathbf{L}^2)^+$ provide spin density plots and localized Singly Occupied Molecular Orbitals (SOMO) that support an oxidation occurring on the central ring (Figure 3-5). For both species, Mulliken population analysis indicate that the spin density is spread over the tetraminobenzene ring, with positive spin populations at the dimethylamino nitrogens, the N-adjacent aromatic carbons while those on the imine/amide nitrogens or phenols are negligible. Correspondingly, the SOMOs of $(H_2\mathbf{L}^1)^+$ and $(Et_2H_2\mathbf{L}^2)^+$ are almost exclusively distributed over the central benzene ring.

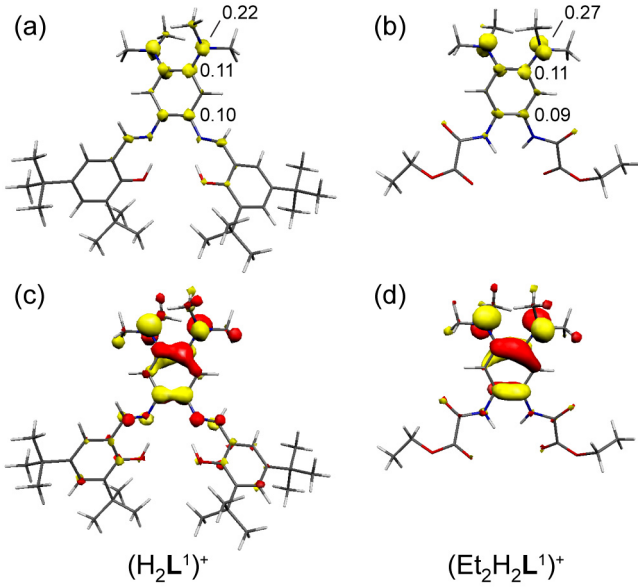

Figure 3-5. (a, b) Spin density plots, including the values of the most important individual spin populations, and (c, d) localized SOMOs for $(H_2\mathbf{L}^1)^+$ (left) and $(Et_2H_2\mathbf{L}^2)^+$ (right).

Last, EPR parameters of oxidized proligands $(H_2\mathbf{L}^1)^+$ and $(Et_2H_2\mathbf{L}^2)^+$ were calculated (Table C-3). Both sets of *g*-tensors confirm the radical nature of the species with predicted isotropic values close to that of the free electron (2.0032 and 2.0034, respectively). An excellent agreement is also found between the experimental and

calculated hfc constants for the ^{14}N and ^{1}H centers of the dimethylamino substituents, which is consistent with the spin density being mainly distributed over these groups.

3.2.3 Spectroscopic properties of 1, 1H$^+$ and 2^{2-}

The UV-vis spectrum of **1** in CH_2Cl_2 displays a main absorption band at 439 nm (3,510 M^{-1} cm^{-1}) that is assigned to a charge-transfer (CT) transition. As expected, this band slightly blue-shifted compared with that in the isostructural Ni complex.[139] A low-intensity shoulder could be additionally detected at around 600 nm, which is assigned to Cu(II) d-d transition. The UV-vis spectrum of **2**$^{2-}$ consists of an intense CT band at 353 nm (14,800 M^{-1} cm^{-1}). Precise assignments of these bands are performed in section 3.2.7 by TD-DFT methods.

1H$^+$ was prepared by adding one molar equivalent of $HClO_4$ to a CH_2Cl_2 solution of **1** and stirring for 3 h. Upon protonation, the initially intense red-brown solution of **1** turns pale. The loss of intensity in the CT band is consistent with protonation of the dimethylaminobenzene ring of **1**.[139] In the case of **2**$^{2-}$, the protonated mixture was not analyzed due to decomposition and precipitation of the mixture.

Frozen-solution EPR spectra of **1**, **1**H$^+$ and **2**$^{2-}$ (Figure 3-6a,b,d) reveal axial $S = ½$ spin states that are typical for square-planar Cu(II) complexes. The EPR spectra were simulated with the spin Hamiltonian parameters given in Table 3-3. The g_3/A_3 ratio can be used to estimate the extent of geometric distortion about the metal center.[144,145] For **1**, **1**H$^+$ and **2**$^{2-}$, this ratio is between 101 and 106 cm, fully consistent with a square-planar geometry of the Cu ion.[146] The g_3 value is smaller for **1H**$^+$ than for **1**, reflecting a decreased ligand field in the former complex. This behavior is a direct consequence of

the protonation of one dimethylamino substituent, making the benzenebis(imine) moiety a weaker donor. The EPR spectrum of $\mathbf{2}^{2-}$ in frozen CH_2Cl_2 is typical for a square-planar Cu(II) ion coordinated by strong amidato donors. The super hyperfine coupling constants with four equivalent nitrogen atoms are well resolved both in the parallel and perpendicular region of the spectrum, as customary with Cu-amidato complexes. The g_3 value (2.167) is the smallest of the series, consistent with a tetraanionic donor set of the ligand.

DFT calculations were conducted to predict the EPR parameters of the parent complexes **1** and $\mathbf{2}^{-}$ and the dioxidized species $\mathbf{1}^{2+}$ (Table 3-3, see section 3.2.7 below for more computational details). The computed *g* and *A* tensors for the three species indicate an axial signal characterized by an average g_{iso} value of 2.077 and an average ^{63}Cu A_{iso} value of 10.7 mT. These values are typical for square-planar Cu(II) complexes, and are close to those derived from EPR simulations, in support of the experimental findings regarding the chemical nature of these complexes.

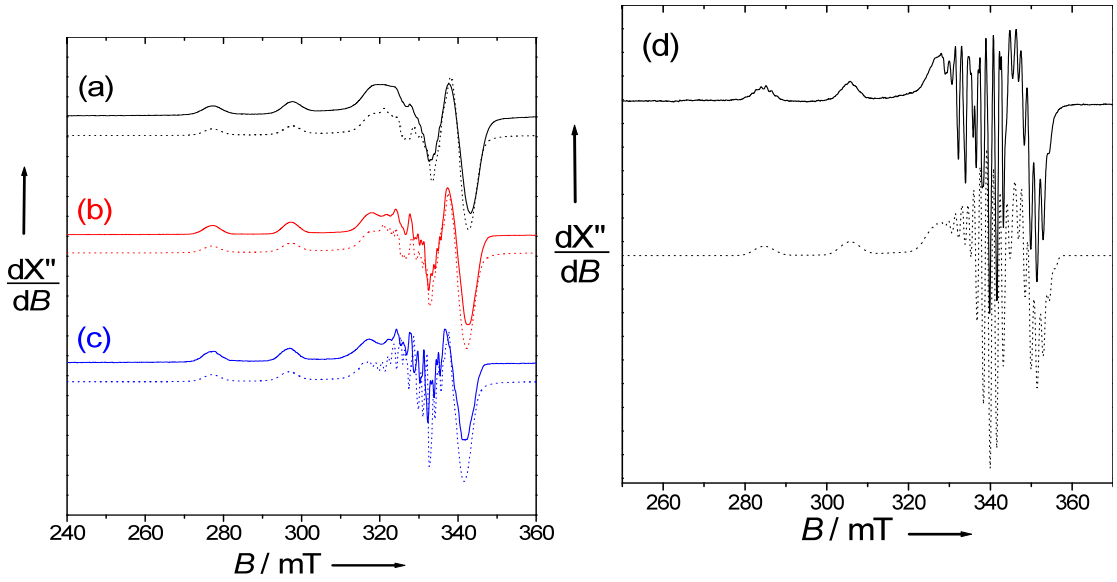

Figure 3-6. X-band EPR spectra of: **1** (a, black), **1H**$^{+}$ (b, red), **1**$^{2+}$ (c, blue) and **2**$^{2-}$ (d) in1 mM CH_2Cl_2 frozen solution (+0.1 M nBu$_4$PF$_6$). Microwave Freq. 9.45 GHz power: 5 mW, Mod. Freq. 100 kHz, Amp: 0.3 mT. T = 100 K. Solid lines: experimental spectra, dotted lines: simulations using the parameters given in the text.

Table 3-3. Experimental and Calculated Spin Hamiltonian Parameters of the Cu(II) Complexes.

		Experimental			Calculated	
	S	g_1, g_2, g_3	A_1, A_2, A_3 (mT) [a]		g_1, g_2, g_3	A_1, A_2, A_3 (mT) [a]
1	½	2.042, 2.042, 2.197	3.8, 3.8, 20.3 [b]		2.0420, 2.0435, 2.1475	3.8, 3.8, 25.2
1H^{+}	½	2.045, 2.045, 2.200	3.6, 3.6, 20.2 [b]		-	-
1^{2+}	½	2.042, 2.042, 2.205	2.5, 2.5, 19.7 [b]		2.0428, 2.0439, 2.1447	2.8, 2.9, 24.9
2^{2-}	½	2.040, 2.040, 2.167	1.5, 1.5, 21.1 [b]		2.0435, 2.0440, 2.1414	4.2, 4.2, 24.7
		Experimental			Calculated	
		g_{iso}	D (cm^{-1}) [a]	E/D	D (cm^{-1})	E/D
1^{+}	1	g_{iso} = 2.02	0.040	0	0.024	0.27
2^{-}	1	silent	n/a	n/a	0.84	0.14

[a] Absolute value. [b] Superhyperfine coupling constants were measured on the triple-derivative spectra: A_{2H} = 0.73, A_{2N} = 1.54 for **1** and **1H**$^{+}$; A_{2H} = 0.56, A_{2N} = 1.54 mT for **1**$^{2+}$; A_{2N} = 1.3 mT for **2**$^{2-}$, respectively.

3.2.4 Electrochemistry of 1 and 2^{2-}

The CV of **1** in CH_2Cl_2 (+ 0.1 M nBu$_4$NClO$_4$, Figure 3-6a, Table 3-2) displays four quasi-reversible one-electron oxidation waves at 0.14, 0.31, 0.94 and 1.13 V vs. Fc^{+}/Fc. The first two oxidation potentials match fairly well those measured for the Ni(II)

analogue of **1**, Ni$\mathbf{L}^{\mathbf{1}}$ (Table 3-2).[139] Thus, the first two oxidation waves of **1** are assigned to redox processes centered on the tetraaminobenzene ring, yielding successively the π-cation radical and the iminoquinone dication. The highest oxidation waves may correspond to the successive oxidations of the phenolate moieties into phenoxyl radicals.[12,42,69,88,125,131–137,147] However, due the high potential values it is not possible to unambiguously conclude regarding these two waves.

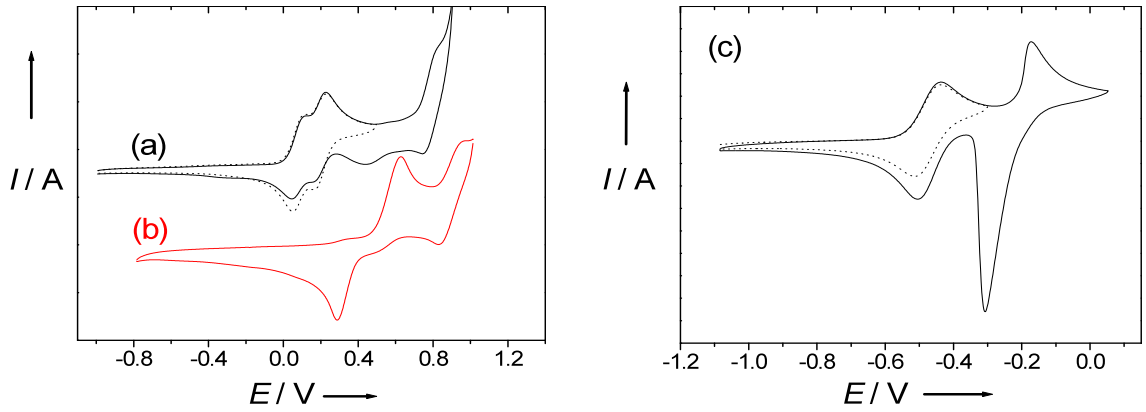

Figure 3-7. Cyclovoltammograms of 1.0 mM CH_2Cl_2 solutions (+0.1 M nBu$_4$NClO$_4$) of (a) **1**, (b) $\mathbf{1H^+}$ and (c) $\mathbf{2}^{2-}$. Potentials are referenced to the Fc^+/Fc redox couple. Scan rates: 100 mV/s, T = 298 K.

Upon protonation, the redox waves of **1** disappeared in the CV while a redox process characteristic of $\mathbf{1H^+}$ emerged, with an oxidation wave at 0.62 V coupled to a cathodic wave at 0.28 V (Figure 3-6b). The large ΔE_p (340 mV) is evidence that the electron-transfer is coupled to a chemical reaction, which, by analogy to (Ni$\mathbf{L}^{\mathbf{1}}$H)$^+$ (Table 3-2), is a fast deprotonation, affording $\mathbf{1}^{2+}$.[139] This hypothesis is supported by the similarity between $E_c^{\,1}$ of $\mathbf{1}$H$^+$ and $E_{1/2}^{\,2}$ of **1**, as well the analogy between $E_{1/2}^{\,2}$ of $\mathbf{1}$H$^+$ and $E_{1/2}^{\,3}$ of **1**. Notably, the first oxidation wave is anodically shifted by more than 300 mV in the

presence of protons, consistent with the fact that the protonation site is a basic dimethylamino group.

The CV of $\mathbf{2}^{2-}$ displays a reversible redox wave at $E_{1/2}^{1}$ = -0.42 V followed by an irreversible anodic signal at $E_p^{a,2}$ = -0.10 V (Figure 3-6c). The latter is associated to a cathodic signal at -0.26 V, whose profile and high intensity suggest reduction of **2** adsorbed on the electrode. Thus, while the mono-oxidized species $\mathbf{2}^{-}$ could be generated in solution, we were unable to isolate the dioxidized complex. As expected, the first two oxidations of $\mathbf{2}^{2-}$ occur at much lower potential than for **1** as the result of the greater donor ability of the deprotonated amidato nitrogen atoms compared to that of the neutral imine ones.

3.2.5 Electronic spectra of the oxidized species

The oxidized species $\mathbf{1}^{+}$ and $\mathbf{1}^{2+}$ were generated by bulk electrolysis at 233 K for spectroscopic characterization. In contrast to **1**, the electronic spectra of $\mathbf{1}^{+}$ and $\mathbf{1}^{2+}$ display strong absorption bands above 450 nm (Figure 3-8, Table 3-4) that may correspond to Cu(II)-radical/diiminoquinone species, or alternatively to Cu(III)/Cu(III)-radical complexes.[137] The spectrum of $\mathbf{1}^{+}$ displays transitions at 446, 508 and 974 nm. It is closely related to that of the Ni analogue of $\mathbf{1}^{+}$, $(\mathrm{Ni}\mathbf{L}^{1})^{+}$,[139] supporting the description of $\mathbf{1}^{+}$ as a Cu(II)-(π radical) complex. The assignment of the bands is intra-ligand charge-transfer (ILCT) involving the bridging radical moiety (see section 3.2.7). The visible-NIR spectrum of $\mathbf{1}^{2+}$ displays transitions at 330 nm, 486 nm and 778 nm that we assign to both IL and MLCT involving the diiminoquinone moiety and the Cu ion. Oxidation of $\mathbf{1H}^{+}$

produces a Vis-NIR spectrum that is very similar to that of $\mathbf{1}^{2+}$, confirming that oxidation is accompanied by deprotonation.[139]

The spectrum of $\mathbf{2}^{-}$ shows intense transitions at 628 and 405 nm with a shoulder at *ca*. 450 nm. These bands are remarkably similar, though red-shifted, to those reported for the Ni analogue of $\mathbf{2}^{-}$ for which EPR spectroscopy indicated a Ni(II)-(π radical) formulation.[30] A Cu(III)-oxamato complex has been previously described with the unsubstituted analogue of $\mathbf{2}^{-}$.[140] Its visible spectrum showed transitions up to 580 nm, with somewhat much smaller intensity. This argues against the assignment of $\mathbf{2}^{-}$, as a Cu(III) complex and reinforces the idea that it has a Cu(II)-(π radical) character.

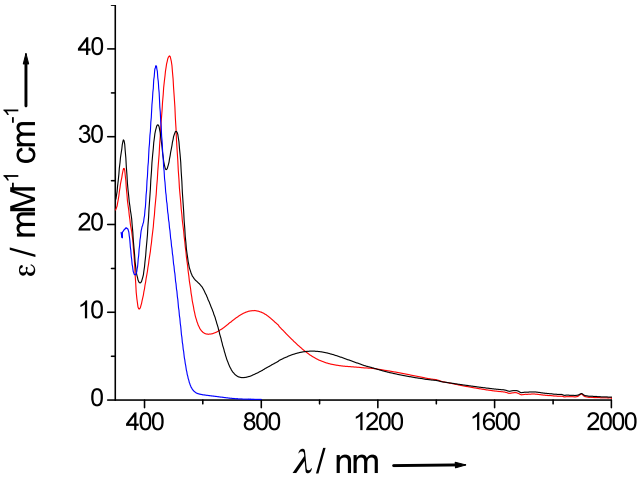

Figure 3-8. UV-vis spectra of **1** (blue) $\mathbf{1}^{+}$ (black) and $\mathbf{1}^{2+}$ (red) generated by electrolysis at 233 K (CH_2Cl_2, 0.1 M nBu$_4$PF$_6$). T = 298 K.

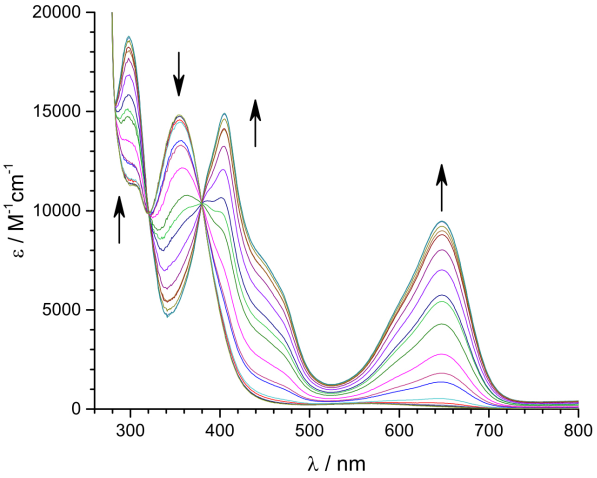

Figure 3-9. UV-vis spectral evolution during the fixed-potential electrolysis of $\mathbf{2}^{2-}$ to form $\mathbf{2}^{-}$ (CH_2Cl_2, 0.1 M nBu$_4$NPF$_6$, T = 233 K).

Table 3-4. Electronic Transitions of $\mathbf{1}^{0/+/2+}$ and $\mathbf{2}^{2-/-}$.

	Experimental λ, nm (ε, mM^{-1} cm^{-1})	TD-DFT λ, nm (f)	Assignment [a]
1	514 (sh)	554 (0.229)	LMCT
	439 (3.5)	460 (0.528)	LLCT
$\mathbf{1}^{+}$	972 (5.6)	980 (0.132)	ILCT
	508 (30.6)	522 (0.606)	MLCT
	446 (31.4)	422 (0.615)	LLCT
	328 (29.7)	326 (0.444)	LLCT
$\mathbf{1}^{2+}$	778 (10.2)	737 (0.271)	LMCT
	486 (39.2)	518 (0.738)	ILCT
	330 (26.4)	370 (0.182)	LLCT
$\mathbf{2}^{2-}$	561 (0.2)	538 (0.028)	LMCT
	353 (14.8)	360 (0.220)	LLCT
$\mathbf{2}^{-}$	628 (9.5)	645 (0.207)	ILCT
	405 (15.0)	455 (0.258)	LLCT

[a] See section 3.2.7 for more details. CT: charge-transfer, LM: ligand-to-metal, ML: metal-to-ligand, IL: intraligand (two different moieties of the ligand), LL ligand-to-ligand (same moiety).

3.2.6 EPR spectra of the oxidized species

The 10 K EPR spectrum of the electrochemically generated $\mathbf{1}^{+}$ in CH_2Cl_2 (+ 0.1 M nBu$_4$NPF$_6$) is depicted in Figure 3.10. It exhibits a broad signal at $g \approx 2$ that is assigned to $\mathbf{1}^{+}$, which superimposes to a (S = ½) signal corresponding to **1** present as impurity in the

sample. The presence of a half-field signal (g = 4.3) demonstrates that the ground spin state of **1**$^{+}$ is a triplet (S = 1), which can only result from ferromagnetic coupling between Cu(II) and radical spins given the low temperature. This assumption is confirmed by the observation of a 4-line pattern in the half field transition, arising from hyperfine interaction of the electronic spin with one Cu(II) nuclear spin. Thus, the present data unequivocally rule out the formulation of **1**$^{+}$ as a Cu(III) complex, which would be diamagnetic. The triplet signal could be simulated by using the zero-field splitting (ZFS) parameters $|D|$ = 0.04 cm^{-1}, E/D = 0 (axial signal) and an isotropic g value of 2.02. Interestingly, the ZFS parameters reported for Cu(II)-phenoxyl radical salen complexes are usually close to or larger than the X-Band quantum (0.3 cm^{-1}), due to the short interspin distance. In **1**$^{+}$, the unpaired electron is mainly hosted by the dimethylamino substituents and neighboring carbons atoms, and thus far from the metal center. The ZFS parameters are consequently much smaller, making the triplet detectable at the X-band frequency. Noteworthy, the qualitative point-dipole approximation leads to a spin-spin separation of ca. 4.1 Å. This distance is smaller than the Cu···$N_{dimethylamino}$ distance (6.5 Å), attesting that the unpaired electrons are somewhat delocalized. Also noticeable is the difference of ZFS parameters between **1**$^{+}$ and its dimethoxy derivative (where MeO substituents replace the NMe_2 ones).[148] Due to the weaker electron-donating ability of MeO substituents, the central-ring orbitals involved in the ZFS are developed closer to the metal, thus conducing a higher $|D|$ value in the MeO derivative.

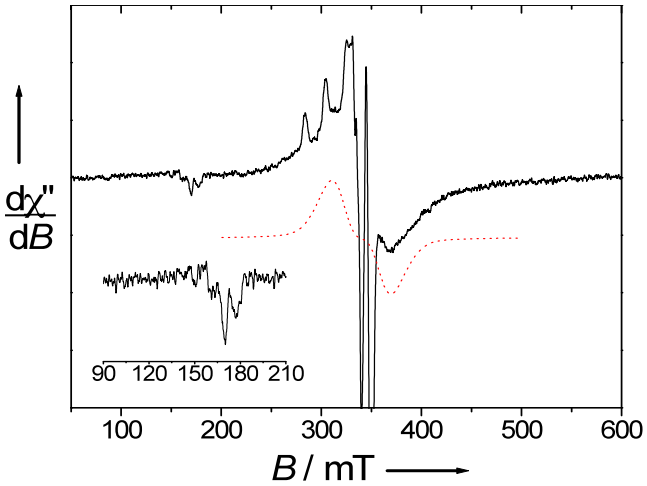

Figure 3-10. X-band EPR spectrum of $\mathbf{1}^{+}$ generated by electrolysis at -30°C (1 mM in CH_2Cl_2, 0.1 M nBu$_4$PF$_6$). Microwave Freq. 9.45 GHz power: 5 mW, Mod. Freq. 100 KHz, Amp: 0.3 mT. T = 10 K. Solid lines: experimental spectra, red dotted lines: simulations using the parameters given in the text. Inset: zoom of the $\Delta M_S = 2$ region.

The 10 K EPR spectrum of the electrogenerated $\mathbf{1}^{2+}$ contrasts sharply with that of $\mathbf{1}^{+}$. It indeed displays an axial (S = ½) signal with hyperfine splitting due to the interaction of the electronic spin with the Cu nuclear spin (Figure 3-6c). The same spectrum was obtained at 100 K. The parameters obtained from simulation are $g_1 = g_2 = 2.042$, $g_3 = 2.205$, with $A_1 = A_2 = 2.5$, $A_3 = 19.7$ mT (Table 3-3). These values are typical for a (S = ½) mononuclear Cu(II) complexes, consistent with the unpaired electron residing in a Cu rather than ligand orbital. Thus, the ligand bridge in $\mathbf{1}^{2+}$ has been doubly oxidized (diiminoquinone ring), affording a closed-shell dioxidized salophen ligand coordinated to a single Cu(II) ion. Noteworthy, the g_3 values ordering is **1** (2.197) < $\mathbf{1H}^{+}$ (2.200) < $\mathbf{1}^{2+}$ (2.205), consistent with a ligand field within the order $\mathbf{1}^{2+}$ < $\mathbf{1H}^{+}$ < **1**. This trend perfectly matches the increase in positive charge at the bridging ring on going from **1** to $\mathbf{1}^{2+}$. The high g_3/A_3 value is also consistent with slightly increased distortion in the Cu(II) geometry in $\mathbf{1}^{2+}$.[144,145] Staab et al. described the X-ray crystal structure of doubly oxidized

1,2,4,5-tetrakis(dimethylamino)benzene.[41] They observed 1,3-diaminoallyl distributions of bond lengths in the two N-C-C-C-N fragments, which are consequently planar (Scheme 3-4). The fragments are strongly titled one against each other, inducing a twisted conformation of the benzene ring as a result of a diminished aromaticity. Such conformation may explain the increased distortion in $\mathbf{1}^{2+}$ in comparison with **1**.

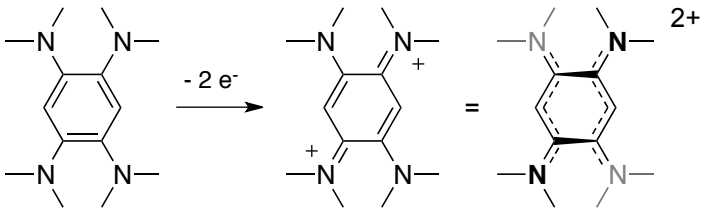

Scheme 3-4. Schematic representation of the twist occurring upon double oxidation of 1,2,4,5-tetraamino derivatives between the two 1,3-diaminoallyl moieties (bold = forwards, grey = backwards).[41]

Electrochemical oxidation of $\mathbf{2}^{2-}$ is accompanied by a quenching of the Cu(II) EPR signal (Figure 3-11). Spin quantification reveals that the residual Cu(II) signal accounts for 5-10% of the original one, in agreement with the Faraday yield of the electrolysis (0.95 electron removed) and RDE coulometry. Thus, the one-electron oxidized complex $\mathbf{2}^{-}$ is X-Band EPR-silent at 9 K in contrast to $\mathbf{1}^{+}$. By considering that $\mathbf{2}^{-}$ is a Cu(II)-radical complex, this result is not unexpected: The electron-withdrawing imino groups of **1** are involved in the coordination without need for deprotonation, making the oxidation potential of **1** very similar to that of the free ligand $H_2\mathbf{L}^{1}$. Regarding $\mathbf{2}^{2-}$, metal coordination is associated with deprotonation of the amide groups, which make them electron-donating and stronger ligands. As a consequence the unpaired electron resides closer to the metal center in $\mathbf{2}^{-}$, and the expected ZFS parameters are larger than for $\mathbf{1}^{+}$.

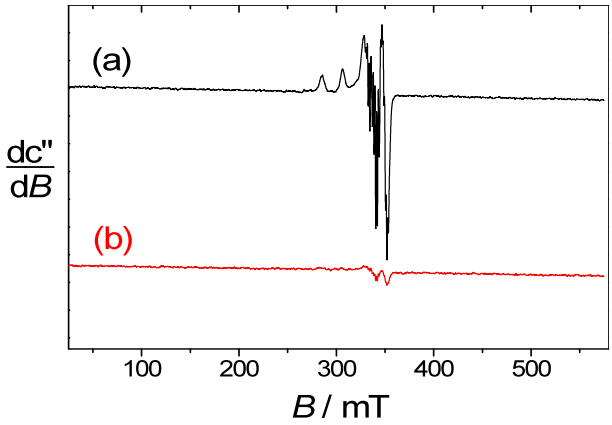

Figure 3-11. X-band EPR spectra of: $\mathbf{2}^{2-}$ (a, black) and $\mathbf{2}^{-}$ (b, red) generated by electrolysis at -30°C (1 mM in CH_2Cl_2, 0.1 M nBu$_4$ClO$_4$). Microwave Freq. 9.36 GHz power: 8 mW, Mod. Freq. 100 KHz, Amp: 0.3 mT. T = 9 K.

3.2.7 Computational investigation of the complexes

Energetic analysis. Energetic analysis was performed to discriminate between the two possible forms of $\mathbf{1}^{+}$ and $\mathbf{2}^{-}$: the triplet Cu(II)-radical or the singlet Cu(III) states. By looking at the HOMO-SOMO energy separation in parent complexes **1** and $\mathbf{2}^{2-}$, one can get insight into the oxidation locus of $\mathbf{1}^{+}$ and $\mathbf{2}^{-}$. The SOMOs of parent complexes **1** and $\mathbf{2}^{2-}$, mainly of 3d(x^2-y^2) metal character (see below), are only 1.5 and 4.9 kcal.mol^{-1} above their respective HOMOs, of ligand character. These rather small values highlight the close proximity of metal- and ligand-based orbitals. In this case, the oxidation is likely to occur on the HOMO because it alleviates the energy cost associated with having an electron pair. Accordingly, the calculated free energies of the two forms of both complexes in CH_2Cl_2 predict the Cu(II)-radical species to be lower in energy by 21.7 and 20.0 kcal mol^{-1}, respectively. For the doubly oxidized species $\mathbf{1}^{2+}$, we also considered the possibility to form two different species: the quartet Cu(II)-diradical or the doublet Cu(II) states. The calculated free energies of the two forms predict the pure Cu(II) species to be

lower in energy by 6.0 kcal mol^{-1}, showing that the second oxidation process is ligand-centered to provide a closed-shell ligand.

Geometry optimizations. The structural rearrangements on going from **1** to $\mathbf{1}^{+}$ and to $\mathbf{1}^{2+}$ are consistent with oxidations occurring on the central ring (Scheme 3-5, Table C-1 and Figures C-5 to C-7). Examination of the C–C and C–O bond lengths within the phenolic rings of **1** and $\mathbf{1}^{+}$ reveals no significant change upon oxidation, the bond distances being similar within ±0.01 Å in the range expected for a bis(phenolate) character. Similarly, the N–Cu and O–Cu bond lengths do not vary by more than 0.003 Å. In contrast, drastic variations are observed in the bond lengths within the central benzene ring on going from **1** to $\mathbf{1}^{+}$. The shortening of C1–N1, C1–C2, C3–C6 and C3–N2, concomitant with the lengthening of C2–C3, C3–C4, C4–C5 and C6–C1 highlights a quinoidal distribution of bond lengths within the tetraaminobenzene ring in $\mathbf{1}^{+}$. This is evidence that oxidation of **1** occurs on the bridge, affording a phenylene π-radical $\mathbf{1}^{+}$. The bonds in the central benzene ring of $\mathbf{1}^{2+}$ display the same trend as observed on going from **1** to $\mathbf{1}^{+}$, i.e. an α-diiminoquinone character showing that double oxidation occurs on the electron-rich bridge of **1**. Consequently, delocalization is mostly concentrated on two 1,3-diaminoallyl moieties, in line with the EPR results (Scheme 3-4). Finally, the same analysis applies when examining the structural rearrangements induced by oxidation of $\mathbf{2}^{2-}$ into $\mathbf{2}^{-}$ (Scheme 3-5, Table C-2 and Figures C-8 and C-9). No significant change occurs within the oxamate moieties, the bond lengths being similar within the ±0.01 Å level, while the N–Cu and O–Cu bond lengths do not vary by more than 0.013 Å. In contrast, important changes of bond lengths within the central benzene ring are observed on going from $\mathbf{2}^{2-}$ to $\mathbf{2}^{-}$. The shortening of C1–N1, C1–C2, C5–C6 and C4–N3, together

with the lengthening of C3–C4 and C6–C1 highlights a quinoidal character of the central ring in $\mathbf{2}^{2-}$. This is evidence that oxidation of $\mathbf{2}^{2-}$ also occurs on the bridge, affording a phenylene π-radical $\mathbf{2}^{-}$.

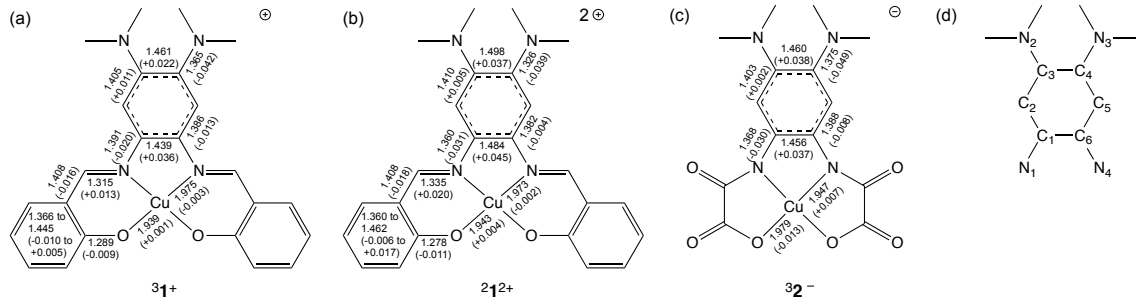

Scheme 3-5. Selected calculated bond lengths in (a) $^3\mathbf{1}^+$, (b) $^2\mathbf{1}^{2+}$ and (c) $^3\mathbf{2}^-$, together with the variations upon each 1e oxidation (in parentheses). *tert*-Butyl substituents in (a) and (b) were omitted for clarity. All species were left-right symmetric (± 0.001 Å). (d) Numbering used in the text.[1]

Electronic structures. The spin density plots for the parent complexes **1** and $\mathbf{2}^{2-}$ and for the dioxidized species $\mathbf{1}^{2+}$ are shown in Figure 3-12a,d while their localized SOMOs are depicted in Figure 3-13a,d. The SOMOs of **1**, $\mathbf{2}^{2-}$ and $\mathbf{1}^{2+}$ have a strong metal character (63, 61 and 61% of Cu 3d(x^2-y^2), respectively) with significant contributions of the coordinating atoms of the ligands due to the covalency of the metal-ligand bonds. Mulliken population analysis of these species supports a description as square-planar Cu(II) complexes with positive spin populations found at the Cu ion (0.57, 0.54 and 0.59), each coordinated oxygen (0.09, 0.07 and 0.02) and each coordinated nitrogen (0.12, 0.15 and 0.06, for **1**, $\mathbf{2}^{2-}$ and $\mathbf{1}^{2+}$ respectively). The spin density plots and the localized SOMOs of the monooxidized complexes, triplet $^3\mathbf{1}^+$ and $^3\mathbf{2}^-$ (see below), are shown in Figures 3-12b,e and 3-13b,e. In each case, the first SOMO is metal-based with a

[1] See Appendix C for details.

Cu 3d(x^2-y^2) contribution similar to that of the SOMOs in the parent complexes **1** and $\mathbf{2}^{2-}$. The second SOMO is ligand-based with a composition similar to that of the SOMOs in the oxidized proligands $(H_2\mathbf{L}^1)^+$ and $(Et_2H_2\mathbf{L}^2)^+$ with no contribution from the metal ion. The Mulliken population analysis of $\mathbf{1}^+$ and $\mathbf{2}^-$ point out that they can be best described as Cu(II)-radical species, both resulting from a ligand-centered oxidation process. The spin density is spread over the central part of the complexes, with positive spin populations found mainly at the Cu ion (0.57 for $\mathbf{1}^+$, 0.56 for $\mathbf{2}^-$) and the bridging unit (Figure 3-12b,e). Importantly, the coordinated nitrogens (N1 and N4, Scheme 3-5) hold more spin density in $\mathbf{2}^-$ than in $\mathbf{1}^+$, while the dimethylamino groups hold less (Figure 3-12b,e). This is in line with the greater participation of the better π-donor $N_{amidato}$ (formally negative) in the resonance structure of the radical, compared with the neutral N_{imine} donor. The composition of the second SOMO are fully consistent with this analysis (Figure 3-13b,e).

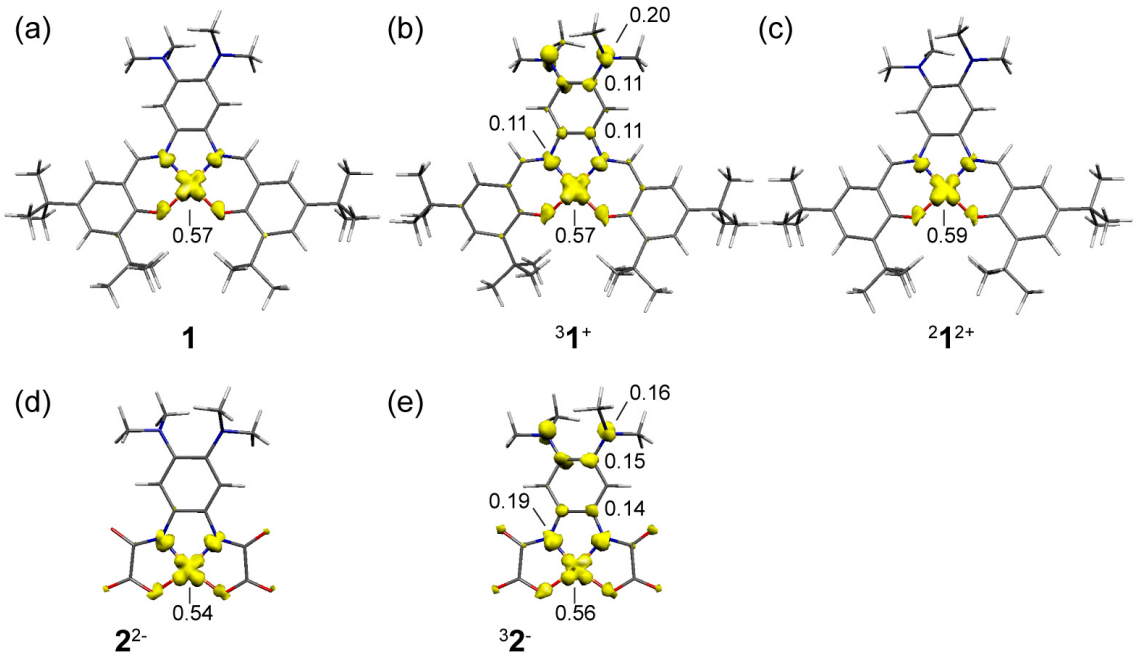

Figure 3-12. Spin density plots, including the values of the most important individual spin populations, for: (a) **1**, (b) triplet $\mathbf{1}^+$, (c) doublet $\mathbf{1}^{2+}$, (d) $\mathbf{2}^{2-}$, (e) triplet $\mathbf{2}^-$.

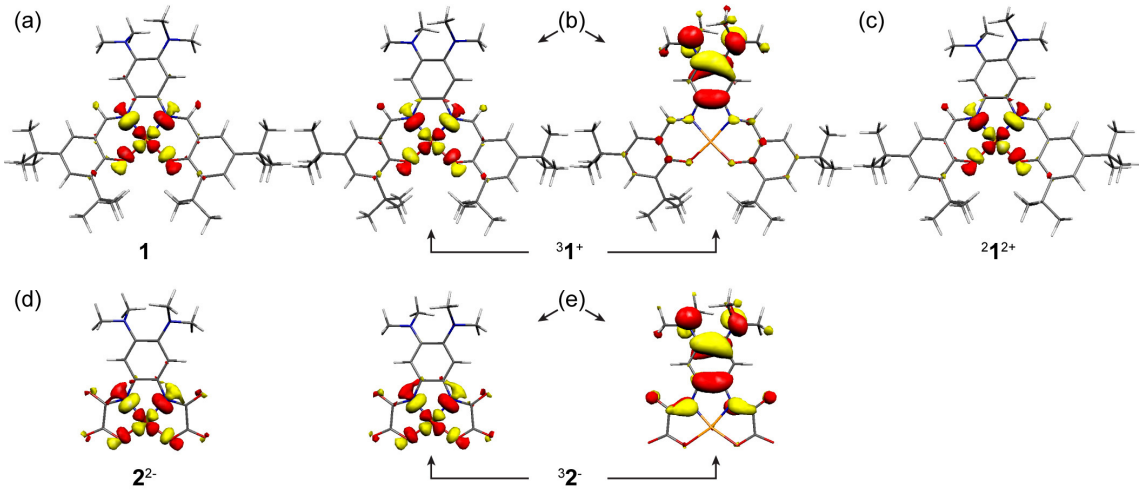

Figure 3-13. Localized SOMOs for: (a) **1**, (b) triplet $\mathbf{1}^{+}$, (c) doublet $\mathbf{1}^{2+}$, (d) $\mathbf{2}^{2-}$, (e) triplet $\mathbf{2}^{-}$.

Magnetic properties. The magnetic properties of $\mathbf{1}^{+}$ and $\mathbf{2}^{-}$ were investigated to get insight into their respective ground spin states. For $\mathbf{1}^{+}$, an exchange coupling constant J = +32 cm^{-1} (spatial overlap of 0.003) was obtained from Broken-Symmetry DFT calculations. This value shows that the two unpaired electrons of the molecule are weakly ferromagnetically coupled resulting in a triplet ground spin state (S = 1) in agreement with the data derived from EPR measurements. Moreover, it is worth noting that a ferromagnetic coupling was expected from the orthogonality of the two magnetic orbitals depicted on Figure 3-13b. Similar results were obtained in the case of $\mathbf{2}^{-}$ with a calculated exchange coupling constant of +99 cm^{-1} (spatial overlap of 0.056), consistent with a moderate ferromagnetic interaction and a triplet ground spin state for this species. The increased magnitude of the J value in $\mathbf{2}^{-}$ can be attributed to a better delocalization of the spin density onto the coordinated nitrogen atoms.

Since oxidized species $\mathbf{1}^{+}$ and $\mathbf{2}^{-}$ are magnetically-coupled systems with a total ground spin state $S > ½$, we have carried out CASSCF-based *ab initio* calculations in an attempt to model the zero-field splitting (ZFS) parameters of both complexes. The following values were obtained: $D = +0.024$ cm^{-1} and $E = + 0.267$ cm^{-1} for $\mathbf{1}^{+}$ and $D = +0.839$ cm^{-1} and $E = + 0.136$ cm^{-1} for $\mathbf{2}^{-}$, respectively (Table 3-3). In these complexes, the ZFS is caused by the combined effect of the magnetic dipole-dipole interaction and the exchange coupling anisotropy. The first one is the spin-spin contribution, which is a first-order term involving direct dipolar spin-spin interactions between pairs of electrons. This contribution is expected to be dominant in organic triplets or radicals and appears to be of prime importance in the present case with $D^{SS} = 0.027$ and 0.021 cm^{-1} for $\mathbf{1}^{+}$ and $\mathbf{2}^{-}$, respectively. The exchange contribution is a relativistic term that originates from the coupling of the excited state(s) and the ground state of the magnetic centers by spin-orbit interaction. The magnitude of this contribution was found to negligible for $\mathbf{1}^{+}$ and dominant for $\mathbf{2}^{-}$, with $D^{SOC} = 0.003$ and 0.848 cm^{-1}, respectively. The computed ZFS parameters for $\mathbf{1}^{+}$ is in fair agreement with the value derived from EPR measurements and confirm the assumption regarding the role of the substituent on the central ring in modulating the magnitude of D. Similarly, the ZFS parameter obtained for $\mathbf{2}^{-}$ is consistent with the experimental findings of an EPR-silent system at both X- and Q-bands, the calculated value being in a range matching the bandwidth limit for experimental detection. Moreover, one can connect the difference of ZFS parameters in $\mathbf{1}^{+}$ and $\mathbf{2}^{-}$ with the chemical nature of the ligand. In $\mathbf{2}^{-}$, we observe a greater delocalization of the spin density onto the coordinated nitrogens and thus the amidato groups allow for a better coupling of the metal center with the paramagnetic ligand.

Optical properties. TD-DFT calculations were undertaken on the optimized structures of the doublet states of **1**, $\mathbf{2}^{2-}$ and $\mathbf{1}^{2+}$ and the triplet states of $\mathbf{1}^{+}$ and $\mathbf{2}^{-}$ to confront the calculated electronic structure to the experimental UV-vis-NIR spectra (Figures 3-8 and 3-9, Table 3-4). For the parent complexes **1** and $\mathbf{2}^{2-}$, the calculations adequately reproduce the energy of the key features of the experimental spectra. The lowest-energy transition of **1** or $\mathbf{2}^{2-}$ arises from a ligand-to-metal charge transfer (LMCT) in which the s donor orbital is essentially distributed over the phenolate or the oxamate moieties, respectively (Figure 3-14 and 3-15). The second lowest-energy transition is of ligand-to-ligand charge-transfer (LLCT) origin with the donor orbitals being distributed over the central aromatic ring and the acceptor orbital being delocalized over the diimine or bis(oxamate) moiety. Calculations on the triplet state of $\mathbf{1}^{+}$ result in a good match to the experimental absorptions with those predicted by TD-DFT calculations. The agreement for the intensity of the transitions is fair, with the calculations predicting higher f^{calc} for the visible bands than for the NIR band. The lowest-energy transition arises from intra-ligand charge transfer (ILCT) since both the donor and acceptor orbitals are ligand-based MOs centered on the bridging radical unit. The second lowest-energy transition is of metal-to-ligand charge transfer (MLCT) origin with the donor being metal-centered and the acceptor being distributed on the central ring. The next two transitions are assigned as LLCT with donor orbitals on the phenolates and the bridging radical unit, respectively, while the acceptor orbital is delocalized over the diimine moiety. For the triplet state of $\mathbf{2}^{-}$**,** the positions and intensities of the transitions predicted by TD-DFT compare well with the experimental ones. The lowest-energy transition arises from ILCT since both the donor and acceptor orbitals are mainly distributed over

the bridging radical unit. The second lowest-energy transition is a bis(oxamate)-to-central-ring LLCT. For $\mathbf{1}^{2+}$, the agreement between calculations and experiment is fair. In order of increasing energy, the first band is a phenolate-to metal LMCT, the second is an intra-central-ring ILCT and the third is an LLCT from phenolate to the diimine moiety.

The key feature of these calculations is that the acceptor orbitals in the oxidized species are almost exclusively centered on the central ring. The only major difference between $\mathbf{1}^{n+}$ and $\mathbf{2}^{n+}$ species stems from the involvement of the diimine moiety in some higher-energy transitions of $\mathbf{1}^{+}$ and $\mathbf{1}^{2+}$. Overall, the agreement between experimental and calculated spectra not only confirms the nature and spin-states of the species, but also confirms that the central ring is the prime locus of oxidation in these complexes.

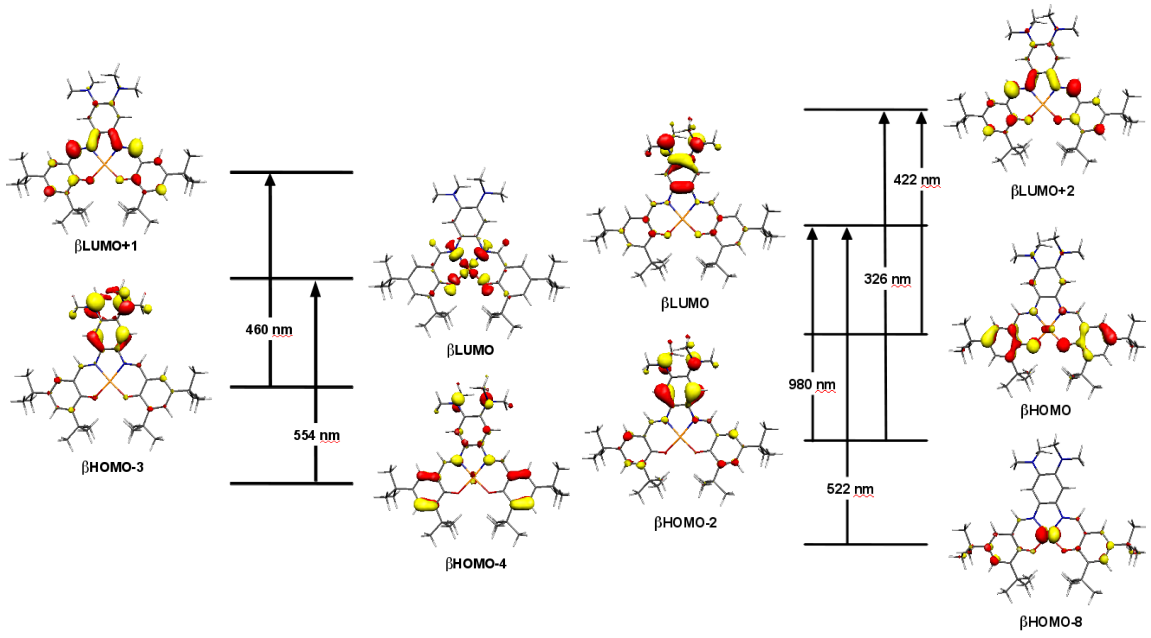

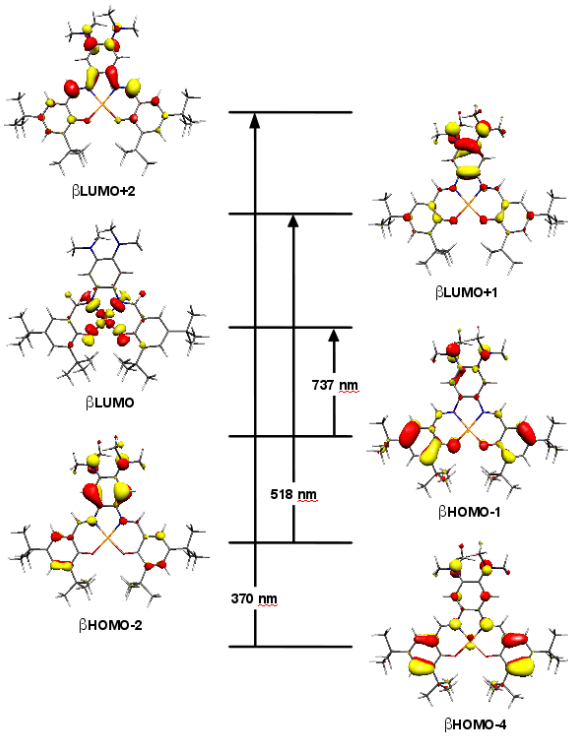

Figure 3-14. TD-DFT assignment of the UV-vis bands for **1** (top, left), triplet $\mathbf{1}^{+}$ (top, right) and doublet $\mathbf{1}^{2+}$ (bottom).

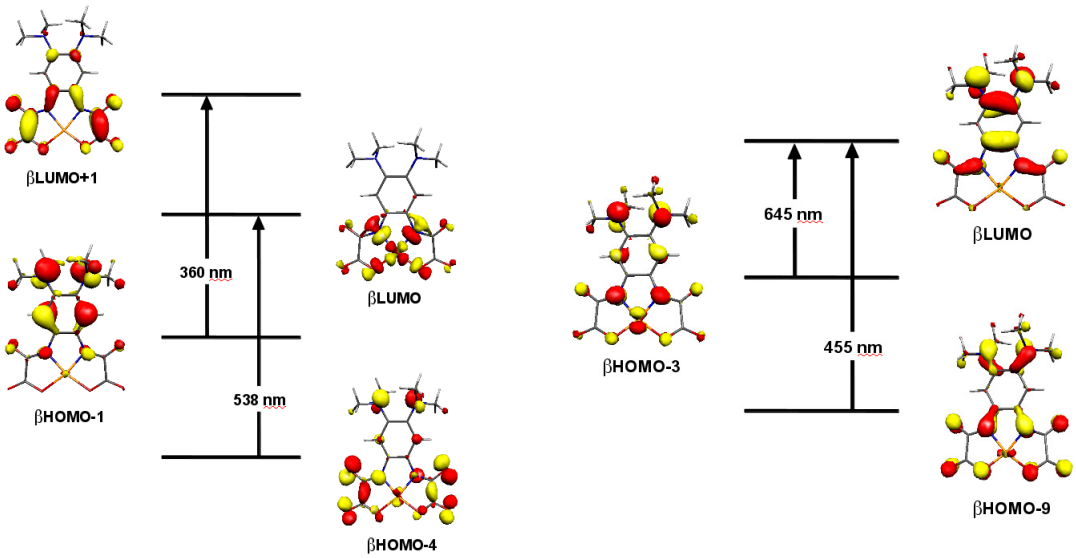

Figure 3-15. TD-DFT assignment of the UV-vis bands for $\mathbf{2}^{2-}$ (left), triplet $\mathbf{2}^{-}$ (right).

3.3 CONCLUSION

In summary, bis(dimethylamino) substitution on the central ring of the classic Cu(II)-salophen complex leads to two easily accessible and reversible redox processes on the central aromatic ring. Complex **1**, when oxidized, produces a stable radical, $\mathbf{1}^{+}$, followed by an α-diiminoquinone, $\mathbf{1}^{2+}$. The π-radical in $\mathbf{1}^{+}$, is ferromagnetically coupled to the unpaired electron in the d orbitals of Cu(II) forming an overall complex in a triplet (S = 1) state. The same methodology of substituting NMe_2 groups onto an oxamate-type Cu(II) complex, $\mathbf{2}^{2-}$, leads to one reversible redox process localized on the central aromatic moiety forming a radical, $\mathbf{2}^{-}$. This occurs at a lower potential than **1** due to the stronger donating ability of the amidates. The radical in complex $\mathbf{2}^{-}$ is also ferromagnetically coupled to the unpaired electron of Cu(II), again producing a triplet ground state. The two series of complexes highlight the potency of NMe_2 substituents to act as π-donors that confer ligands with two low-potential redox processes, a key feature to impart "noble" metal character to first-row transition metals.[5]

3.4 EXPERIMENTAL

3.4.1 Materials

Organics, reagents, solvents, and metal salts were obtained from commercial sources and used as received unless indicated otherwise. For oxidation studies, dichloromethane was degassed, dried over a solvent purification system, and then stored over activated 4 Å molecular sieves inside an inert-atmosphere glovebox filled with a dry dinitrogen atmosphere (less than 1 ppm in dioxygen and water). $H_2\mathbf{L}^{1}$ and $Et_2H_2\mathbf{L}^{2}$ were prepared by literature procedures.[30,139]

3.4.2 Characterization

Elemental CHN microanalyses were performed by the Microanalytical Service of the Institut de Chimie des Substances Naturelles (CNRS, France). Solution ^{1}H and ^{13}C NMR spectra were recorded on a Varian Innova 500 MHz instrument using tetramethylsilane as the internal reference. UV-vis-NIR solution spectra were recorded on Varian CARY 5E (250–1400 nm) and 5000 (1400–3300 nm) spectrophotometers. X-band EPR spectra were recorded on a Bruker EMX Plus spectrometer controlled with Xenon software and equipped with a Bruker teslameter. A Bruker nitrogen-flow cryostat connected to a high-sensitivity resonant cavity was used for 100 K measurements. An Oxford Instrument helium-flow cryostat connected to a dual-mode resonant cavity was used to run experiments at 25 K. The spectra were simulated using SIMFONIA software (Bruker). Cyclic voltammetry curves were recorded on a CHI 620 potentiostat in a standard three-electrode cell under an argon atmosphere. Electrochemical measurements were performed at either 298 K for the non-oxidized complexes or 243 K for the oxidized species to ensure as little decomposition as possible. An $AgNO_3/Ag$ (0.01 M) reference electrode was used. All of the potentials given in the text refer to the regular Fc^{+}/Fc redox couple used as the external reference. A vitreous carbon disk electrode (3 mm diameter) or a platinum disk (2 μm diameter) polished with 1 mm diamond paste was used as the working electrode.

3.4.3 X-ray Crystallography

Crystallographic analysis was performed on a Bruker APEX-DUO diffractometer or on a Kappa CCD Nonius diffractometer. The frames were integrated with the Bruker SAINT software package using a narrow-frame algorithm. Data were corrected for absorption effects using the multiscan method (SADABS). The structures were solved by direct methods and refined using the APEX2 or OLEX2 software packages (SHELXL instructions).[49] All non-hydrogen atoms were refined with anisotropic thermal parameters. Hydrogen atoms were generated in idealized positions, riding on the carrier atoms with isotropic thermal parameters.

3.4.4 Computational Details

All theoretical calculations were performed with the ORCA program package.[149] Full geometry optimizations were carried out for all complexes using the GGA functional BP86[53,150,151] in combination with the TZV/P[152] basis set for all atoms and by taking advantage of the resolution of the identity (RI) approximation in the Split-RI-J variant[55] with the appropriate Coulomb fitting sets.[56] Increased integration grids (Grid4 in ORCA convention) and tight SCF convergence criteria were used. Solvent effects were accounted for according to the experimental conditions. For that purpose, we used the CH_2Cl_2 (e= 9.08) solvent within the framework of the conductor like screening (COSMO) dielectric continuum approach.[57] The relative energies were obtained from single-point calculations using the B3LYP[59,153] functional together with the TZV/P basis set. They were computed from the gas-phase optimized structures as a sum of electronic energy, thermal corrections to free energy, and free energy of solvation. Optical

properties were predicted from additional single-point calculations using the same functional/basis set as employed before. Electronic transition energies and dipole moments for all models were calculated using time-dependent DFT (TD-DFT)[60–62] within the Tamm-Dancoff approximation.[63,64] To increase computational efficiency, the RI approximation[154] was used in calculating the Coulomb term and at least 30 excited states were calculated in each case. g-tensors and hyperfine coupling constants[154–157] were obtained from single-point calculations using the B3LYP functional. The EPR-II[67] basis set was employed for the ligands while scalar relativistic effects were accounted for the metal complexes. They were included with ZORA paired using the SARC def2-TZVP(-f) basis sets[158,159] and the decontracted def2-TZVP/J Coulomb fitting basis sets for all atoms. Increased integration grids (Grid4 and GridX4 in ORCA convention) and tight SCF convergence criteria were used in the calculation. The integration grids were increased to an integration accuracy of 11 (ORCA convention) for the metal center. Picture change effects were applied for the calculation of the hyperfine tensors. The Heisenberg isotropic exchange coupling constants *J* were evaluated from single point calculations based on the Broken Symmetry (BS) approach[160–162] using the B3LYP functional and the TZV/P basis set. The Yamaguchi formula[163,164] was used to estimate the exchange coupling constants *J* based on the Heisenberg–Dirac–van Vleck Hamiltonian.[165–168] Zero field splitting (ZFS) parameters were obtained from *ab initio* calculations based on the complete active space self-consistent field (CASSCF) approach. The spin-orbit coupling was calculated within a quasi-degenerate perturbation theory formalism where the SOC operator is diagonalized in a basis of multiconfigurational wave functions obtained from a full configuration interaction (CI) calculation in a limited set of active electrons and orbitals that were

obtained from a preceding CASSCF calculation.[169] The active space was chosen to consist of 12 active electrons occupying the five 3d-based molecular orbitals (MOs) and two ligand π-orbitals (CAS(12,7)). The CASSCF calculations were performed using the TZV/P basis set and were converged for the average of 10 triplet and 10 singlet roots. The SOC matrix was diagonalized on the basis of all possible triplet (21) and singlet (28) states. The spin-spin (SS) contribution to the ZFS was calculated on the basis of single root CASSCF (12,7) wave function.[169]

3.4.5 Syntheses

1: To a solution of $H_2\mathbf{L^1}$ (313 mg, 0.5 mmol) in CH_2Cl_2 (5 mL) is added dropwise a solution of $Cu(OAc)_2{\cdot}H_2O$ (200 mg, 1.0 mmol) in MeOH (15 mL). After 2 hours of mild reflux, the solvent is evaporated in vacuo and the crude is solubilized in fresh CH_2Cl_2 (50 mL). This solution is filtered over a SiO_2 pad to remove excess metal and the filtrate is evaporated until concentrated. After layering with MeOH and cooling to -20°C, the precipitate is collected by filtration and affords a burgundy/brown fluffy solid, complex **1**. Yield: 120 mg, 35%. Rf(SiO_2/CH_2Cl_2) 0.81. Anal. Calcd. for $C_{40}H_{56}CuN_4O_2$ (688.44 g/mol): C, 69.78; H, 8.20; N, 8.14. Found: C, 69.16; H 8.10; N 8.02. IR σ (cm^{-1}): 1585 (imine) and 1605 (imine). Single crystals of **1** were grown by very slow evaporation of a concentrated CH_2Cl_2 solution at 25°C.

$(PPh_4)_2\mathbf{2}{\cdot}2H_2O$: Under an inert atmosphere, $Et_2H_2\mathbf{L^2}$ (150 mg, 0.38 mmol) and 4.25 equivalents of NaOH (65 mg, 1.62 mmol) are dissolved in 10 mL of degassed water. A solution of $Cu(NO_3)_2{\cdot}3H_2O$ (92 mg, 0.38 mmol) in degassed water (20 mL) is added very slowly (1 drop per second) to the ligand solution under vigorous stirring. The mixture is

left to stir for 15 min after the last drop, then transferred to a separatory funnel. The complex is extracted portion wise in the air by the following procedure: adding 50 mL CH_2Cl_2 and a portion of PPh_4Cl, then mixing and separating the organic phase. This procedure is repeated until 2 equivalents of PPh_4Cl are added or while the organic phase remains deeply colored. The combined organic phases were filtered over paper and evaporated to dryness. The crude is triturated for 1h in acetone, filtered off, then triturated again in acetone overnight. The green solid of $(PPh_4)_2$**2**$\cdot 2H_2O$ is collected by filtration, washed with acetone and dried in vacuo. Yield: 197 mg, 35%. Anal. Calcd. for $C_{14}H_{14}CuN_4O_6 \cdot 2\ H_2O$ (1112.64 g/mol): C, 66.93; H, 5.25; N, 5.04. Found: C, 67.67; H 5.22; N 4.89. IR σ (cm^{-1}): 1688 (C=O amide), 1731 and 1748 (C=O ester). Purple/green birefringent single crystals of $(PPh_4)_2$**2** ($C_{14}H_{14}CuN_4O_6$) were grown by atmospheric diffusion of acetone into a concentrated CH_3CN solution of the complex.

3.5 SUPPORTING INFORMATION

For synthetic, crystallographic, spectroscopic and DFT details see Appendix C.

4. Implications of Strong Electron-Donating Groups in a Square-Planar Cobalt(III) Complex

4.0 Notes on the Chapter

The methodology of substituting electron-donating groups onto salophen-type ligands was successful in rendering them redox-active (see Chapters 2 and 3). Therefore the next step was to begin using this same methodology on other ligands. By making a simple modification of imine to amide, the resulting ligand is much more electron-rich. Such an electron-rich ligand may likely lead to lower redox potentials and provide interesting potential in bio-inspired catalysis. Recall the original purpose of research in this field was to impart noble metal character onto bio-available, earth-abundant metals. If the redox potential is considerably lowered, two successive one-electron redox processes may occur and quite close potentials, resulting in an overall effect of a two-electron oxidation.

Prior to describing the success story, we would like to highlight some of the major difficulties we had with the synthesis of the ligand and the complex described in this chapter. The synthesis of the ligand was adapted from previously published procedures[37] on similar compounds without the dimethylamino groups on the central aromatic ring. The main reaction to form the ligand was an addition of an amine to an acyl chloride with a base catalyst. The amine was generated by hydrogenation of 4,5-bis(dimethylamino)-1,2-dinitrobenzene[33] to afford a tetraamine intermediate. Due to the four strong electron-donating groups on the benzene ring, the compound is extremely electron-rich and reacts quickly with an oxidant like oxygen, thus decomposing rapidly in the air. Therefore, any

manipulations with this compound must be done under strict oxygen-free conditions. The acyl chloride also presented special conditions. Typically, the preparation of an acyl chloride involves harsh conditions like reflux in $SOCl_2$. However, the acyl chloride we had to prepare was heat-sensitive and decomposed readily above 30°C. The synthesis had to be adapted for lower temperatures, together with using standard equipment to maintain anhydrous conditions as the acyl chloride readily reacted with traces of water to reform the acid. This involves anhydrous solvents and vacuum line techniques. The next problem arose from the hydrogenation, which was only successful in methanol and produces water as a by-product. Once connected to the Schlenk line, the solvent had to be removed in vacuo, replaced with degassed THF and this solution had to be dried over Na_2SO_4 before it could be added to the acyl chloride.

As the ligand produced problems, so did the complexes. Nickel(II) was initially chosen for proof-of-concept and characterization reasons. But the nickel complex decomposed rapidly in solution in the time frame of a mass spectrometry measurement (it was only stable for minutes in acetone and CH_2Cl_2). The same behavior was observed for the copper(II), manganese(II), iron(II) and iron(III). When using cobalt(II) acetate, a green solution persisted in acetone and CH_2Cl_2 for hours. By MS, it was determined that a cobalt(III) complex was formed and was far more stable than other metals. When it came to purification, all traditional organic and inorganic methods failed, notably because the complex is charged and could only be made as a salt of one particular cation (NBu_4^+). A purification process was adapted from the literature[37] using Sephadex LH-20 lipophilic size exclusion chromatography. The column had to be packed with swollen LH-20 in methanol (by refluxing for 4 hours) and eluted with CH_2Cl_2. The column could not be

packed directly in CH_2Cl_2 because the LH-20 is less dense than the solvent and floats on it. Notwithstanding these difficulties, we were successful after months of work in isolating the desired complex and carrying out oxidation studies.

4.1 INTRODUCTION

Many cobalt complexes are used for catalysis, for example in propylene oxide polymerization,[170] regioselective ring opening of 1,2-epoxyethane,[171] oxygen activation for palladium-catalyzed aerobic 1,4-oxidation of 1,3-dienes,[172] C-C coupling,[95,120,173] C-C bond cleavage,[174] oxidation of styrene,[175] and olefin epoxidation.[176] Cobalt species are also found in single-molecule magnets,[177] in heme catabolism[178] and galactose oxidase models.[179] Also, several redox-active cobalt complexes have been used for their antimicrobial[180,181] and anti-tumor properties.[182] The redox properties of bio-inspired complexes containing electron-rich ligands have been extensively researched in an attempt to mimic the oxidation reactions catalyzed by metallo-enzymes in which radicals are involved during turnover, such as the porphyrin of hemic systems[19] (i.e. cytochrome P450) and tyrosine residues[20] (i.e. galactose oxidase). Following the same methodology, we previously designed several electron-rich ligands by incorporating dimethylamino substituents on classic ligand types such as salophen and phenylenebis(oxamate).[30,139] In the present work, we combine features of these main families in a ligand that bears a tetraanionic bis(amidate)-bis(phenolate) coordination environement[175,183–185] and a central bis(dimethylamino)-bis(amidato)-substituted aromatic ring (Scheme 4-1). The bonus of having a very electron-rich ligand is lower redox potentials of corresponding complexes so as to impart “noble metal” character (i.e. two-electron redox processes).[5] The present

communication reports the synthesis and characterization of the Co(III) complex of this ligand, $\mathbf{1}^-$, and its redox properties.

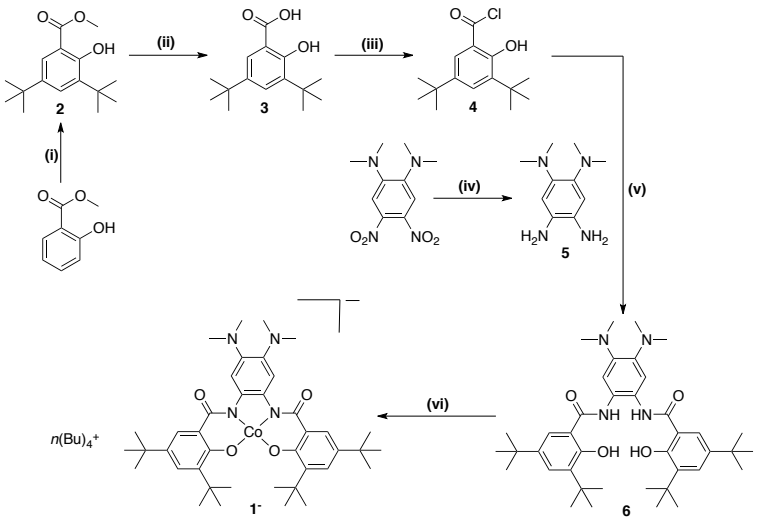

Scheme 4-1. Synthetic route towards $\mathbf{1}^-$. (i) *t*-BuOH, H_2SO_4, MeOH, 96%; (ii) KOH, MeOH, 96%; (iii) $SOCl_2$, THF, not isolated; (iv) H_2, Pd/C, MeOH, quantitative; (v) DIPEA, THF, N_2, 58%; (vi) $Co(OAc)_2$, nBu$_4$NOH, MeOH/DMF, 58%.

4.2 RESULTS AND DISCUSSION

4.2.1 Synthesis and structure of ligand and complexes

The synthesis of ligand **6**, in its protonated form, is a nucleophilic acyl substitution of **4** and **5** with diisopropylethylamine as a base. The reaction is carried out in strictly oxygen-free and anhydrous conditions since **4** reacts quickly with water to regenerate **3** and **5** decomposes in the presence of oxygen. **5** is prepared as previously described by hydrogenation of 4,5-bis(dimethylamino)-1,2-dinitrobenzene in a Parr hydrogenator at 4 atm of H_2 in methanol.[139] Since hydrogenation produces water and due to the water and methanol sensitivity of **4**, the "wet" solvent must be evaporated *in vacuo*, replaced with an aprotic solvent (THF) and dried over Na_2SO_4 before the reaction could continue. **4** is prepared by the chlorination of **3**, its carboxylic acid parent, in excess $SOCl_2$. Unreacted

$SOCl_2$ and THF must be removed *in vacuo* prior to the addition of **4** to **5**. (NBu_4)**1** is prepared by metallation of **6** with $Co(OAc)_2$, the ligand being deprotonated by tetrabutylammonium hydroxide. The complex is a salt and is sensitive to protic solvents. It was purified by lipophilic size-exclusion chromatography in Sephadex LH-20 eluting with CH_2Cl_2. Upon metallation, the metal oxidizes immediately from Co(II) to Co(III). The paramagnetic nature of Co(III) is evidenced by broad NMR signals spread over the [-7 – +18] ppm range. Mass spectrometry also provides evidence for this oxidation since the peak with highest intensity corresponds to the mono-negative complex (m/z = 713.5).

The solid-state structure of (NBu_4)**1** obtained by single-crystal X-ray diffraction confirms the identity of the complex, with a disordered NBu_4^+ cation stacked atop $\mathbf{1}^-$ (Figure 4-1). Due to this stacking and likely steric interactions between the *t*-butyl groups,[139] the coordination environment of the metal center is a distorted square-planar geometry. The Co ion lies essentially within the mean N_2O_2 plane (distance of 0.0026 Å) but a significant puckering is evidenced by a 14.64° angle between the two N-Co-O planes and a 27.83° angle between the two mean phenolate planes. Similarly, due to steric contact between their methyl groups, the NMe_2 substituents are angled away from the benzene plane, leading to limited resonance from these groups.

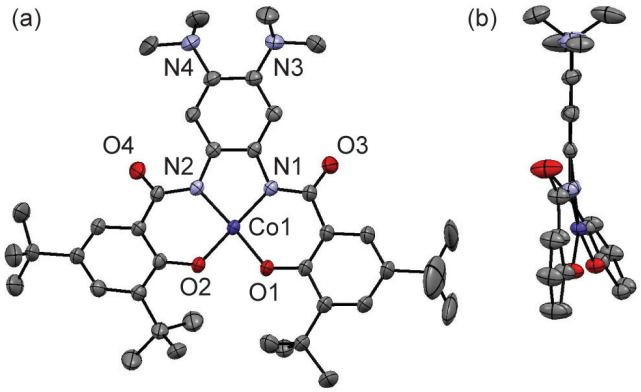

Figure 4-1. ORTEP representation at 50% ellipsoid probability of the cationic part of (*n*Bu$_4$)**1**: (a) top view; (b) side view with *t*Bu omitted. Hydrogen atoms were omitted for clarity. Selected bond lengths: Co1-N1 1.857(2), Co1-N2 1.840(2), Co1-O1 1.8036(19), Co1-O2 1.8238(19).

Table 4-1. Crystallographic data for (NBu$_4$)**1**.

CCDC number	990679
Empirical formula	$C_{56}H_{90}CoN_5O_4$
Formula weight	956.26
Temperature	117(2) K
Wavelength	1.54178
Crystal system	monoclinic
Space group	$P2_1/c$
a	8.5266(3) Å
b	37.8623(12) Å
c	17.2471(6) Å
α	90°
β	91.711(2)°
γ	90°
Volume	5565.5(3) Å^3
Z	4
Density (calculated)	1.141
Absorption coefficient	2.772
F(000)	2080
Crystal size	0.38 x 0.40 x 0.60 mm
Index ranges	$-10 \le h \le 10$, $-45 \le k \le 45$, $-19 \le l \le 20$
Reflections collected	79823
Independent reflections	10141
Parameters / restraints	756 / 646
Goodness of fit	1.037
Final R indices [I > 2σ(I)]	$R_1 = 6.03\%$, $wR_2 = 17.27\%$
R indices (all data)	$R_1 = 7.77\%$, $wR_2 = 18.62\%$
Largest diff. peak and hole	1.460 and -0.549 e Å^{-3}

4.2.2 Electrochemistry

The electrochemical behavior of (NBu_4)**1** was studied in CH_2Cl_2 (+ 0.1 M nBu_4NPF_6 as supporting electrolyte) by cyclic voltammetry. All potentials are referenced versus the Fc^+/Fc couple. The cyclovoltamogram of (NBu_4)**1** displays two oxidation waves at $E_{1/2}^2$ = -0.404 V (reversible) and $E_{1/2}^3$ = -0.058 V, and one reversible reduction wave at $E_{1/2}^1$ = -1.059 V, with some artifacts possibly due to impurities in the sample (Figure 4-2). The reduction likely corresponds to the Co^{III}/Co^{II} couple. A comparable bis(amidophenolate) Co(III) complex with an ethylene linker exhibits one reversible redox wave at $E_{1/2}$ = -0.96 V in DMF, which was assigned to the Co^{III}/Co^{II} couple.[185] In unmodified Co(II)-salophen complexes with two di-*tert*-butylphenolate moieties, the Co^{III}/Co^{II} couple is reported at -0.04 V (versus Fc^+/Fc).[186] The near 1 V difference is a testament to the much stronger donating ability of amidates that would stabilize higher oxidation states, in comparison with neutral imines. The oxidation potentials of various dimethylamino-substituted aromatic derivatives exhibit similar waves, thus supporting the hypothesis that the ligand-based oxidation occurs on the central aromatic bridge: $E_{1/2}$(2,3,6,7-tetrakis(dimethylamino)naphthalene) = 0.08 V (ΔE_p = 0.138 V) and $E_{1/2}$(1,4,5,8-tetrakis(dimethylamino)naphthalene) = 0.07 V (ΔE_p = 0.128 V).[39,40] Furthermore, the lack of oxidation processes at low potentials for the ethylene-linked bis(amidophenolate)[185] suggests that the oxidations in $\mathbf{1}^-$ are ligand-based and occur on the central aromatic ring.

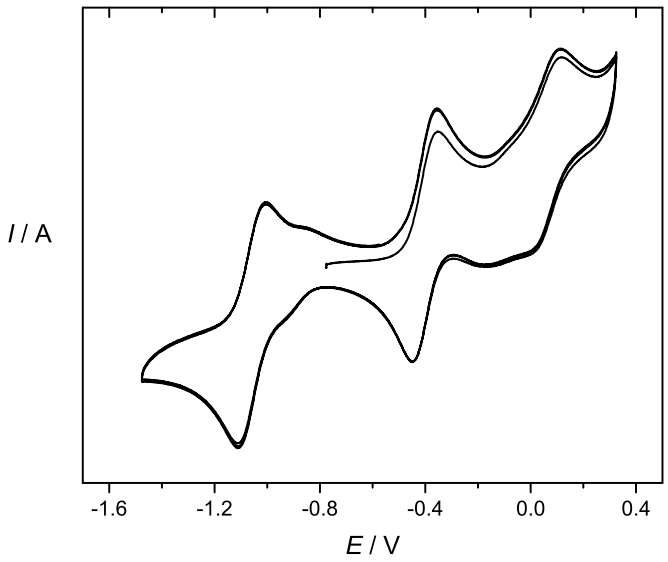

Figure 4-2. CV trace of (nBu$_4$)**1** in CH_2Cl_2 (+0.1 M nBu$_4$PF$_6$) at a glassy carbon working electrode. Potentials are relative to the Fc^+/Fc redox couple. Scan rate = 0.05 V/s. T = 298 K.

4.2.3 Oxidation of ligand and complex

The oxidized products of **6** and $\mathbf{1}^-$ were generated by chemical oxidation at -40°C in a UV-vis cell under N_2. The oxidant used for titrating was a 0.6 mM solution of acetylferrocenium triflate in CH_2Cl_2 ($E_{1/2}$ = 0.27 V vs. Fc^+/Fc).[45] The concentration of the oxidant solution was determined by titration with a solution of known concentration of a redox-active ligand ($Et_2H_2\mathbf{L}^2$, chapter 3) that exhibits a strong transition at 480 nm after oxidation. The volume of oxidant at the equivalence point was used to calculate its concentration.

Upon oxidation, the UV-vis spectrum of ligand **6** displays absorptions at 400 nm and 520 nm (Figure 4-3). This UV-vis behavior is very similar to what has been reported for $Et_2H_2\mathbf{L}^2$ in Chapter 3. Thus, by similarity between the two ligand structures, it is clear that this oxidation is occurring on the central ring of **6**, to generate a π-radical cation.

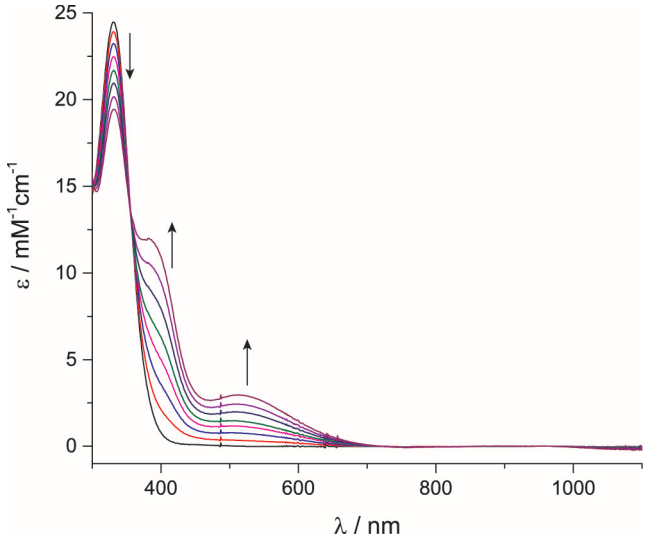

Figure 4-3. UV-vis titration of **6** with 0.6 mM acetylferrocenium triflate in CH_2Cl_2. T = 243 K, l = 1.000 cm.

The titration of $\mathbf{1}^-$ by acetylferrocenium shows two sequential oxidations going through two clear isosbestic points (Figure 4-4). This behavior suggests that the initial complex is successively converted into **1** then $\mathbf{1}^+$, consistent with the electrochemical findings of two well-separated redox processes.

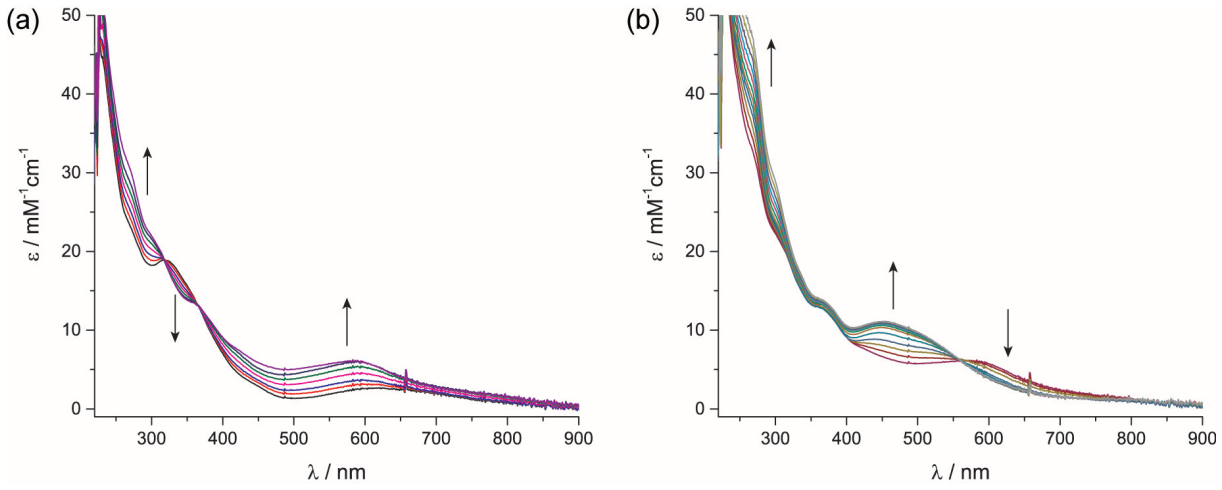

Figure 4-4. UV-vis titration of (nBu$_4$)**1** with 0.6 mM acetylferrocenium triflate in CH_2Cl_2. T = 243 K, l = 1.000 cm. Transitions corresponding to the first (a) and second (b) oxidation of $\mathbf{1}^-$ to **1**.

The superposition of the spectra of $\mathbf{1}^-$, **1** and $\mathbf{1}^+$ (Figure 4-5) reveals a strong similarity between these spectra and those obtained upon oxidations of the Ni(II) and Cu(II) bis(dimethylamino)-substituted salophen complexes, for which sequential oxidations occur mainly on the central ring (Scheme 4-2).[139,2] This suggests that the oxidation of **1** also occurs on the same moiety, to generate first a radical distributed on the central ring, then a iminoquinoid-type species in which the Co center remains in the +3 oxidation state. EPR experiments and DFT calculations are underway to elucidate the electronic structure of **1** and its oxidation products.

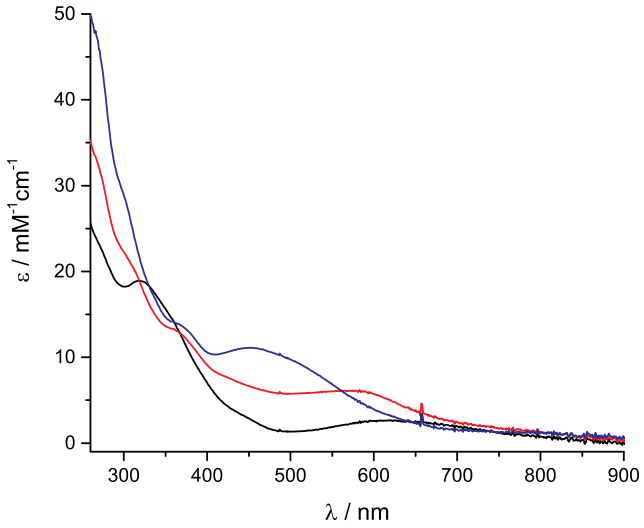

Figure 4-5. UV-vis spectra of $\mathbf{1}^-$ (black), **1** (red) and $\mathbf{1}^+$ (blue) extracted upon titration of (nBu$_4$)**1** with 0-2 equivalents of acetylferrocenium triflate in CH_2Cl_2. T = 243 K, l = 1.000 cm.

[2] See Chapter 3.

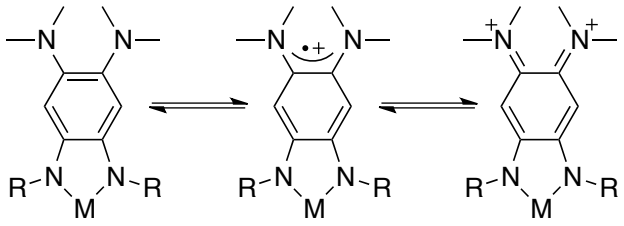

Scheme 4-2. Two sequential one-electron ligand-based oxidations located on the central aromatic ring resulting in a Würster's Blue-type[142] radical cation, followed by a diiminoquinone.

4.3 CONCLUSION

Recent publications highlight the necessity of precisely describing the electronic structure of cobalt complexes and the involvement of Co-radical states during catalytic turnover.[187–189] In this context, bis(dimethylamino) substitution is a means to ascertain ligand-based oxidations, thus keeping the metal ion in a known oxidation state. We are currently deciphering the repercussions of this strategy onto the reactivity of the substituted complexes.

4.4 EXPERIMENTAL

4.4.1 Materials

Organics, solvents and metal salts were obtained from commercial sources and used as received unless indicated otherwise. For oxidation studies, dichloromethane was degased and dried over an MBraun solvent purification system, then stored over activated 4Å molecular sieves in glass bottles inside an inert-atmosphere glovebox (MBraun Labmaster) filled with dry N_2 atmosphere (less than 1 ppm in dioxygen and water).

4.4.2 Characterization

Elemental CHN microanalyses were performed by the Laboratoire d'analyse élémentaire (Université de Montréal, Canada). Solution ^{1}H and ^{13}C NMR spectra were recorded on a Varian Innova 500 MHz instrument using tetramethylsilane as internal reference. Low temperature UV-vis spectra were recorded on a Agilent 8453 spectrophotometer equipped with a Unizoku USP-203-A cryostat. Cyclic voltammetry (CV) curves were recorded on a Bio-Logic SP-150 potentiostat in a standard three-electrode cell under Argon atmosphere.

Electrochemical measurements were performed at 298 K. An AgCl/Ag reference electrode was used. All the potentials given in the text are referenced to the Fc^{+}/Fc redox couple used as external reference. A vitreous carbon disc electrode (3 mm diameter) was used as working electrode. A 0.1 M solution of $n Bu_4PF_6$ in CH_2Cl_2 was used as the supporting electrolyte. Approximately 5 mg of analyte was dissolved in 3 mL of the electrolyte solution in the electrochemical cell. The Argon atmosphere was provided through a CH_2Cl_2 bubbler. Unless otherwise stated, a scan rate of 0.05 V/s was maintained throughout the cyclovoltammetric experiment.

4.4.3 X-ray crystallography

X-ray crystallographic analysis was performed using the microfocus Cu-Kα source of a Bruker APEX-DUO diffractometer. The frames were integrated with the Bruker SAINT software package using a narrow-frame algorithm. Data were corrected for absorption effects using the multi-scan method (SADABS). The structures were solved by direct methods and refined using the Bruker APEX2 software Package (SHELXL

instructions).[38] All non-hydrogen atoms were refined with anisotropic thermal parameters. Hydrogen atoms were generated in idealized positions, riding on the carrier atoms, with isotropic thermal parameters.

4.4.4 Syntheses

AcFcOTf (acetylferrocenium triflate). The synthesis was inspired by previously published procedures.[45] In an inert atmosphere glovebox, silver(I) triflate is mixed with a slight excess of acetylferrocene in diethyl ether and stirred for one hour. The mixture is filtered over a celite pad to remove excess acetylferrocene dissolved in ether, *n.b.* acetylferrocenium triflate and silver(0) are not soluble in diethyl ether. Approximately 10 mL of CH_2Cl_2 is added over the celite pad to dissolve the acetylferrocenium triflate and leave the silver(0) on the filter. Affording a deep blue solution that can be titrated or used as is.

5 was prepared by previously published procedures.[139]

Methyl 3,5-di-*tert*-butylsalicylate (**2**). Concentrated H_2SO_4 (8.0 mL) is mixed with a solution of freshly distilled *t*-BuOH (94.1 mmol, 9.0 mL) and MeOH (2.3 mL) on ice. Once cooled to ~ 0°C, methyl salicylate (23 mmol, 3 mL) is added dropwise with vigorous stirring. After complete addition, the solution is allowed to warm up to 25°C, then is heated to 40°C. The reaction progression can be followed by TLC (SiO_2: 5% MeOH/CH_2Cl_2), once the starting material is completely consumed, distilled H_2O is added to quench the reaction and $NaHCO_3$ is added until neutral pH is reached. The organic phase is extracted by CH_2Cl_2 and dried over Na_2SO_4. The solvent is removed *in vacuo* to afford a white solid (5.8 g, 96%).

3,5-di-*tert*-butylsalicylic acid (**3**). NaOH (125 mmol, 5.0 g) is dissolved in 75 mL distilled H_2O; to this solution is added **2** (23 mmol, 6.1 g) without further purification. The reaction mixture was heated under reflux for 24 hours (the white product dissolved after ~2 hours). The solution is then poured over 150 mL of an ice/water mix and 10% HCl is added until acidic pH is reached. The white precipitate is collected by filtration, washed with distilled water then dried in a vacuum oven at 50°C for several days (5.5 g, 96%).

3,5-di-*tert*-butylsalicyl chloride (**4**). To 100 mL THF is added **3** (8 mmol, 2.0 g) and the flask is cooled in an ice bath. Freshly distilled $SOCl_2$ (25 mL) is placed in an addition funnel and is added dropwise onto the cooled solution. A stream of N_2 is maintained in the reaction flask to discourage reactions with atmospheric moisture. The reaction is stirred overnight on ice, allowing the ice to melt slowly to finish the reaction at room temperature. Excess $SOCl_2$ is removed *in vacuo* along with the solvent. Fresh anhydrous THF is added to the crude oil and the solvent is removed *in vacuo* again. This is repeated twice more to remove all excess $SOCl_2$ affording a yellow/brown oil that is extremely sensitive to moisture and must be used right away. No characterization could be done.

4,5-bis(dimethylamino)benzene-1,2-bis(3,5-di-*tert*-butylsalicylamide) (**6**). A solution of **5** (4 mmol, 1.0 g) in MeOH[139] is removed from a Parr hydrogenator and is immediately blanketed with Ar gas (**5** is extremely oxygen-sensitive). All subsequent procedures must be completed under strict oxygen-free and anhydrous conditions. The catalyst is removed by filtration over Celite and the filter is washed with MeOH (~25 mL). The solvent is removed *in vacuo* and replaced with THF (100 mL). The solution is then poured over oven-dried Na_2SO_4 to remove traces of H_2O and placed in a dry 3-neck flask.

Diisopropylethylamine (8 mmol) is added to **5** in THF. Meanwhile, **4** in 100 mL THF is placed into an addition funnel connected to the 3-neck flask. Dropwise, **4** is added to **5** at 25°C and after complete addition, the solution is refluxed for 24 hours. Once complete, the material can now be handled in the air. The solvent is removed *in vacuo* and the crude is taken up in 100 mL CH_2Cl_2. The organic phase is washed with $NaHCO_3$, H_2O and saturated NaCl, and dried over Na_2SO_4. The solvent is removed *in vacuo* to afford a brown solid. The crude is dissolved in just enough CH_2Cl_2 (~5 mL) and is layered with MeOH (~200 mL). The solution is allowed to crystalize at 25°C for 24 hours and at -20°C for another 24 hours to afford a yellow powder, compound **6**. Yield: 1.5 g, 58%. R_f (SiO_2/1% MeOH/CH_2Cl_2) 0.77. Anal. Calcd. for $C_{40}H_{58}N_4O_4 \cdot CH_3OH$ (690.47 g/mol): C, 71.27; H, 9.04; N, 8.11. Found: C, 72.17; H, 9.04; N, 8.21. ^{1}H NMR ($CDCl_3$, 500 MHz): δ 1.28 (s, 18H, *t*-Bu), 1.42 (s, 18H, *t*-Bu), 2.74 (s, 12H, NCH_3), 6.95 (s, 2H, central aromatic), 7.39 (d, J_{12} = 2.5 Hz, 2H, phenol), 7.48 (d, J_{12} = 2.0 Hz, 2H, phenol), 8.77 (s, 2H, amide), 12.50 (s, 2H, OH). ^{13}C NMR ($CDCl_3$, 500 MHz): δ 29.38, 31.39, 34.36, 35.24, 41.12, 113.02, 114.87, 120.13, 123.48, 129.50, 138.29, 140.46, 143.98, 159.21, 170.19.

(*n*Bu_4)**1**. To a solution of **6** (0.14 mmol, 100 mg) and $Co(OAc)_2 \cdot 4H_2O$ (0.20 mmol, 50 mg) in 10 mL DMF is added a 1M solution of nBu_4OH in MeOH (0.72 mmol, 720 μL). The reaction is allowed to stir at 80°C for 4 hours. The solvent is removed *in vacuo* and the crude is further dried over strong vacuum. The crude is dissolved in minimal CH_2Cl_2 (~8 mL) and is purified by lipophilic flash chromatography (Sephadex LH-20, ~20 g dry) eluting with CH_2Cl_2 at 4 psi (120 mL/min). The forerun (~10 mL) is discarded and the remaining colored solution is collected and evaporated *in vacuo* to afford a deep green

solid on the flask walls. Yield: 94 mg, 70%. Anal. Calcd. for $C_{56}H_{90}CoN_5O_4$ (955.63 g/mol): C, 70.43; H, 9.49; N, 7.32. Found: C, 70.18; H, 9.42; N, 7.43. ESI-QTOF MS(-): 713.3 m/z (corresponding to $\mathbf{1}^-$). ^{1}H NMR ($CDCl_3$, 500 MHz): δ -5.12, -1.80, 1.36, 3.94, 8.27, 17.28. Single crystals can be prepared for X-ray diffraction by diffusion of a solution of **1** in CH_2Cl_2 into pentane.

5. Conclusion

For the past few years, the field of catalysis has been turning its focus to nature. Bio-inspired catalysts have been emerging more and more and the use of noble metal catalysts has seen an appreciable loss of attention. For environmental, economic or socio-political reasons, noble metal catalysts are being replaced with earth-abundant bio-available metals. In redox chemistry, one methodology of imparting noble metal character to first-row transition metals is to tailor the electronics of the complex by modifying the electron-donating strength of the ligand. The present work has shown that the approach of substituting the central aromatic bridge of classic ligands with dimethylamino groups ($H_2\mathbf{L^1}$, $Et_2H_2\mathbf{L^2}$ and $H_4\mathbf{L^3}$, Scheme 5-1) provides an elegant method to access two one-electron ligand-based oxidations at low redox potentials.

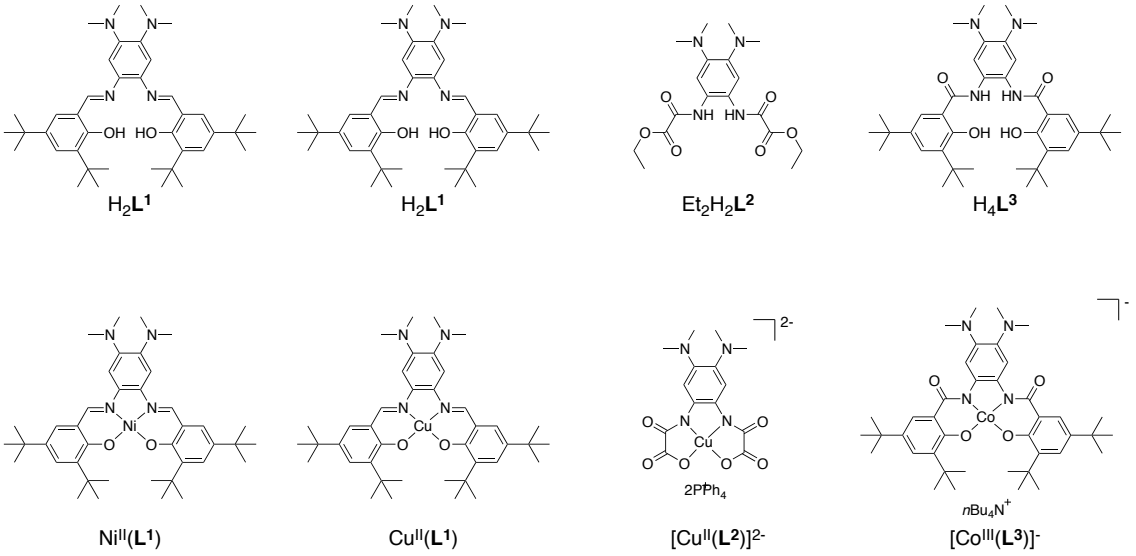

Scheme 5-1. Summary of the ligands (top) and corresponding complexes (bottom)

$[Ni^{II}(\mathbf{L^1})]$ and $[Cu^{II}(\mathbf{L^1})]$ exhibit very similar electrochemical and UV-vis-NIR properties. These complexes undergo two easily accessible and reversible one-electron oxidations at much lower potentials than comparable complexes. They are transiently oxidized to form a π-radical on the central aromatic moiety, followed by an α-diiminoquinone. $[Cu^{II}(\mathbf{L^1})]^{+}$ demonstrates ferromagnetic coupling between the radical and the Cu^{II} unpaired electron.

$[Cu^{II}(\mathbf{L^2})]^{2-}$ possesses a more electron-rich ligand due to the presence of two deprotonated amidates and undergoes two oxidations at lower potential than for $[Cu^{II}(\mathbf{L^1})]$. As expected, the oxidations occur on the central ring, though with greater participation of the coordinating nitrogens due to their negative charge. In $[Cu^{II}(\mathbf{L^2})]^{2-}$, the radical is thus delocalized in closer proximity to the metal center compared with $[Cu^{II}(\mathbf{L^1})]^{+}$, which leads to a stronger magnetic coupling.

Ligand $(\mathbf{L^3})^{4-}$ is analogous to $(\mathbf{L^1})^{2-}$, considering the replacement of imines by amidates, and to $(\mathbf{L^2})^{4-}$, given the replacement of carboxylate by phenolates. Unfortunately, it was impossible to compare its Ni(II) and Cu(II) complexes with those of $(\mathbf{L^1})^{2-}$ or $(\mathbf{L^2})^{4-}$ because of their instability. The only complex we were able to prepare, $[Co^{III}(\mathbf{L^3})]^{-}$, behaves similarly to the above complexes, with two low-potential oxidations. Preliminary experiments suggest that the oxidations also take place on the central ring.

The apparent trend is that by increasing the out-of-plane π-electron density of the ligand, one can tailor the electronic properties of a complex, rendering it highly oxidizable away from the metal. The metal thus remains in one redox state for which the reactivity is known. These findings contribute significantly to the field of bio-inspired

redox chemistry and may provide support in the search of new bio-inspired redox catalysts.

6. References

(1) Miyaura, N.; Yamada, K.; Suzuki, A. *Tetrahedron Lett*. **1979**, *20*, 3437–3440.

(2) Heck, R. F.; Nolley, J. P. *J. Org. Chem*. **1972**, *37*, 2320–2322.

(3) Sonogashira, K.; Tohda, Y.; Hagihara, N. *Tetrahedron Lett*. **1975**, *16*, 4467–4470.

(4) Blanchard, S. S.; Derat, E.; Desage-El Murr, M.; Fensterbank, L.; Malacria, M.; Mouriès-Mansuy, V. *Eur. J. Inorg. Chem*. **2012**, *2012*, 376–389.

(5) Chirik, P. J.; Wieghardt, K. *Science* **2010**, *327*, 794–795.

(6) Hamilton, G. a.; Adolf, P. K.; De Jersey, J.; DuBois, G. C.; Dyrkacz, G. R.; Libby, R. D. *J. Am. Chem. Soc*. **1978**, *100*, 1899–1912.

(7) Whittaker, M.; Whittaker, J. *J. Biol. Chem*. **1990**, *265*, 9610–9613.

(8) Green, M. T. *Curr. Opin. Chem. Biol*. **2009**, *13*, 84–88.

(9) Shaik, S.; Lai, W.; Chen, H.; Wang, Y. *Acc. Chem. Res*. **2010**, *43*, 1154–1165.

(10) Stubbe, J.; Donk, W. A. Van Der. *Chem. Rev*. **1998**, *2665*.

(11) Storr, T.; Wasinger, E. C.; Pratt, R. C.; Stack, T. D. P. *Angew. Chem. Int. Ed*. **2007**, *46*, 5198–5201.

(12) Orio, M.; Jarjayes, O.; Kanso, H.; Philouze, C.; Neese, F.; Thomas, F. *Angew. Chem. Int. Ed*. **2010**, *122*, 5109–5112.

(13) Kochem, A. A.; Jarjayes, O.; Baptiste, B.; Philouze, C.; Vezin, H. H.; Tsukidate, K.; Tani, F.; Orio, M.; Shimazaki, Y.; Thomas, F. *Chem. Eur. J*. **2012**, *18*, 1068–1072.

(14) Chiang, L.; Kochem, A.; Jarjayes, O.; Dunn, T. J.; Vezin, H.; Sakaguchi, M.; Ogura, T.; Orio, M.; Shimazaki, Y.; Thomas, F.; Storr, T. *Chem. Eur. J*. **2012**, *18*, 14117–14127.

(15) Benisvy, L.; Kannappan, R.; Song, Y.-F.; Milikisyants, S.; Huber, M.; Mutikainen, I.; Turpeinen, U.; Gamez, P.; Bernasconi, L.; Baerends, E. J.; Hartl, F. F.; Reedijk, J. *Eur. J. Inorg. Chem*. **2007**, *2007*, 637–642.

(16) Storr, T.; Verma, P.; Shimazaki, Y.; Wasinger, E. C.; Stack, T. D. P. *Chem. Eur. J*. **2010**, *16*, 8980–8983.

(17) Dunn, T. J.; Webb, M. I.; Hazin, K.; Verma, P.; Wasinger, E. C.; Shimazaki, Y.; Storr, T. *Dalton Trans*. **2013**, *42*, 3950–3956.

(18) Lyaskovskyy, V.; de Bruin, B. *ACS Catal*. **2012**, *2*, 270–279.

(19) Ortiz de Montellano, P. R. *Chem. Rev*. **2010**, *110*, 932–948.

(20) Kaim, W.; Schwederski, B. *Coord. Chem. Rev*. **2010**, *254*, 1580–1588.

(21) Kaim, W. *Inorg. Chem.* **2011**, *50*, 9752–9765.

(22) Kadish, K. M.; Caemelbecke, E. V; Royal, G. In *The Porphyrin Handbook*; Kadish, K. M.; Smith, K. M.; Guilard, R., Eds.; Academic Press: London, 2000; pp. 1–114.

(23) Chaudhuri, P.; Wieghardt, K. *Prog. Inorg. Chem.* **2001**, *50*, 151–216.

(24) Thomas, F. *Eur. J. Inorg. Chem.* **2007**, *2007*, 2379–2404.

(25) Pierpont, C. G.; Lange, C. W. *Prog. Inorg. Chem.* **1994**, *41*, 331–442.

(26) Chaudhuri, P.; Verani, C. N.; Bill, E.; Bothe, E.; Weyhermüller, T.; Wieghardt, K. *J. Am. Chem. Soc.* **2001**, *123*, 2213–2223.

(27) Ray, K.; Petrenko, T.; Wieghardt, K.; Neese, F. *Dalton Trans.* **2007**, 1552–1566.

(28) Gordon-wylie, S. W.; Claus, B. L.; Horwitz, C. P.; Leychkis, Y.; Workman, J. M.; Marzec, A. J.; Clark, G. R.; Rickard, C. E. F.; Conklin, B. J.; Sellers, S.; Yee, G. T.; Collins, T. J.; Workman, Â. M. *Chem. Eur. J.* **1998**, *4*, 2173–2181.

(29) Aukauloo, A.; Ottenwaelder, X.; Ruiz, R.; Poussereau, S.; Pei, Y.; Journaux, Y.; Fleurat, P.; Volatron, F.; Cervera, B.; Mun, M. C.; Muñoz, M. C. *Eur. J. Inorg. Chem.* **1999**, *1999*, 1067–1071.

(30) Ottenwaelder, X.; Ruiz-García, R.; Blondin, G.; Carasco, R.; Cano, J.; Lexa, D.; Journaux, Y.; Aukauloo, A.; Ruiz-Garcia, R. *Chem. Commun.* **2004**, 504–505.

(31) Ottenwaelder, X.; Aukauloo, A.; Journaux, Y.; Carrasco, R.; Cano, J.; Cervera, B.; Castro, I.; Curreli, S.; Muñoz, M. C.; Roselló, A. L.; Soto, B.; Ruiz-Garcia, R. *Dalton Trans.* **2005**, 2516–2526.

(32) Tondreau, A. M.; Milsmann, C.; Patrick, A. D.; Hoyt, H. M.; Lobkovsky, E.; Wieghardt, K.; Chirik, P. J. *J. Am. Chem. Soc.* **2010**, *132*, 15046–15059.

(33) Cheeseman, G. W. H. *J. Chem. Soc.* **1962**, 1170.

(34) Berg, K. E.; Pellegrin, Y.; Blondin, G.; Ottenwaelder, X.; Journaux, Y.; Canovas, M. M.; Mallah, T.; Parsons, S.; Aukauloo, A. *Eur. J. Inorg. Chem.* **2002**, 323–325.

(35) Lassalle-Kaiser, B.; Guillot, R.; Aukauloo, A. *Tetrahedron Lett.* **2007**, *48*, 7004–7006.

(36) Rotthaus, O.; Jarjayes, O.; Philouze, C.; Pérez Del Valle, C.; Thomas, F.; Del Valle, C. P. *Dalton Trans.* **2009**, 1792–1800.

(37) Rotthaus, O.; Thomas, F.; Jarjayes, O.; Philouze, C.; Saint-Aman, E.; Pierre, J.-L. *Chem. Eur. J.* **2006**, *12*, 6953–6962.

(38) Thomas, F.; Jarjayes, O.; Duboc, C.; Philouze, C.; Saint-Aman, E.; Pierre, J. L. *Dalton Trans.* **2004**, 2662–2669.

(39) Elbl-Weiser, K.; Krieger, C.; Staab, H. A. *Angew. Chem. Int. Ed. Engl.* **1990**, *29*, 211–213.

(40) Barth, T.; Krieger, C.; Neugebauer, F. A.; Staab, H. A. *Angew. Chem. Int. Ed. Engl.* **1991**, *30*, 1028–1030.

(41) Elbl, K.; Krieger, C.; Staab, H. A. *Angew. Chem. Int. Ed. Engl.* **1986**, *25*, 1023–1024.

(42) Shimazaki, Y.; Tani, F.; Fukui, K.; Naruta, Y.; Yamauchi, O. *J. Am. Chem. Soc.* **2003**, *125*, 10512–10513.

(43) Shimazaki, Y.; Stack, T. D. P.; Storr, T. *Inorg. Chem.* **2009**, *48*, 8383–8392.

(44) Shimazaki, Y.; Arai, N.; Dunn, T. J.; Yajima, T.; Tani, F.; Ramogida, C. F.; Storr, T. *Dalton Trans.* **2011**, *40*, 2469–2479.

(45) Connelly, N. G.; Geiger, W. E. *Chem. Rev.* **1996**, 877-910.

(46) Neugebauer, F. A.; Funk, B.; Staab, H. A. *Tetrahedron Lett.* **1994**, *35*, 4755–4758.

(47) Speiser, B.; Würde, M.; Maichle-Mössmer, C. *Chem. Eur. J.* **1998**, *4*, 222–233.

(48) Jacobsen, E. N.; Liu, J. *Org. Synth.* **2004**, *10*, 96–101.

(49) Sheldrick, G. M. SHELXL-97, Program for Crystal Structure Refinement, 1997.

(50) Neese, F. ORCA - an ab initio, Density Functional and Semiempirical Program Package, 2.8.0, 2010.

(51) Perdew, J. P. *Phys. Rev. B* **1986**, *33*, 8822–8824.

(52) Perdew, J. P. *Phys. Rev. B* **1986**, *34*, 7406.

(53) Becke, A. D. *Phys. Rev. A* **1988**, *38*, 3098–3100.

(54) Schäfer, A.; Huber, C.; Ahlrichs, R. *J. Chem. Phys.* **1994**, *100*, 5829–5835.

(55) Neese, F. *J. Comput. Chem.* **2003**, *24*, 1740–1747.

(56) Weigend, F. *Phys. Chem. Chem. Phys.* **2006**, *8*, 1057–1065.

(57) Klamt, A.; Schüürmann, G. *J. Chem. Soc. Trans.* **1993**, 799–805.

(58) Becke, A. D. *J. Chem. Phys.* **1993**, *98*, 5648–5652.

(59) Lee, C. T.; Yang, W. T.; Parr, R. G. *Phys. Rev. B* **1988**, *37*, 785–789.

(60) Casida, M. E. *Recent Advances in Density Functional Methods*; Chong, D. P., Ed.; World Scientific: Singapore, 1995.

(61) Stratmann, R. E.; Scuseria, G. E.; Frisch, M. J. *J. Chem. Phys.* **1998**, *109*, 8218–8224.

(62) Bauernschmitt, R.; Ahlrichs, R. *Chem. Phys. Lett.* **1996**, *256*, 454–464.

(63) Hirata, S.; Head-Gordon, M. *Chem. Phys. Lett.* **1999**, *314*, 291–299.

(64) Hirata, S.; Head-Gordon, M. *Chem. Phys. Lett.* **1999**, *302*, 375–382.

(65) Neese, F.; Olbrich, G. *Chem. Phys. Lett.* **2002**, *362*, 170–178.

(66) Neese, F. *Inorg. Chim. Acta* **2002**, *337*, 181–192.

(67) Barone, V. *Recent Advances in Density Functional Methods*; Chong, D. P., Ed.; World Scientific: Singapore, 1996.

(68) Ouch, K.; Mashuta, M. S.; Grapperhaus, C. A. *Eur. J. Inorg. Chem.* **2012**, *2012*, 475–478.

(69) Russell, S. K.; Bowman, A. C.; Lobkovsky, E.; Wieghardt, K.; Chirik, P. J. *Eur. J. Inorg. Chem.* **2012**, *2012*, 535–545.

(70) Cowley, R. E.; Christian, G. J.; Brennessel, W. W.; Neese, F.; Holland, P. L. *Eur. J. Inorg. Chem.* **2012**, *2012*, 479–483.

(71) Patureau, F. W.; Siegler, M. A.; Spek, A. L.; Sandee, A. J.; Jugé, S.; Aziz, S.; Berkessel, A.; Reek, J. N. H. *Eur. J. Inorg. Chem.* **2012**, *2012*, 496–503.

(72) Tejel, C.; Asensio, L.; Pilar del Río, M.; de Bruin, B.; López, J. A.; Ciriano, M. A. *Eur. J. Inorg. Chem.* **2012**, *2012*, 512–519.

(73) Hindson, K.; de Bruin, B. *Eur. J. Inorg. Chem.* **2012**, *2012*, 340–342.

(74) Kreisel, K. A.; Yap, G. P. A.; Theopold, K. H. *Eur. J. Inorg. Chem.* **2012**, *2012*, 520–529.

(75) Kornecki, K. P.; Berry, J. F. *Eur. J. Inorg. Chem.* **2012**, *2012*, 562–568.

(76) Lippert, C. A.; Riener, K.; Soper, J. D. *Eur. J. Inorg. Chem.* **2012**, *2012*, 554–561.

(77) Lu, F.; Zarkesh, R. A.; Heyduk, A. F. *Eur. J. Inorg. Chem.* **2012**, *2012*, 467–470.

(78) Zeng, Q.; Messaoudani, M.; Vlček, A.; Hartl, F. *Eur. J. Inorg. Chem.* **2012**, *2012*, 471–474.

(79) Schauer, P. A.; Low, P. J. *Eur. J. Inorg. Chem.* **2012**, *2012*, 390–411.

(80) Watanabe, M.; Kashiwame, Y.; Kuwata, S.; Ikariya, T. *Eur. J. Inorg. Chem.* **2012**, *2012*, 504–511.

(81) Chan, T. L.; To, C. T.; Liao, B.-S.; Liu, S.-T.; Chan, K. S. *Eur. J. Inorg. Chem.* **2012**, *2012*, 485–489.

(82) Ringenberg, M. R.; Rauchfuss, T. B. *Eur. J. Inorg. Chem.* **2012**, *2012*, 490–495.

(83) Zhu, S.; Cui, X.; Zhang, X. P. *Eur. J. Inorg. Chem.* **2012**, *2012*, 430–434.

(84) Hohloch, S.; Braunstein, P.; Sarkar, B. *Eur. J. Inorg. Chem.* **2012**, *2012*, 546–553.

(85) Schneider, S.; Meiners, J.; Askevold, B. *Eur. J. Inorg. Chem.* **2012**, *2012*, 412–429.

(86) Sieh, D.; Schlimm, M.; Andernach, L.; Angersbach, F.; Nückel, S.; Schöffel, J.; Šušnjar, N.; Burger, P. *Eur. J. Inorg. Chem.* **2012**, *2012*, 444–462.

(87) Budzelaar, P. H. M. *Eur. J. Inorg. Chem.* **2012**, *2012*, 530–534.

(88) Caulton, K. G. *Eur. J. Inorg. Chem.* **2012**, *2012*, 435–443.

(89) Intrieri, D.; Caselli, A.; Ragaini, F.; Macchi, P.; Casati, N.; Gallo, E. *Eur. J. Inorg. Chem.* **2012**, *2012*, 569–580.

(90) Van der Vlugt, J. I. *Eur. J. Inorg. Chem.* **2012**, *2012*, 363–375.

(91) Kaim, W. *Eur. J. Inorg. Chem.* **2012**, *2012*, 343–348.

(92) Lesh, F. D.; Lord, R. L.; Heeg, M. J.; Schlegel, H. B.; Verani, C. N. *Eur. J. Inorg. Chem.* **2012**, *2012*, 463–466.

(93) Hicks, R. G. *Org. Biomol. Chem.* **2007**, *5*, 1321–1338.

(94) Pierre, J.-L. *Chem. Soc. Rev.* **2000**, *29*, 251–257.

(95) Dzik, W. I.; van der Vlugt, J. I.; Reek, J. N. H.; de Bruin, B. *Angew. Chem. Int. Ed.* **2011**, *50*, 3356–3358.

(96) Luca, O. R.; Crabtree, R. H. *Chem. Soc. Rev.* **2013**, *42*, 1440–1459.

(97) Whittaker, J. W. In *Metal Ions in Biological Systems*; Sigel, H.; Sigel, A., Eds.; Marcel Dekker: New York, 1994; p. 315.

(98) Borman, C. D.; Saysell, C. G.; Sokolowski, A.; Twitchett, M. B.; Wright, C.; Sykes, A. G. *Coord. Chem. Rev.* **1999**, *190-192*, 771–779.

(99) McPherson, M. J.; Parsons, M. R.; Spooner, R. K.; Wilmot, C. M. In *Handbook for Metalloproteins*; Messerschmidt, A.; Huber, R.; Poulos, T.; Wieghardt, K., Eds.; John Wiley & Sons, Inc., 2001; p. 1272.

(100) Whittaker, J. W. In *Advances in Protein Chemistry*; Richards, F. M.; Eisenberg, D. S.; Kuriyan, J., Eds.; Academic Press, Elsevier, 2002; p. 1.

(101) Whittaker, J. W. *Chem. Rev.* **2003**, *103*, 2347–2363.

(102) Rogers, M. *Curr. Opin. Chem. Biol.* **2003**, *7*, 189–196.

(103) Firbank, S.; Rogers, M.; Hurtado-Guerrero, R.; Dooley, D.; Halcrow, M.; Phillips, S.; Knowles, P.; McPherson, M. *Biochem. Soc. Trans.* **2003**, *31*, 506.

(104) Li, H. In *Handbook for Metalloproteins*; Messerschmidt, A.; Huber, R.; Poulos, T.; Wieghardt, K., Eds.; John Wiley & Sons, Inc., 2001; p. 267.

(105) Que, L.; Tolman, W. B. *Nature* **2008**, *455*, 333–340.

(106) Rittle, J.; Green, M. T. *Science* **2010**, *330*, 933–937.

(107) Thomas, F. In *Stable Radicals: Fundamentals and Applied Aspects of Odd-Electron Compounds*; Hicks, R. G., Ed.; John Wiley & Sons, Inc.: Chichester, 2010; p. 281.

(108) Shimazaki, Y.; Yamauchi, O. *Ind. J. Chem.* **2011**, 383.

(109) Rotthaus, O.; Jarjayes, O.; Thomas, F.; Philouze, C.; Perez Del Valle, C.; Saint-Aman, E.; Pierre, J.-L. *Chem. Eur. J.* **2006**, *12*, 2293–2302.

(110) Shimazaki, Y.; Yajima, T.; Tani, F.; Karasawa, S.; Fukui, K.; Naruta, Y.; Yamauchi, O. *J. Am. Chem. Soc.* **2007**, *129*, 2559–2568.

(111) Rotthaus, O.; Labet, V.; Philouze, C.; Jarjayes, O.; Thomas, F. *Eur. J. Inorg. Chem.* **2008**, *2008*, 4215–4224.

(112) Kochem, A.; Orio, M.; Jarjayes, O.; Neese, F.; Thomas, F. *Chem. Commun.* **2010**, *46*, 6765–6767.

(113) Dunn, T. J.; Ramogida, C. F.; Simmonds, C.; Paterson, A.; Wong, E. W. Y.; Chiang, L.; Shimazaki, Y.; Storr, T. *Inorg. Chem.* **2011**, *50*, 6746–6755.

(114) Verma, P.; Pratt, R. C.; Storr, T.; Wasinger, E. C.; Stack, T. D. P. *Proc. Natl. Acad. Sci. U. S. A.* **2011**, *108*, 18600–18605.

(115) Pierpont, C. G.; Lange, C. W. *Prog. Inorg. Chem.* **1994**, *41*, 381.

(116) Pierpont, C. G. *Inorg. Chem.* **2011**, *50*, 9766–9772.

(117) Verma, P.; Weir, J.; Mirica, L.; Stack, T. D. P. *Inorg. Chem.* **2011**, *50*, 9816–9825.

(118) Sun, X.; Chun, H.; Hildenbrand, K.; Bothe, E.; Weyhermüller, T.; Neese, F.; Wieghardt, K. *Inorg. Chem.* **2002**, *41*, 4295–4303.

(119) Smith, A. L.; Clapp, L. A.; Hardcastle, K. I.; Soper, J. D. *Polyhedron* **2010**, *29*, 164–169.

(120) Smith, A. L.; Hardcastle, K. I.; Soper, J. D. *J. Am. Chem. Soc.* **2010**, *132*, 14358–14360.

(121) Poddel'sky, A. I.; Cherkasov, V. K.; Abakumov, G. A. *Coord. Chem. Rev.* **2009**, *253*, 291–324.

(122) Chaudhuri, P.; Hess, M.; Müller, J.; Hildenbrand, K.; Bill, E.; Weyhermüller, T.; Wieghardt, K. *J. Am. Chem. Soc.* **1999**, *121*, 9599–9610.

(123) Verani, C. N.; Gallert, S.; Bill, E.; Weyhermüller, T.; Wieghardt, K.; Chaudhuri, P. *Chem. Commun.* **1999**, 1747–1748.

(124) Chun, H.; Verani, C.N.; Chaudhuri, P.; Bothe, E.; Bill, E.; Weyhermüller, T.; Wieghardt, K. *Inorg. Chem.* **2001**, *40*, 4157–4166.

(125) Herebian, D.; Ghosh, P.; Chun, H.; Bothe, E.; Weyhermüller, T.; Wieghardt, K. *Eur. J. Inorg. Chem.* **2002**, *2002*, 1957–1967.

(126) Chun, H.; Chaudhuri, P.; Weyhermüller, T.; Wieghardt, K. *Inorg. Chem.* **2002**, *41*, 790–795.

(127) Sik Min, K.; Weyhermüller, T.; Bothe, E.; Wieghardt, K. *Inorg. Chem.* **2004**, *43*, 2922–2931.

(128) Sik Min, K.; Weyhermüller, T.; Wieghardt, K. *Dalton Trans.* **2003**, 1126–1132.

(129) Ray, K.; Begum, A.; Weyhermüller, T.; Piligkos, S.; van Slageren, J.; Neese, F.; Wieghardt, K. *J. Am. Chem. Soc.* **2005**, *127*, 4403–4415.

(130) Sproules, S.; Kapre, R. R.; Roy, N.; Weyhermüller, T.; Wieghardt, K. *Inorg. Chim. Acta* **2010**, *363*, 2702–2714.

(131) Khusniyarov, M. M.; Weyhermüller, T.; Bill, E.; Wieghardt, K. *J. Am. Chem. Soc.* **2009**, *131*, 1208–1221.

(132) Muresan, N.; Chlopek, K.; Weyhermüller, T.; Neese, F.; Wieghardt, K. *Inorg. Chem.* **2007**, *46*, 5327–5337.

(133) De Bruin, B.; Bill, E.; Bothe, E.; Weyhermüller, T.; Wieghardt, K. *Inorg. Chem.* **2000**, *39*, 2936–2947.

(134) Bowman, A. C.; Milsmann, C.; Atienza, C. C. H.; Lobkovsky, E.; Wieghardt, K.; Chirik, P. J. *J. Am. Chem. Soc.* **2010**, *132*, 1676–1684.

(135) Darmon, J. M.; Stieber, S. C. E.; Sylvester, K. T.; Fernández, I.; Lobkovsky, E.; Semproni, S. P.; Bill, E.; Wieghardt, K.; DeBeer, S.; Chirik, P. J. *J. Am. Chem. Soc.* **2012**, *134*, 17125–17137.

(136) Bill, E.; Bothe, E.; Chaudhuri, P.; Chlopek, K.; Herebian, D.; Kokatam, S.; Ray, K.; Weyhermüller, T.; Neese, F.; Wieghardt, K. *Chem. Eur. J.* **2004**, *11*, 204–224.

(137) Storr, T.; Verma, P.; Pratt, R. C.; Wasinger, E. C.; Shimazaki, Y.; Stack, T. D. P. *J. Am. Chem. Soc.* **2008**, *130*, 15448–15459.

(138) Asami, K.; Tsukidate, K.; Iwatsuki, S.; Tani, F.; Karasawa, S.; Chiang, L.; Storr, T.; Thomas, F.; Shimazaki, Y. *Inorg. Chem.* **2012**, *51*, 12450–12461.

(139) De Bellefeuille, D.; Askari, M. S.; Lassalle-Kaiser, B.; Journaux, Y.; Aukauloo, A.; Orio, M.; Thomas, F.; Ottenwaelder, X. *Inorg. Chem.* **2012**, *51*, 12796–12804.

(140) Cervera, B.; Sanz, J. L.; Ibáñez, M. J.; Vila, G.; LLoret, F.; Julve, M.; Ruiz, R.; Ottenwaelder, X.; Aukauloo, A.; Poussereau, S.; Journaux, Y.; Muñoz, M. C. *J. Chem. Soc. Dalton Trans.* **1998**, 781–790.

(141) Barth, T.; Neugebauer, F. A. *J. Org. Chem.* **1995**, *60*, 5401–5406.

(142) Michaelis, L.; Schubert, M. P.; Granick, S. *J. Am. Chem. Soc.* **1939**, *61*, 1981–1992.

(143) Latta, B. M.; Taft, R. W. *J. Am. Chem. Soc.* **1967**, *89*, 5172–5178.

(144) Addison, A. W.; Yokoi, H. *Inorg. Chem.* **1977**, *16*, 1341–1349.

(145) Sakaguchi, U.; Addison, A. W. *J. Chem. Soc. Dalton Trans.* **1979**, 600.

(146) Klement, R.; Stock, F.; Elias, H.; Paulus, H.; Pelikán, P.; Valko, M.; Mazúr, M. *Polyhedron* **1999**, *18*, 3617–3628.

(147) Hess, C. R.; Weyhermüller, T.; Bill, E.; Wieghardt, K. *Angew. Chem. Int. Ed.* **2009**, *48*, 3703–3706.

(148) Asami, K.; Takashina, A.; Kobayashi, M.; Iwatsuki, S.; Yajima, T.; Gastel, M. Van; Tani, F.; Kohzuma, T.; Thomas, F.; Shimazaki, Y. *Dalton Trans.* **2014**, 2283–2293.

(149) Neese, F. *Wiley Interdiscip. Rev. Comput. Mol. Sci.* **2012**, *2*, 73–78.

(150) Perdew, J. P. *Phys. Rev. B* **1986**, *33*, 8822–8824.

(151) Perdew, J. P. *Phys. Rev. B* **1986**, *34*, 7406.

(152) Scha¨fer, A.; Huber, C.; Ahlrichs, R. *J. Chem. Phys.* **1994**, *100*, 5829.

(153) Becke, A. D. *J. Chem. Phys.* **1993**, *98*, 1372.

(154) Neese, F. *J. Chem. Phys.* **2001**, *115*, 11080.

(155) Koseki, S.; Schmidt, M. W.; Gordon, M. S. *J. Phys. Chem.* **1992**, *96*, 10768–10772.

(156) Koseki, S.; Gordon, M. S.; Schmidt, M. W.; Matsunaga, N. *J. Phys. Chem.* **1995**, *99*, 12764–12772.

(157) Neese, F. *J. Chem. Phys.* **2003**, *118*, 3939.

(158) Pantazis, D. A.; Chen, X.-Y.; Landis, C. R.; Neese, F. *J. Chem. Theory Comput.* **2008**, *4*, 908–919.

(159) Pantazis, D. A.; Neese, F. *J. Chem. Theory Comput.* **2009**, *5*, 2229–2238.

(160) Noodleman, L.; Case, D. A. *Adv. Inorg. Chem.* **1992**, *38*, 423.

(161) Noodleman, L.; Davidson, E. R. *Chem. Phys.* **1986**, *109*, 131–143.

(162) Noodleman, L. *J. Chem. Phys.* **1981**, *74*, 5737.

(163) Soda, T.; Kitagawa, Y.; Onishi, T.; Takano, Y.; Shigeta, Y.; Nagao, H.; Yoshioka, Y.; Yamaguchi, K. *Chem. Phys. Lett.* **2000**, *319*, 223–230.

(164) Yamaguchi, K.; Takahara, Y.; Fueno, T. *Applied Quantum Chemistry V*; Smith, V. H., Ed.; Reidel: Dordrecht, 1986.

(165) Heisenberg, W. *Zeitschrift für Phys.* **1928**, *49*, 619–636.

(166) Heisenberg, W. *Zeitschrift für Phys.* **1926**, *38*, 411–426.

(167) Dirac, P. a. M. *Proc. R. Soc. A Math. Phys. Eng. Sci.* **1929**, *123*, 714–733.

(168) Van Vleck, J. H. *The Theory of Electronic and Magnetic Susceptibilities*; Oxford University: London, 1932.

(169) Ganyushin, D.; Neese, F. *J. Chem. Phys.* **2006**, *125*, 24103.

(170) Peretti, K. L.; Ajiro, H.; Cohen, C. T.; Lobkovsky, E. B.; Coates, G. W. *J. Am. Chem. Soc.* **2005**, *127*, 11566–11567.

(171) Venkatasubbaiah, K.; Feng, Y.; Arrowood, T.; Nickias, P.; Jones, C. W. *ChemCatChem* **2013**, *5*, 201–209.

(172) Wöltinger, J.; J, B.; Zsigmond, Á. *Chem. Eur. J.* **1999**, 1460–1467.

(173) Atienza, C. C. H.; Milsmann, C.; Semproni, S. P.; Turner, Z. R.; Chirik, P. J. *Inorg. Chem.* **2013**, *52*, 5403–5417.

(174) Manuel, T. D.; Rohde, J.-U. *J. Am. Chem. Soc.* **2009**, *131*, 15582–15583.

(175) Collins, T. J.; Ozaki, S.; Richmond, T. G. *J. Chem. Soc. Chem. Commun.* **1987**, 803–804.

(176) Koola, D.; Kochi, K. *J. Org. Chem.* **1987**, *52*, 4545–4553.

(177) Mulyana, Y.; Alley, K. G.; Davies, K. M.; Abrahams, B. F.; Moubaraki, B.; Murray, K. S.; Boskovic, C. *Dalton Trans*. **2014**, *43*, 2499–2511.

(178) Balch, A. L.; Mazzanti, M.; Olmstead, M. M. *Inorg. Chem*. **1993**, *32*, 4737–4744.

(179) Zats, G. M.; Arora, H.; Lavi, R.; Yufit, D.; Benisvy, L. *Dalton Trans*. **2011**, *40*, 10889–10896.

(180) Iranmanesh, H.; Behzad, M.; Bruno, G.; Rudbari, H. A.; Nazari, H.; Mohammadi, A.; Taheri, O. *Inorg. Chim. Acta* **2013**, *395*, 81–88.

(181) Srinivasan, S.; Annaraj, J.; Athappan, P. *J. Inorg. Biochem*. **2005**, *99*, 876–882.

(182) Silva, T. F. S.; Martins, L. M. D. R. S.; Guedes da Silva, M. F. C.; Fernandes, A. R.; Silva, A.; Borralho, P. M.; Santos, S.; Rodrigues, C. M. P.; Pombeiro, A. J. L. *Dalton Trans*. **2012**, *41*, 12888–12897.

(183) Jiménez, C. a; Belmar, J. B.; Alderete, J.; Delgado, F. S.; López-Rodríguez, M.; Peña, O.; Julve, M.; Ruiz-Perez, C. *Dalton Trans*. **2007**, 2135–2144.

(184) Anson, F. C.; Collins, T. J.; Coots, R. J.; Gipson, S. L.; Richmond, T. G. *J. Am. Chem. Soc*. **1984**, *106*, 5037–5038.

(185) Zhang, Z.; Suwabe, T.; Ishikawa, M.; Funahashi, Y.; Inomata, T.; Ozawa, T.; Masuda, H. *Dalton Trans*. **2013**, *42*, 4470–4478.

(186) Shimakoshi, H.; Hirose, S.; Ohba, M.; Shiga, T.; Okawa, H.; Hisaeda, Y. *Bull. Chem. Soc. Jpn*. **2005**, *78*, 1040–1046.

(187) Kochem, A.; Kanso, H.; Baptiste, B.; Arora, H.; Philouze, C.; Jarjayes, O.; Vezin, H.; Luneau, D.; Orio, M.; Thomas, F. *Inorg. Chem*. **2012**, *51*, 10557–10571.

(188) Kurahashi, T.; Fujii, H. *Inorg. Chem*. **2013**, *52*, 3908–3919.

(189) Kemper, S.; Hroba, P.; Kaupp, M.; Schlo, N. E. *J. Am. Chem. Soc*. **2009**, *131*, 4172–4173.

(190) Skoog, D. A.; Holler, J. F.; Crouch, S. R. In *Principles of Instrumental Analysis*; Thomson Brooks/Cole: Belmont, 2007; pp. 716–742.

(191) Corvaja, C. In *Electron Paramagnetic Resonance*; John Wiley & Sons, Inc., 2009; pp. 1–36.

Appendix A

Electrochemistry

There are two techniques of electrochemistry used to provide information about the redox processes taking place: cyclic voltammetry (CV) and electrolysis. All electrochemical experiments are done in an electrochemical cell. The cell contains 3 electrodes: working, reference and auxiliary. The reference electrode has a fixed constant potential. The working electrode's potential with respect to the reference electrode is varied with time, the auxiliary electrode simply conducts electricity from the source through the solution to the working electrode[190]. Since oxygen is redox-active, dissolved oxygen must be purged from the cell; this can be done by degassing with an inert gas like argon. A supporting electrolyte must also be added to insure maximal conductivity in the solution. Lastly, an internal reference is often used to report redox potentials. Often in inorganic chemistry the ferrocenium-ferrocene redox couple (Fc^+/Fc) is used as an internal reference.

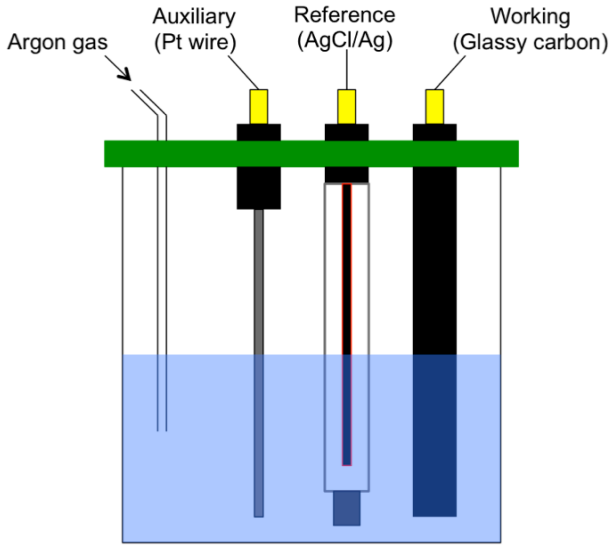

Figure A-1. Schematic view of an electrochemical cell.

The principle of cyclic voltammetry is to vary the potential of the working electrode with respect to time and record changes in current. The potential is varied from minima to maxima in a linear fashion. The electrochemical process that occurs in the vicinity of the electrode is what is recorded. It is important for the solution to be unstirred in order to maintain oxidation only at the vicinity of the electrode, the redox processes are thus diffusion-controlled. The shape of the CV curve provides information about electrochemical processes of the analyte. The classic duck-shape indicates a reversible redox process (oxidation and reduction). The redox potential (or the Nernst potential) can be found by taking the average of the oxidation and reduction voltages and is displayed as $E_{1/2}$.

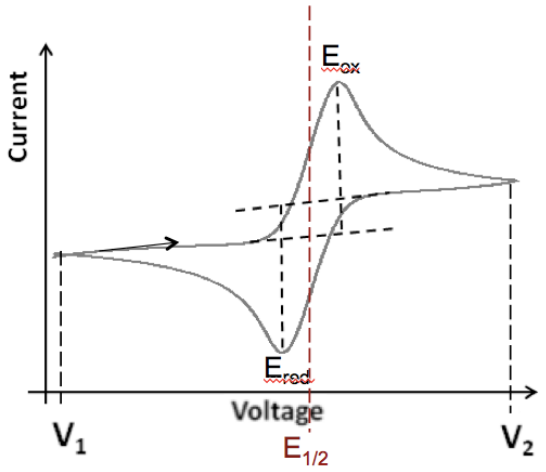

Figure A-2. Typical shape of a reversible redox process in a CV curve.

Following the arrow, the voltage of the cell is low and begins to increase to the maxima ($V_1 \rightarrow V_2$). As the potential increases, in the vicinity of the electrode, oxidation begins to occur until most is oxidized (E_{ox}). Potential still increases due to diffusion but there are less oxidations taking place. Once the potential has reached the maxima (V_2), the potential is reversed and eventually, in the vicinity of the electrode, reduction of the oxidized species in the vicinity of the electrode begins to occur. When E_{red} is reached most of the species are reduced. In a typical experiment, this process is repeated several times to ensure the shape remains the same, indicating no decomposition and supporting the reversibility of the redox process. The redox potential can be found by taking the average of the oxidation and reduction potentials.

The principle of an electrolysis experiment is similar to that of CV, in fact, often a CV is done after electrolysis. The reasoning behind this experiment is two-fold: first to determine whether the oxidized products are stable and second to verify how many electrons were transferred during each redox event. Once the redox potential is found (by CV for instance), the voltage is maintained just above that of the redox potential. The

current is monitored until there is no more exchange of electrons (i.e. everything is oxidized). From the integration of current passed, the total charge can be found and using Faraday's constant the moles of electrons transferred can be calculated. Divide by the moles of analyte and the number of electrons per molecule in the redox event can be found. Stability is inferred by repeating a CV to the oxidized solution. Since the voltage was maintained for a long time, any decomposition would have already occurred and the starting material could not be reformed. If the original CV and the CV of the oxidized solution match up, there was no decomposition or reactions and one can infer that the oxidized products are stable.

Electron Paramagnetic Resonance Spectroscopy

Electron paramagnetic resonance (EPR) spectroscopy is a method to study species containing unpaired electrons. The principle is similar to that of nuclear magnetic resonance (NMR) spectroscopy, which studies magnetically equivalent nuclei rather than unpaired electrons. A great advantage of EPR is that only unpaired electrons give rise to a signal, therefore the experiment has a very high specificity and virtually no interactions with spectator compounds or solvent. The magnetic moment is related to the electron spin by the following relationship:

$$\mu_e = g\mu_B S \qquad \text{(equation A-1)}$$

where μ_B is the Bohr magneton (-9.27410 x 10^{-24} JT^{-1}) and g is a new term called the g-factor or the Landé factor.[191] When an external magnetic field (B_0) is applied to an electron with spin ½ , the energy of the spin states are separated and can be calculated by:

$$E_{\pm} = \pm\left(\frac{1}{2}\right) g \mid \mu_B \mid B_0 \qquad \text{(equation A-2)}$$

where the positive value corresponds to the higher energy state and negative value to the lower energy state; the difference in energy can be calculated by:

$$h\upsilon = E_{\alpha} - E_{\beta} = g \mid \mu_B \mid B_0 \qquad \text{(equation A-3)}$$

This technique relies on the Zeeman effect (Figure A-3), which states that in the presence of a magnetic field a spectral line is split into components of higher energy (α) and of lower energy (β); electron spins and magnetic moments will align themselves parallel or anti-parallel. ν is the frequency of electromagnetic radiation. In NMR experiments, the working frequency is in the Megahertz range. In a typical X-band EPR experiment the magnetic field is 0.34 T, if $g = g_e = 2.0023$, ν gives a radiation frequency of 9.3 Gigahertz. Due to electron-nuclear mass differences, the magnetic moment of an electron is much higher than that of a nucleus, this means that the frequency must be larger to achieve this excitation. From the Boltzmann distribution, we know that there is a larger population in a lower energy state at low temperature, thus there is a net absorption of energy when the electron migrates to the higher energy level. This absorbance is recorded by the instrument and plotted as the first derivative (Figure A-4).

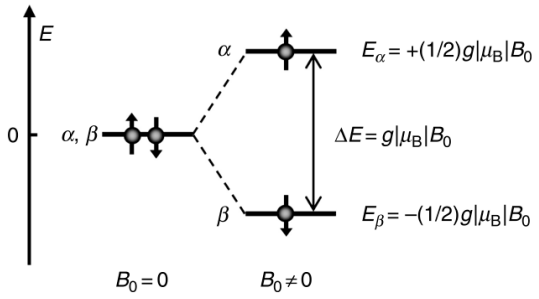

Figure A-3. The Zeeman effect.[191]

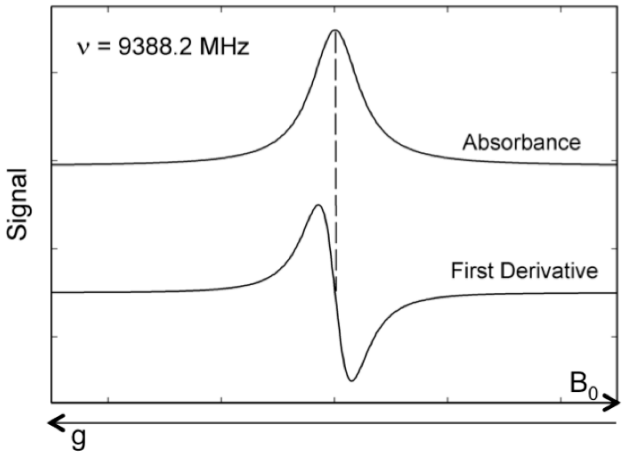

Figure A-4. EPR spectrum.

The g-factor gives information about the paramagnetic electron's location. The electron's spin generates a magnetic field that allows itself to be aligned with the applied field. However, the electron orbits a nucleus and this can generate its own magnetic field. The relationship between the electron spin and its orbit (spin-orbit coupling) can thus affect the g-factor. Therefore, an unpaired electron is sensitive to local magnetic fields created by the neighbouring electrons in its immediate environment. Any deviation from the g-factor of a free electron is indicative of the position of the electron in the compound.

Table A-1. The impact of SOC on the "g" factor

Free electron	~ 0 SOC	$g_e = 2.0023$
Electron on organic moiety	Very little if any SOC	$g \sim g_e$ (ex. 2.004)
Electron on metals	Significant SOC	$g \neq g_e$ (ex. 1.7 – 9.0)

Since the spin-orbit interaction is directly related to the orbital motion of the electron, it is highly dependant on the orientation of the applied magnetic field to the molecule and is therefore anisotropic.[191] This anisotropy is manifested in the overall shape of the plot derived from the absorption. In liquid solutions, that tumble freely, the anisotropy averages to zero and an isotropic signal is observed. However, in crystalline, powder and frozen samples, other features become more apparent. Axial anisotropy occurs when two of the planes are either parallel or perpendicular to the magnetic field vector. As the experiment uses a continuous wave approach, as the field moves from parallel to perpendicular or vice-versa, the absorption increases on a particular value of g and two g factors are revealed ($g_{//}$ and $g_{\perp}$).

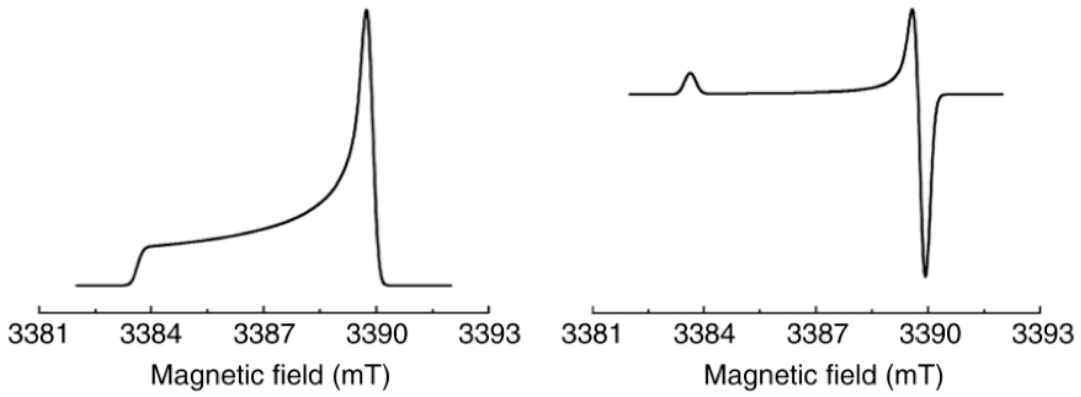

Figure A-5. EPR absorption and first derivative of a sample exhibiting axial anisotropy.[191]

The last form is due to rhombic anisotropy. Where axial maintained symmetry in two planes, rhombic has no symmetry at all and thus induces a different value of g for each plane (g_1, g_2 and g_3).

In the presence of nearby nuclear spins, the electrons experience an additional magnetic field generated by the nuclear magnetic moments. Hyperfine coupling is the interaction between the unpaired electron with nearby nuclear spins. This is somewhat analogous to J-coupling in NMR. This interaction leads to additional allowed energy states, which in turn will cause multi-lined spectra, in the same way a proton signal is split in an NMR experiment. The number of lines is given by MI+1 where M is the number of equivalent nuclei and I is their spin.

UV-vis NIR Spectroscopy / TD-DFT modelling

Often it is interesting to study the UV-vis-NIR transitions of complexes as a comparison with known values. Unfortunately, for novel compounds there is nothing to compare these results to. UV-vis-NIR experimental results were compared with predicted transitions. Using Time-Dependent Density Functional Theory (TD-DFT), electronic transitions of the complexes could be calculated and compared to the experimental results as a way of determining clues about their electronic structure. In fact, TD-DFT was also used to predict the EPR spectra. TD-DFT is an extension of DFT that allows for features like excitation energies and frequency-dependent response properties of molecules (i.e. UV-vis-NIR transitions and EPR spectra). The reason the span of the electromagnetic spectrum is so wide (UV-vis-NIR) is that radicals often exhibit transitions in the near-infrared region.

Appendix B

Electrochemistry

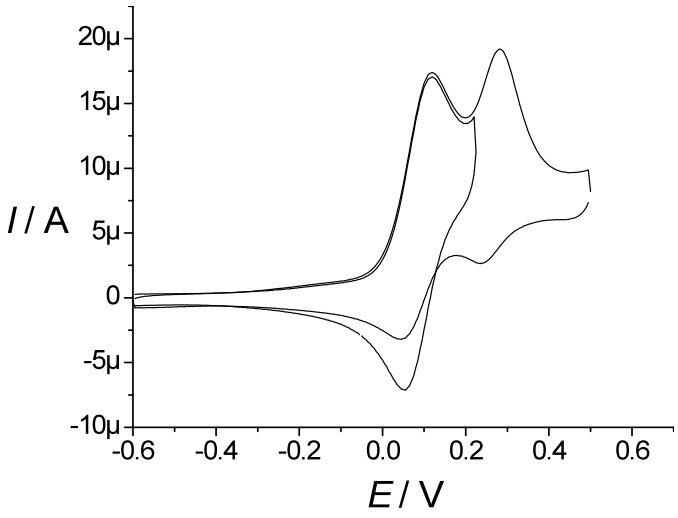

Figure B-1. Cyclovoltamograms of a 1 mM CH_2Cl_2 solution (containing 0.1 M nBu$_4$NClO$_4$) of **5** at a carbon working electrode. T = 298 K; Scan rate = 0.1 V/s; the potentials are given relative to the Fc^+/Fc reference.

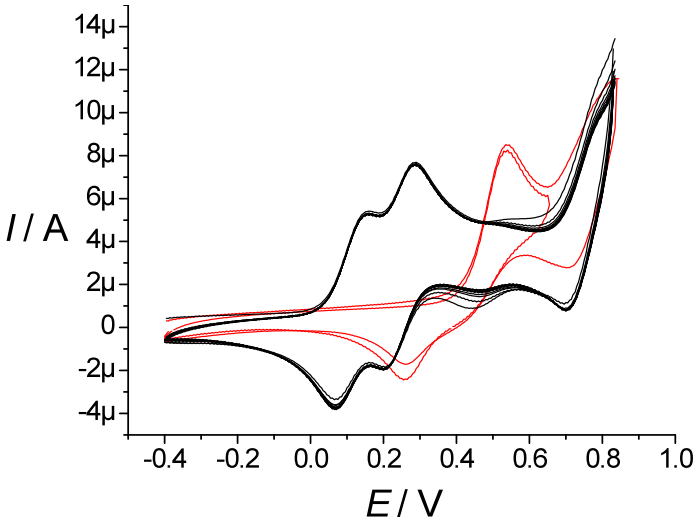

Figure B-2. Cyclovoltamograms of 0.5 mM CH_2Cl_2 solutions (containing 0.1 M nBu$_4$NClO$_4$) of: **1** (black) and *in situ* generated **1H**$^+$ (red). T = 298 K; Scan rate = 0.1 V/s; Working electrode: Platinum disc; The potentials are given relative to the Fc^+/Fc reference.

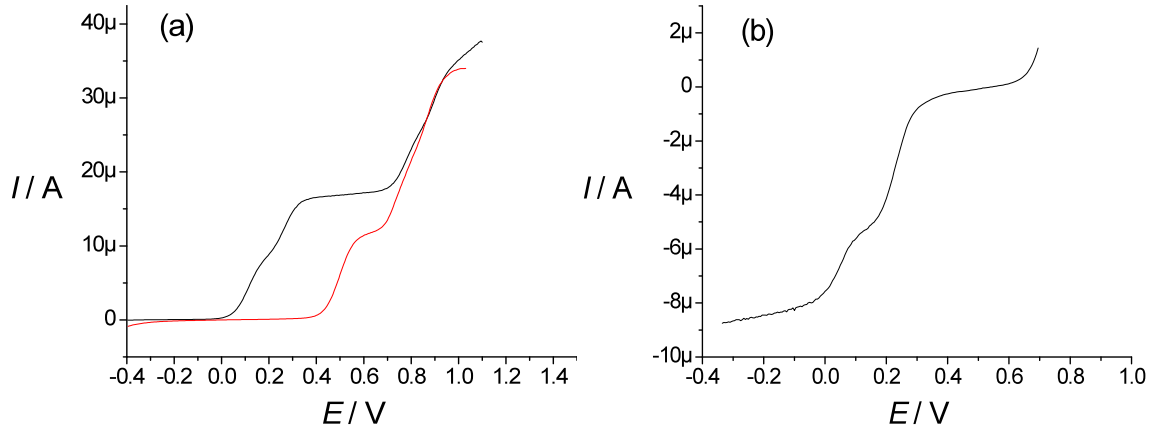

Figure B-3. Rotating Disc Electrode Voltammetry of 0.5 mM CH_2Cl_2 solutions (containing 0.1 M nBu$_4$NClO$_4$) of: (a) **1** (black) and *in situ* generated [**1H**]$^+$ (red); (b) [**1H**]$^+$ after exhaustive electrolysis at +0.6 V (coulometry indicates two electrons removed). T = 298 K (a) and 233 K (b); Scan rate = 0.01 V/s; Working electrode: Platinum wire; All potentials are given relative to the Fc^+/Fc reference.

EPR

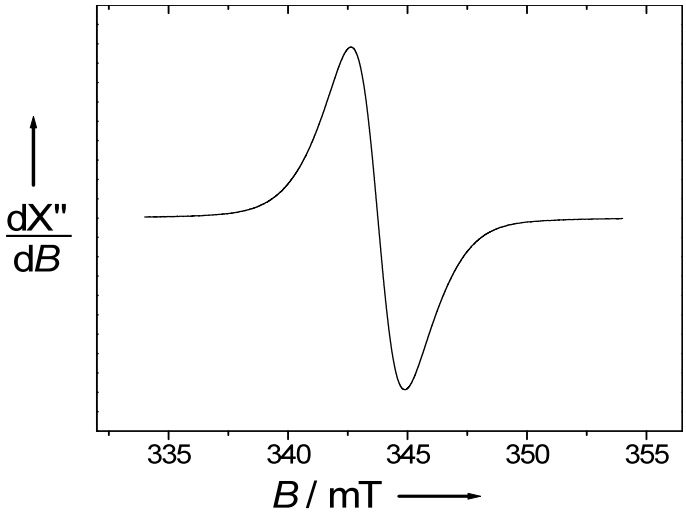

Figure B-4. X-band EPR spectrum of a 1 mM CH_2Cl_2 (+ 0.1 M nBu$_4$NClO$_4$) solution of the electrochemically generated **1**$^+$. T = 25 K, Microwave power: 2 mW, Microwave Freq.: 9.63 GHz, Mod. Amp.: 0.1 mT, Mod. Freq.: 100 KHz.

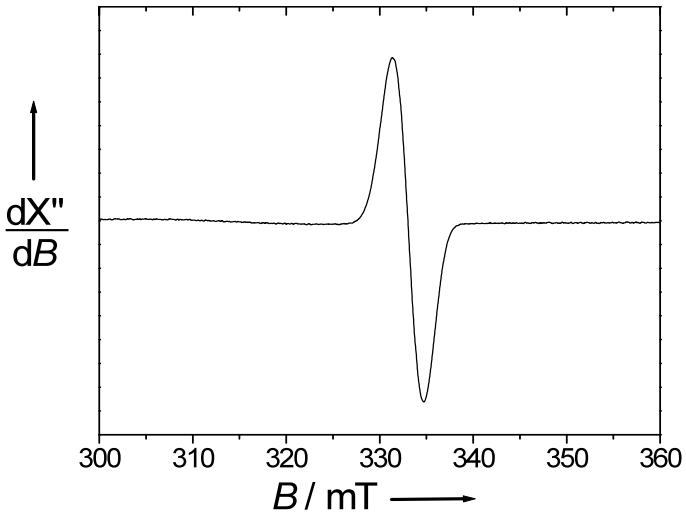

Figure B-5. X-band EPR spectrum of a 0.25 mM CH_2Cl_2:CH_3OH (3:1) (+ 0.025 M nBu$_4$NClO$_4$) solution of the electrochemically generated **1**$^+$. T = 25 K, Microwave power: 5 mW, Microwave Freq.: 9.33 GHz, Mod. Amp.: 0.2 mT, Mod. Freq.: 100 KHz.

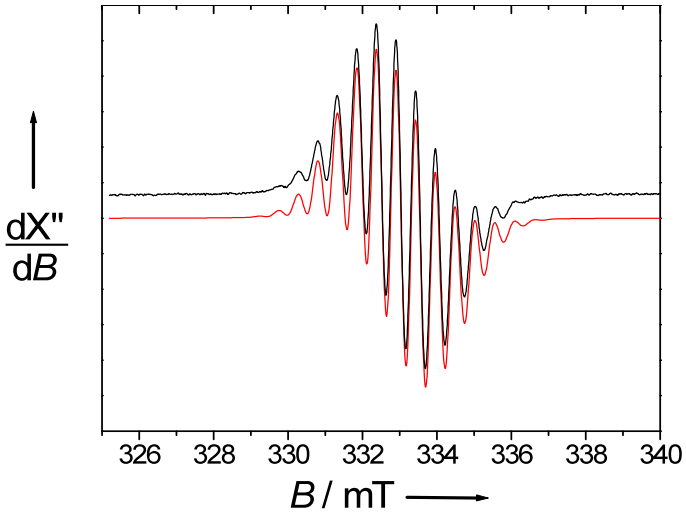

Figure B-6. X-band EPR spectrum after electrolysis (one-electron removed) of [**1H**]$^{+}$ in CH_2Cl_2. Black lines: Experimental spectrum, Red lines: Simulation using the following isotropic hyperfine coupling (HFC) constants: A_H = 14.0 MHz for 6 equivalent ^{1}H nuclei, A_H = 16.7 MHz for 6 equivalent ^{1}H nuclei and A_N = 12.8 MHz for 2 equivalent ^{14}N nuclei. T = 293 K, Microwave power: 4 mW, Microwave Freq.: 9.33 GHz, Mod. Amp.: 0.05 mT, Mod. Freq.: 100 KHz.

UV-vis-NIR

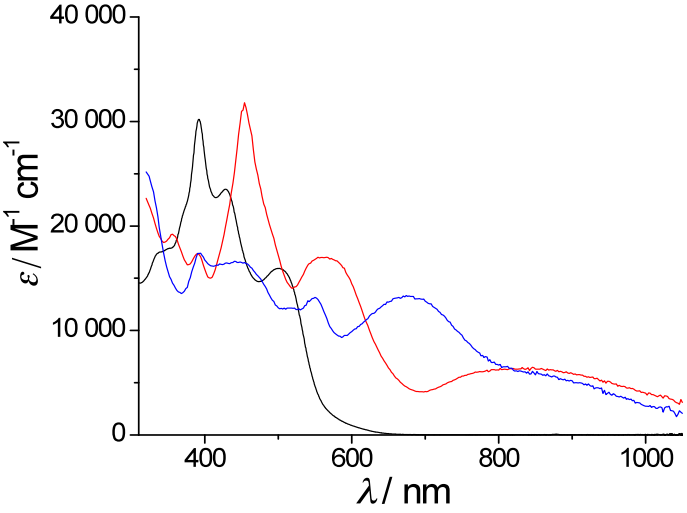

Figure B-7. UV-vis spectra of **1** (black) and the electrogenerated **1**$^{+}$ (red) and **1**$^{2+}$ (blue) in CH_2Cl_2 containing 0.01 M nBu$_4$NClO$_4$. l = 1.000 cm, T = 243 K.

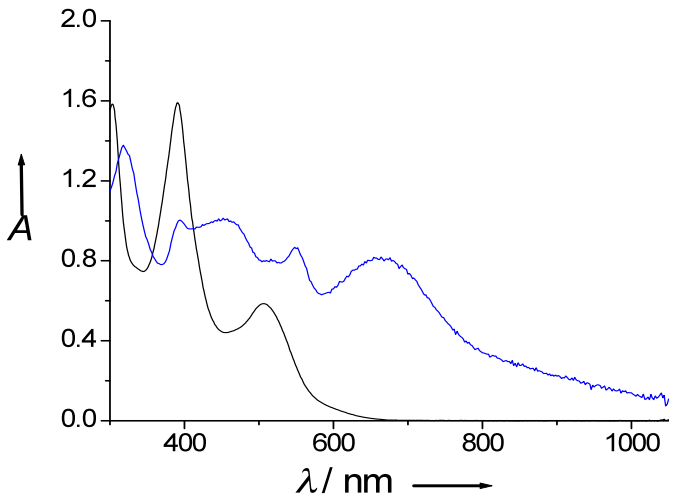

Figure B-8. UV-vis spectra of [**1H**]$^+$ before (black) and after (blue) electrolysis at 0.80 V in CH_2Cl_2 containing 0.1 M nBu$_4$NClO$_4$ at -30°. The total charge passed corresponds to two electrons. Black spectrum: 0.55 mM of [**1H**]$^+$, T = 298 K, l = 1.000 mm; Blue spectrum: 0.052 mM of oxidized species, T = 243 K, l = 1.000 cm.

DFT calculations

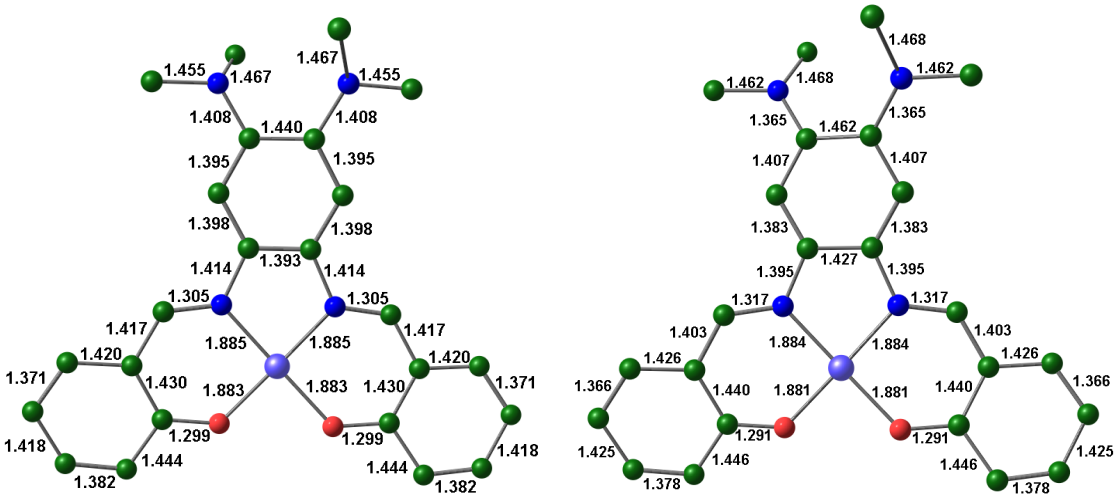

Figure B-9. Computed metrical parameters in **1** and **1**$^+$. Hydrogens and *t*Bu groups removed for clarity.

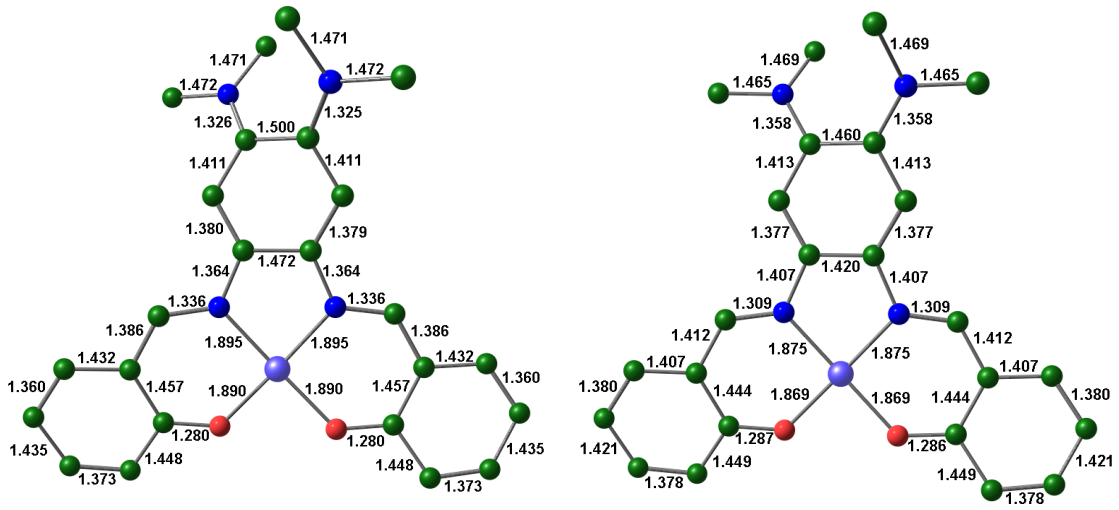

Figure B-10. Computed metrical parameters in $^{1}\mathbf{1}^{2+}$ (left) and $^{3}\mathbf{1}^{2+}$ (right). Hydrogens and *t*Bu groups removed for clarity.

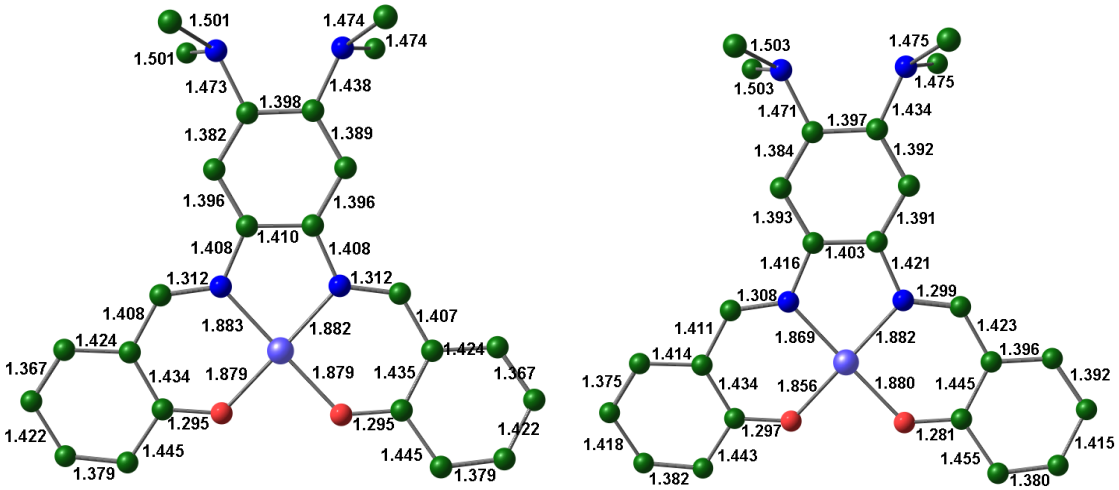

Figure B-11. Computed metrical parameters in $[\mathbf{1H}]^{+}$ and putative radical species $[\mathbf{1H}]^{2+}$. Hydrogens and *t*Bu groups removed for clarity.

Table B-1. Selected experimental and calculated bond lengths (Å) for $\mathbf{1H^+}$ and $\mathbf{1H^{2+}}$.[a]

Bond	$\mathbf{1H^+}$ (exp)	$\mathbf{1H^+}$(calcd)	$\mathbf{1H^{2+}}$ (calcd)
nature	closed shell	closed shell	radical
Ni-O	1.862	1.879	1.856
Ni-O'	1.852	1.879	1.880
Ni-N1	1.851	1.883	1.869
Ni-N1'	1.864	1.882	1.882
C1-O	1.296 - 1.302[b]	1.295	1.297 - 1.281[c]
C1-C2	1.452 - 1.440[b]	1.445	1.443 - 1.455[c]
C2-C3	1.376 - 1.377[b]	1.379	1.382 - 1.380[c]
C3-C4	1.422 - 1.413[b]	1.422	1.418 - 1.415[c]
C4-C5	1.362 - 1.373[b]	1.367	1.375 - 1.392[c]
C5-C6	1.425 - 1.412[b]	1.424	1.414 - 1.396[c]
C1-C6	1.420 - 1.430[b]	1.434	1.434 - 1.445[c]
C6-C7	1.409 - 1.405[b]	1.407 - 1.408[d]	1.411 - 1.423[c]
C7-N1	1.308 - 1.307[b]	1.312	1.308 - 1.299[c]
N1-C8	1.419 - 1.418[b]	1.408	1.416 - 1.421[c,d]
C8-C9	1.388 - 1.389[b]	1.396	1.393 - 1.391[c,d]
C9-C10	1.364 - 1.390[b]	1.382 - 1.389[d]	1.384 - 1.392[c,d]
C10-C10'	1.390	1.398	1.397
C8-C8'	1.397	1.410	1.403
C10-N3	1.474 - 1.434[b]	1.473- 1.438[d]	1.471 - 1.434[d]

[a] See scheme for atom numbering used. [b] The values refer to the two unequivalent sides of the molecule (regular labels and primed labels) due to the asymmetry created by the SbF_6^- anion in the crystal structure. [c] The second value refers to the opposite unequivalent rings due to the mixed-valence character of the phenolate-phenoxyl moiety. [d] The second value refers to the opposite unequivalent ring due to the selective protonation on one of the NMe_2 substituents.

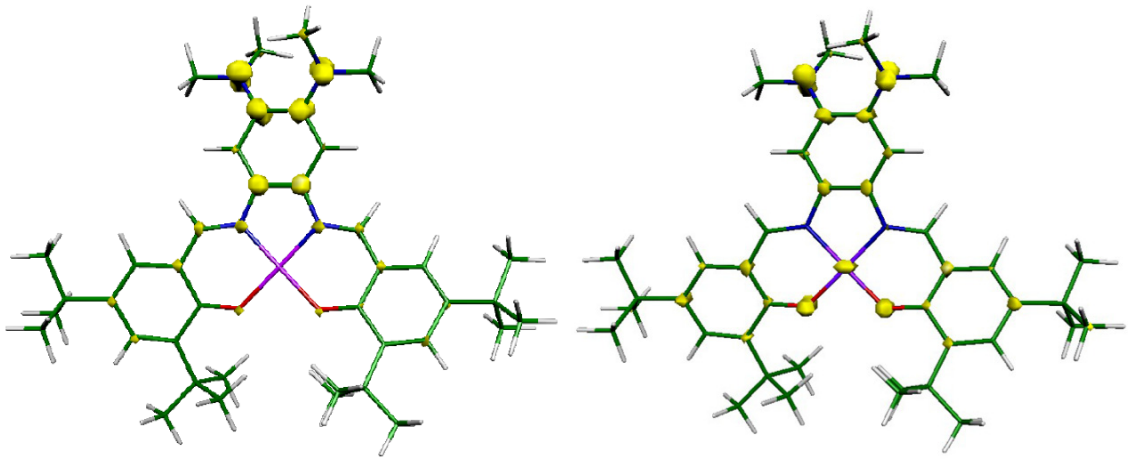

Figure B-12. Spin density plots of $\mathbf{1^+}$ (left) and triplet $\mathbf{1^{2+}}$ (right).

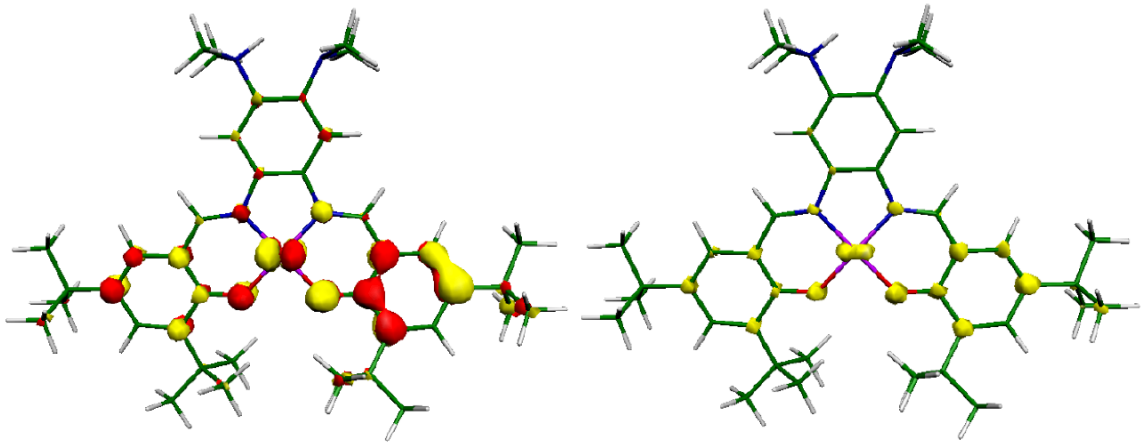

Figure B-13. Localized SOMO (left) and spin density plot (right) for the putative radical species $[\mathbf{1H}]^{2+}$.

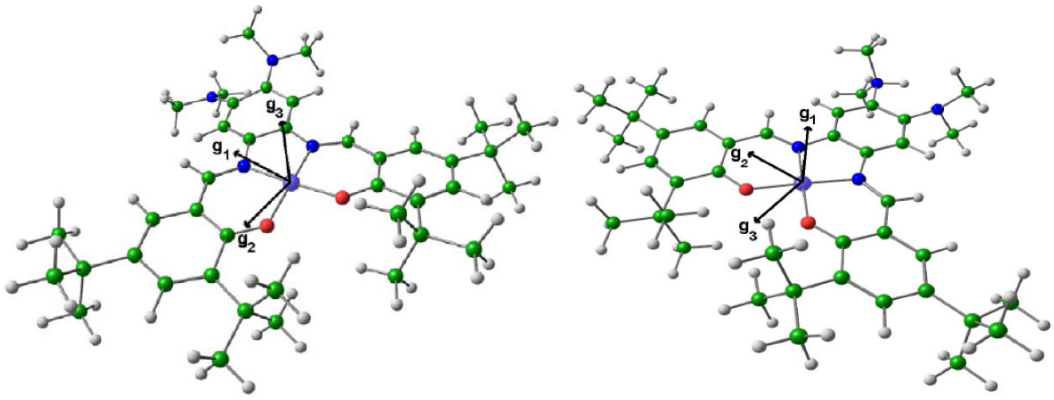

Figure B-14. g-tensor orientation for $\mathbf{1}^{+}$ (left) and the putative radical species $[\mathbf{1H}]^{2+}$ (right).

Appendix C

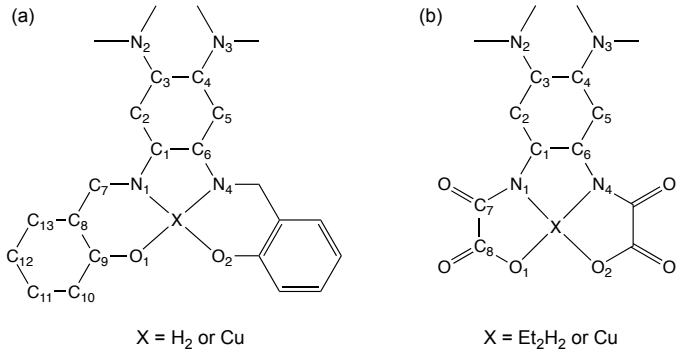

Table C-1. Selected calculated bond lengths for $\mathbf{H_2L^1}$, $\mathbf{(H_2L^1)^+}$, **1**, triplet $\mathbf{1^+}$ and doublet $\mathbf{1^{2+}}$.

Bond	$\mathbf{H_2L^1}$	$\mathbf{(H_2L^1)^+}$	**1**	$\mathbf{1^+}$	$\mathbf{1^{2+}}$
Cu-O1	-	-	1.938	1.939	1.943
Cu-N1	-	-	1.978	1.975	1.973
C9-O1	1.349	1.346	1.298	1.289	1.278
C9-C10	1.415	1.415	1.444	1.446	1.449
C10-C11	1.393	1.391	1.382	1.377	1.372
C11-C12	1.408	1.411	1.418	1.425	1.434
C12-C13	1.382	1.379	1.371	1.366	1.360
C13-C8	1.406	1.410	1.421	1.427	1.433
C9-C8	1.415	1.418	1.435	1.445	1.462
C8-C7	1.449	1.438	1.424	1.408	1.390
C7-N1	1.289	1.296	1.302	1.315	1.335
N1-C1	1.405	1.386	1.411	1.391	1.360
C1-C2	1.401	1.384	1.399	1.386	1.382
C2-C3	1.396	1.410	1.394	1.405	1.410
C3-C4	1.434	1.457	1.439	1.461	1.498
C4-C5	1.395	1.410	1.394	1.405	1.410
C5-C6	1.402	1.385	1.399	1.386	1.382
C6-C1	1.406	1.440	1.403	1.439	1.484
C3-N2	1.409	1.363	1.407	1.365	1.326

Table C-2. Selected calculated bond lengths for $Et_2H_2\mathbf{L}^2$, $(Et_2H_2\mathbf{L}^2)^+$, $\mathbf{2}^{2-}$ and triplet $\mathbf{2}^-$.

Bond	$Et_2H_2\mathbf{L}^2$	$(Et_2H_2\mathbf{L}^2)^+$	$\mathbf{2}^{2-}$	$\mathbf{2}^-$
Cu-O1	-		1.992	1.979
Cu-N1	-		1.940	1.947
C8-O1	1.214	1.214	1.294	1.293
C8-C7	1554	1.557	1.573	1.573
C7-N1	1.352	1.365	1.332	1.351
N1-C1	1.414	1.396	1.398	1.368
C1-C2	1.394	1.377	1.396	1.388
C2-C3	1.397	1.411	1.401	1.403
C3-C4	1.432	1.451	1.422	1.460
C4-C5	1.397	1.411	1.401	1.404
C5-C6	1.393	1.374	1.396	1.389
C6-C1	1.399	1.433	1.419	1.456
C4-N3	1.408	1.362	1.424	1.375

Table C-3. Spin Hamiltonian parameters for the oxidized proligands.[a]

		Calculated						Experimental		
	S	g_1	g_2	g_3	g_{iso}	$\lvert A_N \rvert$	$\lvert A_H \rvert$	g_{iso}	$\lvert A_N \rvert$	$\lvert A_H \rvert$
$(H_2L^1)^+$	1/2	2.0027	2.0030	2.0039	2.0032	13.7	16.6	2.003	12.8	17.8
$(Et_2H_2L^2)^+$	1/2	2.0026	2.0033	2.0042	2.0034	15.4	19.6	2.003	15.4	19.6

[a] Hyperfine constants in MHz. A_N for 2 equivalent ^{14}N. A_H for 12 equivalent ^1H.

Figures

Color scheme: Cu: orange, O: red; N: dark blue; C: green; H: white.

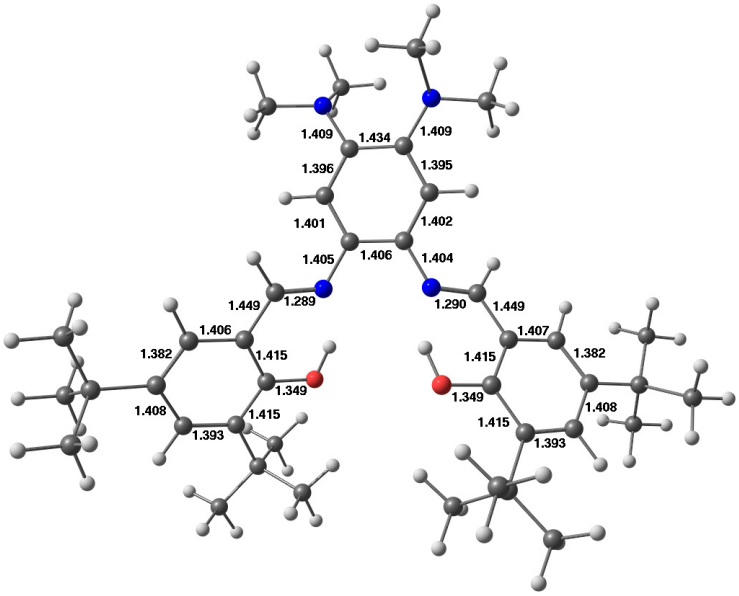

Figure C-1. DFT-optimized structure of $H_2\mathbf{L}^1$ and selected bond lengths.

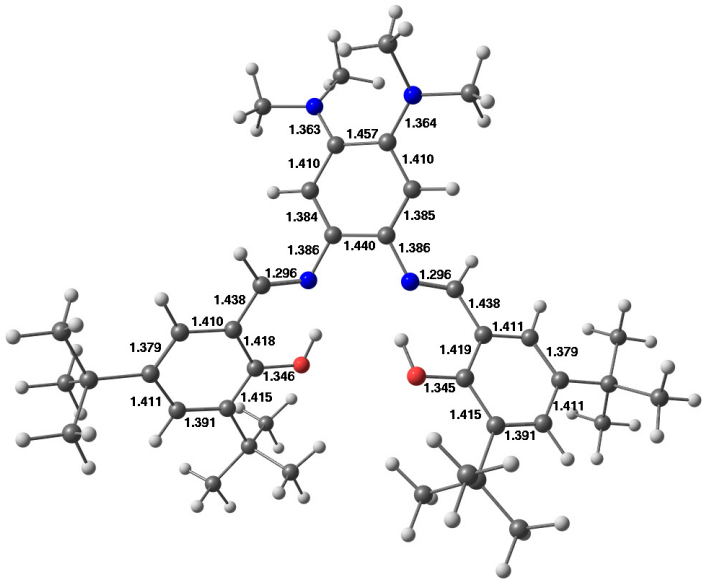

Figure C-2. DFT-optimized structure of $(H_2\mathbf{L}^1)^+$ and selected bond lengths.

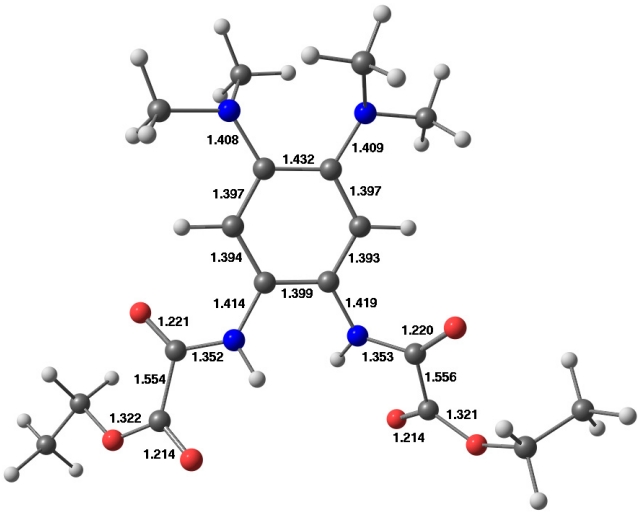

Figure C-3. DFT-optimized structure of $Et_2H_2\mathbf{L}^2$ and selected bond lengths.

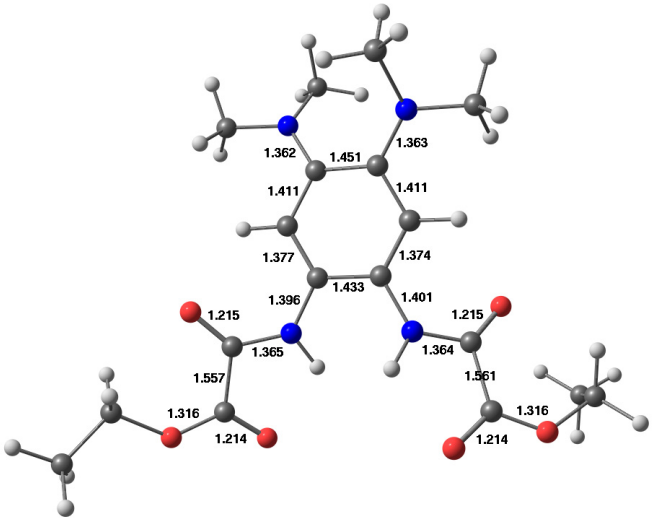

Figure C-4. DFT-optimized structure of $(Et_2H_2\mathbf{L}^2)^+$ and selected bond lengths.

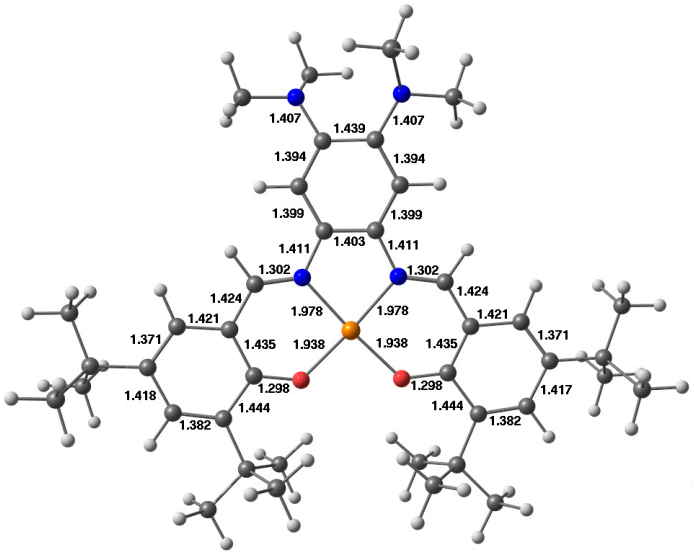

Figure C-5. DFT-optimized structure of **1** and selected bond lengths.

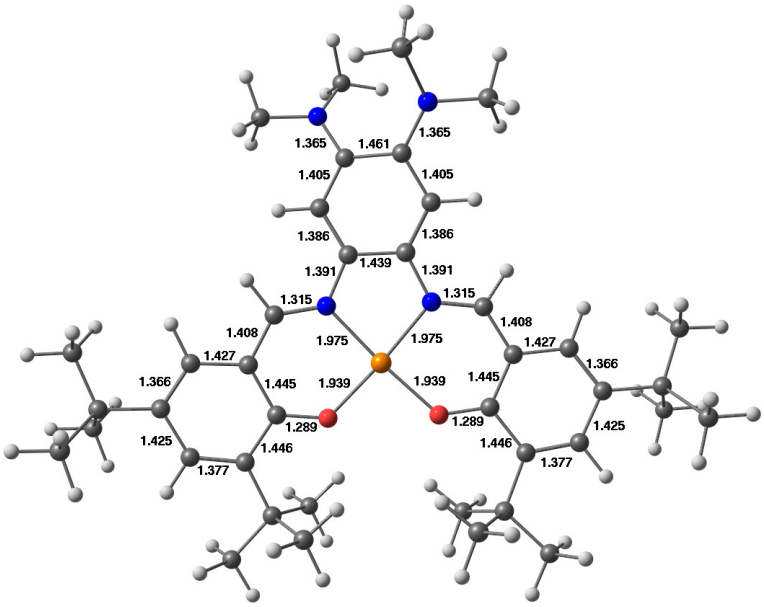

Figure C-6. DFT-optimized structure of triplet $\mathbf{1}^{+}$ and selected bond lengths.

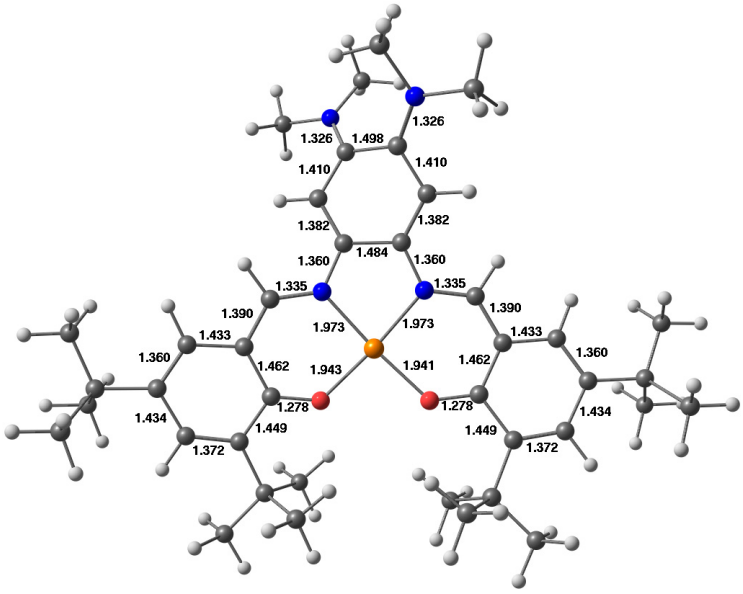

Figure C-7. DFT-optimized structure of doublet $\mathbf{1}^{2+}$ and selected bond lengths.

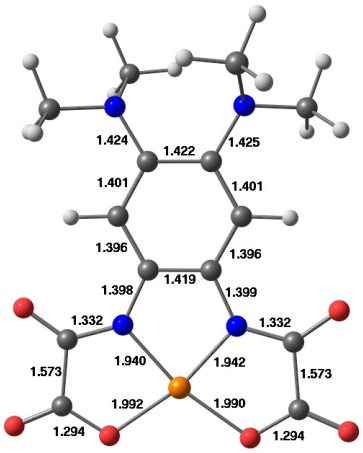

Figure C-8. DFT-optimized structure of $\mathbf{2}^{2-}$ and selected bond lengths.

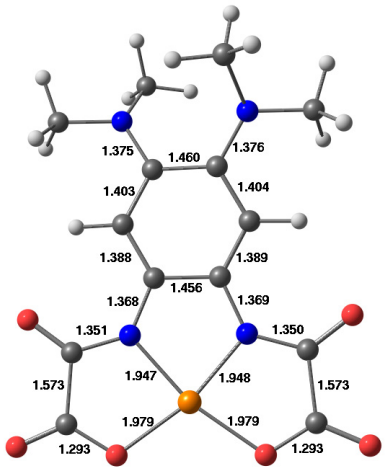

Figure C-9. DFT-optimized structure of triplet $\mathbf{2}^{-}$ and selected bond lengths.